

**THE IMPACT OF BUBBLES ON UNDERWATER
ACOUSTIC COMMUNICATION**

GABRIEL CHUA YU HAN
(B.E.), (M.S.), National University of Singapore (NUS)

**A THESIS SUBMITTED FOR THE DEGREE OF DOCTOR
OF PHILOSOPHY**

**DEPARTMENT OF ELECTRICAL AND COMPUTER
ENGINEERING**

NATIONAL UNIVERSITY OF SINGAPORE

2020

SUPERVISOR:
Associate Professor Mandar Chitre

EXAMINERS:
Professor Zhang Rui
Emeritus Professor Lawrence Wong Wai Choong
Dr. Joao Pedro Gomes, Instituto Superior Técnico

DECLARATION

I hereby declare that this thesis is my original work and it has been written by me in its entirety. I have duly acknowledged all the sources of information which have been used in the thesis.

This thesis has also not been submitted for any degree in any university previously.



Gabriel Chua Yu Han

31st Dec 2019

ACKNOWLEDGEMENTS

Looking back at the Ph.D. journey, I see myself as a buoy in the middle of a wild ocean, and the many confounding theories in the body of literature as the turbulent currents buffeting me around in this vast ocean. Although I am drifting, thank God, I am not a suspended bubble without grounded support. I am fortunate to have received wonderful support from the people I worked with. One of the first people I am deeply grateful to is my advisor, Prof. Mandar Chitre. His dedication in mentoring me has helped me during the most difficult period, when everything seemed so tough. Furthermore, he was the first to believe in me and thought that I have the potential to achieve something extraordinary. All these gave me the confidence in navigating the uncharted waters.

I am also grateful to Dr. Grant Deane from Scripps Institute of Oceanography for his valuable guidance in the project direction as well as the numerous occasions where he rendered help. The project would not have been as successful without his dedication and selfless support. The success of a project is also hardly the work of a few individuals, it is the culmination of effort from the people who have all contributed to the project in many different ways. As such, I am grateful to the project team, namely: Mr. Koay Teong Beng, Mr. Kee Boon Leng, Ms. Tan Soo Pieng, Ms. Annie, Mr. Low Teck Khoon for providing logistical support in the experiments. I would also like to express my appreciation to my peers and colleagues, namely Dr. Too Yuen Min and Dr. Gao Rui for their valuable inputs. I also thank Ms. Ong Lee Lin, for her help in editing the manuscripts.

Lastly, I thank my family for the love and support that they have showered me during these years. I thank my wife, Kai Yunn for taking care of the two little children (Yi Yong and Ee Lerd) when I needed more time at work. I also thank my siblings Yu Song and Yu Min for accompanying papa and taking care of him at home. Thank you so much for being there. I dedicate this work to my father and my late mother, without whom, I would not be what I am today.

Contents

Abstract	iii
List of Acronyms	xi
List of Notation	xiii
1 Introduction	1
1.1 Motivation	1
1.2 Rationale of the Research Questions	3
1.3 Objectives	6
1.4 Thesis Contributions	6
1.5 Thesis Organization	7
2 Preliminary Experiments	8
2.1 Mission 2013 Experiment	8
2.2 Research Vessel Experiment	11
2.3 Summary	14
3 Literature Review	15
3.1 Bubbles Generated by Wind	15
3.2 Bubbles Generated by Ships and Boats	18
3.3 Impact of Bubbles on Acoustic Communication	18
3.4 Bubble Acoustics Theory	21
3.5 Summary	24
4 Bubble Measurement Techniques	26
4.1 Controlled Experiment	26
4.2 Acoustical Validation	28
4.3 Summary	35
5 Persistence and Impact of Bubbles	36
5.1 Choice of Acoustic Frequencies	36
5.2 Wind-Wave-Flume Experiment	40
5.3 Bubble Measurement Results	43
5.4 Discussion	48
5.5 Impact on Communication Systems	50
5.6 Large Scale Variations	62
5.7 Summary	67
6 Micro-bubble Advection from Shipping Lanes	69
6.1 Collective Lifetime of Bubbles	69
6.2 Modeling the Spatial-reach of Micro-bubbles	72
6.3 Experiment Description	76

6.4	Experiment Results	78
6.5	Comparison of Model and Experimental Data	81
6.6	Summary	83
7	Impact of advected micro-bubbles on communications	84
7.1	Introduction	84
7.2	Experiment Description	85
7.3	Data Processing	85
7.4	Soft estimates analysis	95
7.5	Long-term Channel Variations	100
7.6	Summary	102
8	The Stabilization of Micro-bubbles	104
8.1	Theoretical Model	105
8.2	Experiment Description	111
8.3	Comparison between Theory and Experiment	116
8.4	Summary	118
9	Conclusions & Future Research	119
9.1	Conclusions	119
9.2	Future Research	121
	Bibliography	123
	List of Publications	128

Abstract

Underwater wireless communication has a wide variety of applications in both the defense and commercial sector, such as remote control of vehicles in offshore oil rigs, scientific monitoring of the ocean, and underwater communications among various underwater vehicles . Although acoustic waves are not the only means of wireless transfer of information in water, they are the only ones that can travel longer distances. Radio and optical waves suffer from high attenuation in water and do not propagate as far. We often observe acoustic communication performance degradation when a ship traverses a communication link. As ships generate bubbles, we believe that these bubbles contribute largely to the observed performance degradation. However, the actual impact and its duration is not fully understood.

In this thesis, we identify that the rapid channel variations are more long-lasting as compared to the strong attenuation, as the variations are caused by long-lived bubbles that are suspended in the ocean. The lifetime of these bubbles can be as long as a few hours. The impact of these bubbles is far-reaching as they have the potential to be advected by currents to distant locations. We quantify the impact of these bubbles on acoustic communications from the data observed in series of experiments. We also provide a physical explanation of the longevity of these bubbles. In all, we establish a comprehensive physical understanding of the bubbles that impact communications. The characterization

of the channel can be used as a representation of a class of channels where bubble advections from distant intermittent injections are known to exist.

List of Tables

2.1	PSR during various time-sections of the experiment. Highlighted in gray are times where the performance of the link is severely degraded from its nominal performance.	11
3.1	Bubble Model [1] (Monahan, 1993)	17
3.2	Typical values for physical parameters	25
4.1	Variable description	32
5.1	Stages of Experiment	41
5.2	Estimated constants for void fraction decay	44
5.3	Typical physical parameter values in (5.9)	47
5.4	Model calculations of path arrival time and observed arrival time.	56
5.5	DFE parameters	62
5.6	Model calculations of impulse response arrival time vs experiment observed arrival time.	64
8.1	Physical parameter values in (5.9) and (8.20)	111

List of Figures

2.1	(a) Bottom-mounted modems. (b) The surface modem, Node 21. (c) Deployment process.	8
2.2	Modem deployments during the MISSION 2013 Experiment. Yellow boxes are the nodes. The depths of the seabed are labeled with white labels.	9
2.3	The barge which is at the center of the deployment.	10
2.4	Diagram depicting communication link geometry for link node 21 to node 34 (not drawn to scale).	11
2.5	(a) Research Vessel Galaxea. (b) Vessel path.	12
2.6	Constellations and CIR before, during and after the research vessel passed by the communication link.	14
4.1	(a) and (b) show the wood pores. (c) and (d) show the wooden bubble generator.	27
4.2	The optical imaging setup	27
4.3	The raw image of the bubbles taken from the optical experiment. The black dots are the bubbles. The rings and the blurred circles are the bubbles that were not in focus.	28
4.4	Empirical bubble density from the cross-sectional images and its kernel density fit.	29
4.5	Tank experimental setup diagram for the measurement of attenuation and phase speed in the bubbly medium.	30
4.6	A photo of the tank experimental setup.	31
4.7	Solid line is the attenuation and sound speed given by the EMT with the bubble density estimated from the images. The dots are the acoustic experiment data points.	34
5.1	δ^{-1} for bubbles of 10 - 1000 μm evaluated with parameter values defined in Table 3.2 for various frequencies.	37

5.2	Schematic of the experimental setup. Tx is the projector used to transmit acoustic signals, Rx1 and Rx2 are the receiving hydrophones for estimation of bubbles. Rx3 is an additional receiving hydrophone located further in the channel.	40
5.3	The interleaving structure of the bubble probes and the PN-sequence.	41
5.4	Void fraction as a function of time. The solid lines are the experiment data and the dashed lines are the fitted exponential decaying trends.	43
5.5	Bubble spectral density measurement from the first and second run. On the left vertical axis is the bubble size, and on the right vertical axis is the corresponding resonance frequency of the bubble.	46
5.6	Theoretical dissolution curve from (5.9) at a dissolved gas concentration of 0.85.	47
5.7	(a) shows the channel estimates of the channel at Rx2 at Stage A. (b) shows a concatenation of the snapshots of CIRs during the transition from Stage A to Stage B.	55
5.8	Amplitude and amplitude fluctuation of direct path. Data show increase in variability during Stage E.	56
5.9	Amplitude distribution and power spectral density (PSD) of the variations in Stage B and Stage E. From (a) to (b), there is an increase in width of the distribution following the presence of micro-bubbles in Stage E. In (c), data show an increase in variations at the higher frequencies after micro-bubbles were introduced.	57
5.10	(a) is the extracted phase in radians. (b) is the phase fluctuations after de-trend operation. The standard deviation in Stage B is 0.029 and the standard deviation in Stage E is 0.039.	58
5.11	Phase distribution and PSD of the variations in Stage B and E. .	59
5.12	(a)-(c), the output of the DFE after equalization for Stage A, Stage B and Stage E. The figure in (d) shows the projected variability at an intersecting length of 100 m based on the measured variability.	63

5.13	First segment, CIR at Rx3 when the channel is static initially. On the labels are assigned paths of each arrival based on calculations from channel geometry. The second segment is when there were only waves. Wave height is 0.35 m peak to peak, this corresponds to ≈ 0.23 ms delay time fluctuation. Third segment is when the bubbles were just injected.	64
5.14	In the upper panel, the amplitude of the first most energetic arrival at Rx3 is shown. On the two lower panels, we show an enlarged view of the variations in a time-frame of 2 minutes for both before and after the injection. While the oscillation on a 2 s interval is largely similar, the modulating envelope on a minute to minute basis is distinctly different.	65
5.15	The power spectral density (PSD) of the variations. On the blue solid line is the spectra at Stage B (only waves), on the red dashed line is the spectra at Stage E (waves and micro-bubbles advection). On the black line is the spectra in Stage A (electrical noise only). The wave modulations remained the same, but the sub-hertz band is distinctly different.	66
6.1	Model evaluation against estimated decay constant, Γ_u	72
6.2	Conceptual diagram of the advected bubbles from the shipping lanes. u is the current strength.	72
6.3	Void fraction with respect to distance from shipping lane (- O(10 m))	75
6.4	Experiment nodes deployment.	76
6.5	(a) Bubble resonator. (b) The buoy and Node C. (c) Deploying the bubble resonator.	77
6.6	Cross-sectional view of the communication nodes deployment. . .	77
6.7	The upper panel is the void fraction measured on the bubble resonator. The middle panel is the current measurement from the ADCP. The lower panel is the ship arrivals from the AIS data. Distance is calculated as the nearest distance of the ship from the bubble resonator.	78
6.8	Ships which passed through the shipping lane on the day of experiment. The ship information is retrieved from the AIS logger. In brackets are the labels, below the brackets are MSSI of the ships. The red cross indicates that there is no image available for that ship.	80
6.9	Bubble spectral density measurements.	81

6.10	Void fraction with respect to current strength (model against experiment data), for a fix distance (300 m) from the shipping lane.	81
7.1	Block diagram of the signal flow.	85
7.2	The observed BER to SNR data points during the experiment. The light green dots represent data points from the time-frame of 11:15 am to 12:30 pm where bubble advections are observed at the bubble resonator. Whereas black crosses represent data points from the time-frame of 12:30 pm to 14:07 pm, this corresponds to the time where bubbles are observed to be fewer on the bubble resonator.	88
7.3	CIRs before and after 12:30 pm.	90
7.4	Intra-block variability	91
7.5	Q-function with respect to X_n . X_n is evaluated at various noise amplitude, n . $Q_x(X_n)$ is the probability that the random variable takes a value larger than n . It can be seen that the S α S distribution is a much better model in describing the tail probabilities of the data.	93
7.6	Amplitude distribution and PSD of first most energetic arrival before and after 12:30 pm.	94
7.7	Constellation diagram of the estimated transmitted symbols by the MMSE equalizer.	95
7.8	Amplitude and phase of the error estimates.	97
7.9	Distribution of the SDEs conditioned on various SNR regions. . .	98
7.10	Distribution of the SDEs conditioned on various SNR regions. . .	99
7.11	Spectral analysis of measured $H(t_p)$ and the fits of the two models. The dashed-line is the AR(1) fit, while the dotted line is the advection filter fit.	101
7.12	Proposed physical model for the random bubble cloud arrivals. .	101
8.1	Bubble dissolution model	105
8.2	Dissolution in the presence of surfactants	108

8.3	A comparison of dissolution with and without surfactants. The curves are evaluated with $\epsilon = 0.1$ which corresponds to 10% of the surface of the original bubble is coated with surfactants. The bubble stabilizes once it dissolves until the surfactant area covers the whole diffusing surface.	110
8.4	Map of Singapore and the four locations where water was sampled.	112
8.5	Stabilization experiment setup	113
8.6	Stabilization Experiment Results (1)	114
8.7	Stabilization Experiment Results (2)	116
8.8	Stabilized void fraction decay model vs. experiment data observation	117

List of Acronyms

ADCP	Acoustic Doppler Current Profiler
ADE	Advection Diffusion Equation
AIS	Automatic Identification System
AR	Auto-Regressive
AWGN	Additive White Gaussian Noise
BER	Bit Error Rate
BPSK	Binary Phase Shift Keying
CIR	Channel Impulse Response
CLT	Central Limit Theorem
DAQ	Data Acquisition Device
DFE	Decision Feedback Equalizer
DFT	Discrete Fourier Transform
EMT	Effective Medium Theory
FT	Fourier Transform
FFT	Fast Fourier Transform
FIR	Finite Impulse Response
GPS	Global Positioning System
ISI	Inter-Symbol Interference
LMS	Least-Mean-Squares
MMSE	Minimum Mean Square Error
MSE	Mean Square Error
MMSI	Maritime Mobile Service Identity
OFDM	Orthogonal Frequency Division Multiplexing
PDF	Probability Density Function
PLL	Phase-locked Loop
PN	Pseudo-random Noise
PSD	Power Spectral Density
PSR	Packet Success Rate
QPSK	Quadrature Phase Shift Keying

RBA	Resonance Bubble Approximation
RLS	Recursive-Least-Squares
SDE	Soft Decision Error
SNR	Signal-to-Noise Ratio
USA	United States of America

List of Notation

$*$	linear convolution operator
\approx	approximately equal to
\sim	distributed by
\gg	much greater than
\ll	much lesser than
$E[\cdot]$	the expectation operator
$\Re\{x\}$	real part of x
$\Im\{x\}$	imaginary part of x
$ x $	absolute value of x , i.e., $ x = \sqrt{\Re\{x\}^2 + \Im\{x\}^2}$
$\angle x$	the phase of x , i.e., $\angle x = \tan^{-1}(\Im\{x\}/\Re\{x\})$
\mathbf{X}^*	complex conjugate transpose of the matrix \mathbf{X}
$\ \mathbf{x}\ $	L_2 norm of the vector \mathbf{x}
$\{\dots\}$	elements in a set
$\operatorname{argmax} \rho(\mathbf{x})$	the instance of \mathbf{x} for which $\rho(\mathbf{x})$ is at its maximum
$\operatorname{argmin} \rho(\mathbf{x})$	the instance of \mathbf{x} for which $\rho(\mathbf{x})$ is at its minimum
$\log(x)$	natural logarithm of x
$\log_{10}(x)$	logarithm to the base 10 of x
$\exp(x)$	exponential of x

Chapter 1

Introduction

1.1 Motivation

Underwater acoustic communication technologies have steadily matured during the past two decades. Innovations in both single-carrier and multicarrier techniques have provided data rates in the order of tens of kilobits per second, over ranges of tens of kilometers and beyond [2]. However, there are still challenging environments where even low data rates at short ranges are difficult [3]. Furthermore, on many occasions, the performance of a communication link varies with time such that an initially benign communication link can transform back and forth from a non-challenging one to a challenging one. For example, bit errors were found to be clustered [4] in the SPACE'08 experiment¹. Also, in another work, which also looks into the data from the same experiment, the author finds cyclic fluctuations of distinct Signal-to-Noise Ratio (SNR) regimes that last for few hours [5] (See Fig. 3.2 of [5]). These long periods of distinct SNRs (a few hours) in a stationary deployment setup suggest that physical oceanographic processes have a role to play in the performance of communication systems. It has also been found that these channel quality

¹SPACE stands for Surface Process and Acoustic Communication Experiment. It was conducted by Woods Hole Oceanographic Institution (WHOI) in 2008 at Martha's Vineyard, Massachusetts.

variations are more severe in a shallow underwater acoustic link [6].

One of the physical processes which are commonly linked to communication performance is the wind state, this is because wind induces waves which are in turn a source of both noise and channel variability. However, in 2013, during one of our encounters with environment-induced time-varying channel quality, we find that wind might not always be the source of communication performance degradation. This is described in detail in Chapter 2.1. In essence, it was found that although the communication performance varied significantly for the same communication link over time, the performance correlation among links are distinct even though the links were only kilometers apart [7]. As the wind is a physical process which affects sea states on a spatial scale much larger than this (one does not expect the winds to be different within the kilometer proximity), we recognize that some other environment-related variable must be behind the observed degradation. More intriguingly, we observed a correlation between currents and communication performance in specific links, leading us to suspect that a certain kind of oceanic scatterers which are carried by the currents might be behind the observed phenomenon. We had no direct proof at that time.

Two years later, in 2015, we further narrowed down the causes and identified bubbles to be the prime contributor to the observed performance degradation. This was through an opportunistic observation where we recorded signals as a research vessel was traversing a communication link. The vessel is known to generate bubbles, and we observed that the Bit Error Rates (BER) did not recover even 20 minutes after the vessel had left the vicinity. The details are given in Chapter 2.2.

1.2 Rationale of the Research Questions

Although we had direct observation of the impact of bubbles on communication, there were still many unanswered questions. These include the time-frame of the impact, the actual acoustical impact which led to the communication performance degradation, the spatial scale of the impact, and the reason behind the longevity of the degradation. These are all important questions as the answers to these would eventually determine the kind of mitigation strategies to be deployed.

Identifying the acoustical impact is important as it allows one to identify the scheme to be deployed, for example, if it was a pure SNR issue then adaptive power control would be a suitable candidate, however, if channel variability is involved then increasing the power without addressing the real cause is just “barking up the wrong tree”. In this case, one would have to choose a more Doppler resilient approach. There are a great number of these approaches described in the literature, therefore choosing the right one might be more effective than devising a new one. This choice depends on what bubbles are actually doing to the channel.

Next, although there have already been numerous mitigation strategies proposed to address the issue of time-varying channel quality, the question of which strategy to use depends on the nature and time-frame of the impact. For example, signal processing orientated methods tend to regard the time-variation of certain parameters of the channel to be stationary and non-environment specific. Example of such methods include: power control, [8], adaptive

Orthogonal Frequency Division Multiplexing (OFDM) modulations [9]. These algorithms work provided that the channel predictor predicts the channel a few time steps ahead to a certain level of accuracy. While predicting the channel a few seconds ahead might be possible, predicting the channel a few minutes ahead quickly becomes a difficult task, which is why channel prediction typically works in the time-frame of seconds [10]. Ultimately, whether these channel assumptions are satisfied depends on the physical process affecting the channel, which is why one has to look into the time-frame of an environmental impact in the search for a suitable solution.

When one considers a time-frame in the order of minutes to hours, link tuning solutions tend to provide a more feasible alternative, as the tuning does not rely on statistical assumptions of the channel variations [11], [12]. These techniques are more data-driven and attempt to learn the channel on-the-fly. When deploying these schemes, it is also important to consider the time-frame of the associated acoustical impact to prevent learning the channel at a rate slower than the actual channel variations.

At times when the link is beyond reliable communications, networking solutions, such as Rerouting and Disruption Tolerant Networks provide workable alternatives. In these cases, the link outage time-frame, frequency of outage and the spatial scale of the impact are all important factors to take into consideration.

We acknowledge that academic research in the communications field has a history stretching back a hundred-years-old, as such, there have been numerous techniques proposed for various kinds of scenarios. However, many of these techniques are based on the physics for electromagnetic waves, typically for

wireless terrestrial communications. Electromagnetic waves are different in nature from acoustic waves, and the applicability of these techniques has to be examined in the acoustics context. Therefore understanding the acoustical impact of bubbles is necessary.

In this thesis, we put our knowledge of the acoustics channel to best use by focusing on experimentally characterizing a channel impact that is prevalent yet often overlooked. We are convinced that it was overlooked due to the subtle nature of the acoustical impact. As such, we focus on providing a good physical and statistical characterization of the channel impacted by these bubbles. We not only give statistical characterizations of the channel variations, we provide the physical basis for the longevity of the impact. Subsequently, based on the longevity of the bubbles, we hypothesized that they could be carried to distant locations. We conducted an experiment and found that these bubbles were indeed carried to such places. These bubbles caused an impact on the communication channel as they are periodically advected by currents to far-flung places. The communication impact and statistical characterization of the channel along with the bubble measurements were given. Measuring and modeling the bubble lifetime is non-trivial. Predicting the spatial extent based on an observed bubble lifetime and then designing an experiment to validate it is itself an even more challenging endeavor.

We believe that with these characterizations, we equip communication engineers with a better understanding of the channel.

1.3 Objectives

The main goals of this thesis are to identify the actual acoustical impact, establish the time-frame and spatial extent of the bubbles. Furthermore, we also set to statistically characterize the channel variations in the presence of bubbles and understand the physical reason behind their long persistence. Here is a breakdown of the research objectives:

- Identify the impact of bubbles on communications.
- Quantify the time-frame of the impact.
- Quantify the spatial extent of these bubbles.
- Provide a model to emulate the impact of bubbles.
- Identify the physical reason behind the long persistence of bubbles.

1.4 Thesis Contributions

This thesis seeks to understand and quantify the impact of bubbles on acoustic communication. The key contributions are listed below.

- We identify that bubbles of around $100\ \mu\text{m}$ and below (micro-bubbles) are suspended and persist for a long time. Their lifetimes are determined by dissolution and they have the potential to last for hours. The impact of these bubbles is mostly reflected in the elevated channel variability.
- We formulate a model to predict the spatial-reach of micro-bubbles generated by a continuous stream of ships passing through a shipping lane. We experimentally verify the model.

- We give a statistical characterization for a class of shallow water channels affected by advected micro-bubbles.
- We provide a physics model to explain the surfactant stabilization process and verify it with an experiment.

1.5 Thesis Organization

Chapter 2 presents the preliminary experiments which is part of the background of the project. Chapter 3 presents a literature survey on the theory of bubble acoustics and oceanic bubbles. Chapter 4 describes the propagation methods for bubble population estimation. Chapter 5 presents the controlled experiment to quantify the impact of bubbles on communication and the time-frame of the impact. Chapter 6 presents the prediction of the spatial-reach of the bubbles and the experimental validation. Chapter 7 presents the characterization of a class of channel models for shallow waters with the presence of advected micro-bubbles. Chapter 8 presents the physical reason behind the long persistence of bubbles. A physical model is formulated with experimental validation. Chapter 9 presents the conclusions for the thesis.

Chapter 2

Preliminary Experiments

In this chapter, a detailed description of the two preliminary experiments mentioned in Chapter 1 is given.

2.1 Mission 2013 Experiment

MISSION 2013 was conducted at Selat Pauh in Singapore from 15th to 29th November 2013. The original objective of the experiment was to test the network capability of the modems and to understand the environmental factors that impact communication performance. From the analysis of the experiment data, we believe that bubbles are one of the factors determining communication performance. We present our findings here.

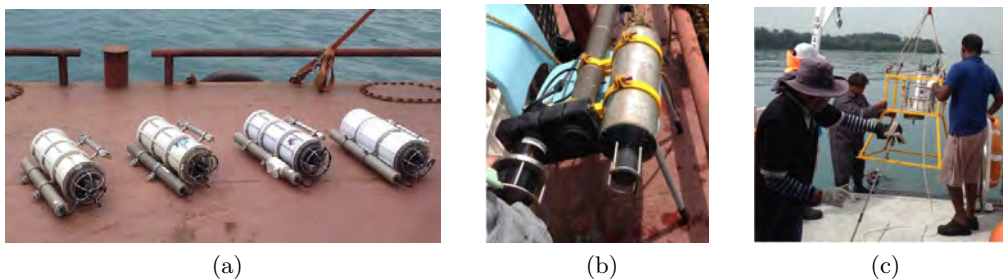


Figure 2.1: (a) Bottom-mounted modems. (b) The surface modem, Node 21. (c) Deployment process.

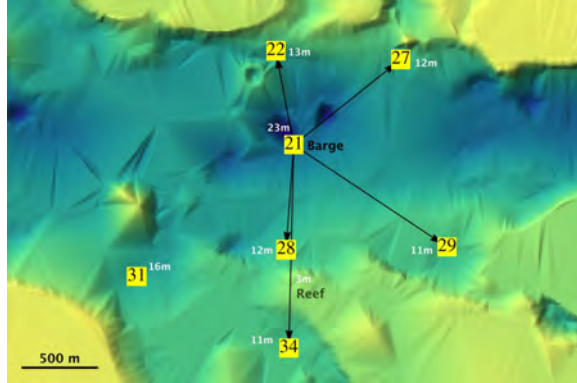


Figure 2.2: Modem deployments during the MISSION 2013 Experiment. Yellow boxes are the nodes. The depths of the seabed are labeled with white labels.

2.1.1 Experiment description

We deployed several underwater communication nodes (modems) operating concurrently. There were in all 7 modems, which were given names: node 21, 22, 27, 28, 29, 31, 34. All of them were deployed in a 2 km by 2 km area, Fig. 2.1(a)-(b) shows the modems before deployment, and Fig. 2.1(c) shows the deployment process where the modems are slowly lowered to the seabed. The location of the communication nodes in the map is shown in Fig. 2.2. Node 21 was surface-mounted on a barge while the rest were bottom-mounted. The bottom-mounted modems were suspended from a stand about 1 m above the seabed. Other than the modems, we deployed a weather sensor to monitor the winds. We also deployed an Acoustic Doppler Current Profiler (ADCP) to monitor the current strengths.

2.1.2 Network performance variability

We focus on results from 6 fragmented transmissions from 26th to 28th November. In Table 2.1, we first show the Packet Success Rate (PSR) for node 21 acting as a



Figure 2.3: The barge which is at the center of the deployment.

transmitter and 22, 28, 29, 34 acting as receivers. We show the PSR on 6 different time-sections labeled as S1-S6. The time column as shown in Table 2.1 is the elapsed time from the start of 26th November. One can see that the PSR varies significantly across links. Even in the same link, the time-variability is extensive, resulting in a PSR variation of about 200 %. The time-variability for some links are distinct and not very correlated, for example, one can see that 21-28 and 21-34 have performance degradation at different time-sections (marked in gray in Table 2.1). The change in performance can also be very abrupt, for example, the PSR for link 21-34 varies drastically in the short one-hour interval during S4 to S6. As wind speeds were very low during S4-S6, fluctuating around 3 m/s, wave-generated bubbles are occluded (>10 m/s). The only suspect observed from the Acoustic Doppler Current Profiler (ADCP) was a change in the current direction related to the maximum diurnal tide. Further, the link geometry for 21-34 shown in Fig. 2.4 could have played a part. The link had a reef in the middle, this forces the acoustic rays to propagate through a small volume of water near the surface, as such the rays have to propagate through more bubbles that

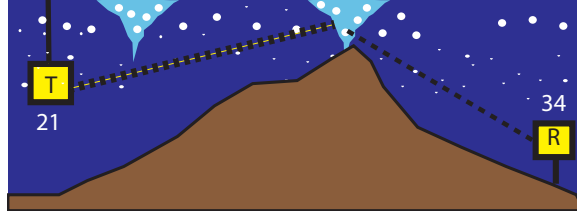


Figure 2.4: Diagram depicting communication link geometry for link node 21 to node 34 (not drawn to scale).

are known to exist in the near-surface. The source of the bubbles was unknown, however, we suspect that currents might have advected some of these bubbles into the links. A more detailed analysis can be found in our previous work [7].

TABLE 2.1: PSR DURING VARIOUS TIME-SECTIONS OF THE EXPERIMENT. HIGHLIGHTED IN GRAY ARE TIMES WHERE THE PERFORMANCE OF THE LINK IS SEVERELY DEGRADED FROM ITS NOMINAL PERFORMANCE.

Section	21 to 22	21 to 28	21 to 29	21 to 34	Time
<i>S1</i>	0.9796	0.9971	0.9983	0.6676	0.1–1.6 hrs
<i>S2</i>	0.9924	0.7786	0.9389	0.6260	20.6–21 hrs
<i>S3</i>	0.9849	0.9874	0.9940	0.6566	22.4–24.9 hrs
<i>S4</i>	1.000	0.9593	1.000	0.3529	44.5–45.1 hrs
<i>S5</i>	0.9579	0.9872	0.9936	0.5434	45.6–46.2 hrs
<i>S6</i>	0.9827	0.9480	1.000	0.7225	46.4–47.1 hrs

2.2 Research Vessel Experiment

Here, we present another experiment where the direct impact of bubbles was observed. During a field experiment on 20th Sep 2015, we had the opportunity to record communication signals as a research vessel passes through one of our communication links. The observation was opportunistic in nature as it was an on-the-spot decision to record the signals as the vessel was approaching.



Figure 2.5: (a) Research Vessel Galaxea. (b) Vessel path.

2.2.1 Experiment Description

In Fig. 2.5(a), a photograph of the vessel and its ship wake is shown. In Fig. 2.5(b), we show the path of the research vessel as it traverses the channel between the transmitter (inverted triangle) and receiver (triangle). Vessel speed was around 14 knots. The vessel intrusion started at 2:19 pm and ended at 3:00 pm, these signals were recorded, subsequently, we recorded signals 20 minutes after the vessel left at 3:20 pm. Additionally, we had a signal recorded in the morning at 9:00 am, which was originally intended as a routine recording.

The transmitted sequence was a Quadrature Phase Shift Keying (QPSK) modulated M-sequence. The carrier frequency was 24 kHz. The data rate was 9.6 kbps. The sampling rate was 2 samples per symbol. As the channel was frequency selective, the M-sequence data was equalized with the fractionally-spaced Recursive Least-Squares Decision Feedback Equalizer (RLS-DFE). It was used concurrently with a Phase-Locked Loop (PLL) as proposed in [13]. The forgetting factor, λ , was 0.995, and the number of

feedforward and feedback taps were 30 and 10 respectively. The PLL coefficients K_1 and K_2 were 10^{-3} and 10^{-4} respectively.

2.2.2 Experiment Results

The performance is given in training mode. We calculate the Signal-to-Noise ratio (SNR) with $10 \log_{10} \frac{P_s}{\sigma_{\text{noise}}^2}$, where P_s is the mean square amplitude of the signal and σ_{noise}^2 is the mean square amplitude of the noise.

In Fig. 2.6(a), we show the constellation at 9:00 am (we did not have data just prior to the vessel's passing, as this is an on-the-spot decision to record the signals) the SNR is 14 dB and the BER is 0.01. At 2:19 pm when the vessel traversed the channel, the SNR ranged from 6 to 10 dB. An instance where the SNR is at 8 dB is shown in Fig. 2.6(b), and the BER is 0.05. Next, we show the performance at 3:20 pm, which is about 20 minutes after the vessel had left the vicinity. The SNR is 19 dB, however, the BER is only 0.03, showing a performance that is worse than what we observed in the morning. This thus suggests that the SNR before the vessel's passing is likely to be higher than the 14 dB observed in the morning. The reason that the signal strength is higher in the afternoon could be due to coherent losses (constructive and destructive interference) which is in turn related to tide induced multipath superposition. This is very likely to have happened from morning to late afternoon. One can observe even after approximately 20 minutes, the BER performance has not yet even recovered to a point where the SNR was lower in the morning. This suggests that the SNR dip is not the only factor that determines the performance of the BERs.

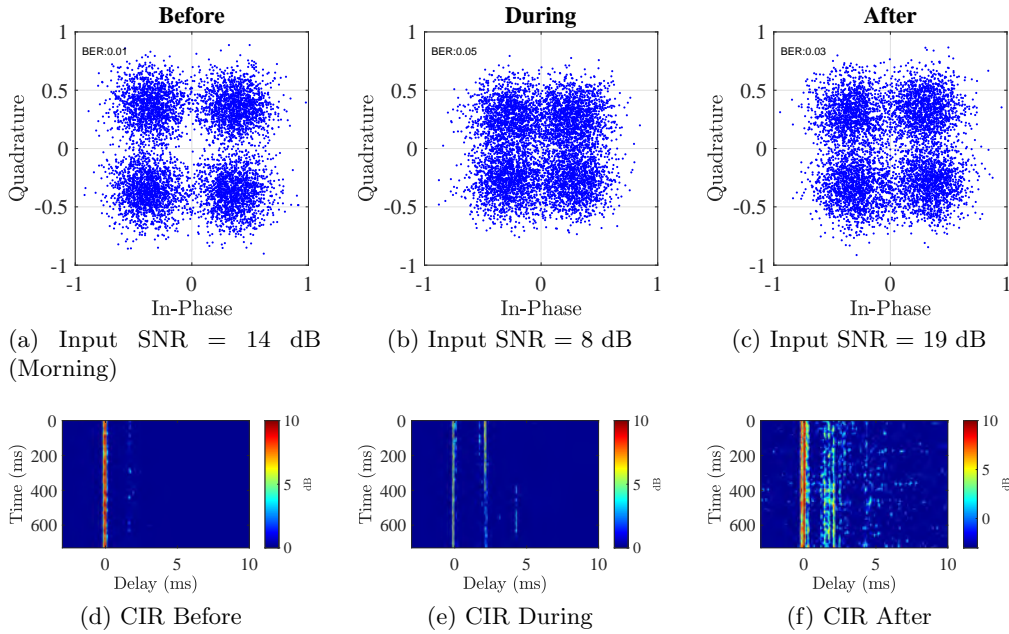


Figure 2.6: Constellations and CIR before, during and after the research vessel passed by the communication link.

In Fig. 2.6(d)-(f), we show the Channel Impulse Response (CIR) during these three instances. One can observe that although the SNR was higher in Fig. 2.6(c) as compared to Fig. 2.6(a), the channel variability is higher in the latter even though it was 20 minutes since the vessel had left. This is the cause of the BERs. This observation led us to suspect that the performance of communication systems is related to the lifetime of bubbles.

2.3 Summary

In this chapter, the two experiments which were mentioned in the previous chapter were described. From these two experiments, we identified that bubbles are indeed a concern to underwater acoustic communications. The time duration of the impact is not exactly known but we see that it can at least last for more than 20 minutes.

Chapter 3

Literature Review

3.1 Bubbles Generated by Wind

Most literature on oceanic bubble population addresses the bubbles created by breaking waves during high wind [14]–[28]. During the injection, a wave breaks and plunges into the water, injecting large amount of bubbles. The bubbles described above are created in huge quantities and exist over a wide range of sizes, ranging from tens of microns to tens of millimeters [29]. The void fraction which is the ratio of air to water during this phase is around 10^{-2} – 10^{-4} . The acoustic impact during this period is studied in [30]–[35], where it is shown that the relevant impact is the high attenuation and sound refraction associated with the initial large amount of bubbles. However, the larger bubbles are often short-lived (at most a few minutes), because their relatively stronger buoyancy causes them to surface shortly after they are created. Only during very high winds are the dense bubbles constantly replenished.

A table in [1] is reproduced to illustrate the time-scales and the spatial-reach of the bubbles associated with different stages in their lifetimes. The author categorized the bubbles created immediately after the wave-breaking event as the α and β -plume. The number of bubbles in these plumes is high as can be seen in their void fraction values. These high amounts of air in the α and

β -plume typically only last for a few seconds to at most few minutes, this is because the larger bubbles which constitute most of the air fraction, surface shortly after the bubbles' creation. The dense bubble plume thus decays into a so-called γ -plume. The fraction of air in this plume is small and is at a level of 10^{-7} . The bubble densities are not given in the original paper in [1], only void fraction values are given. The values for α and β -plume are concluded from both the analysis of photographs of the bubbles and the experimental observations from other authors [36],[37]. The lifetime of the γ -plume is decided based on a previous observation where very small bubbles in the order of a few tens of microns were detected about 15 minutes after an injection. This is due to a small difference in the backscatter return of a 240 kHz Sonar [17]. The bubble spectral density is not resolvable because this is a mono-frequency measurement. As such, the bubble density of this diffused bubble cloud is not known. The authors proposed suspension by turbulence and dissolution as the physical mechanisms behind the prolonged lifetime. The spatial-scale is decided based on the typical horizontal-scale of Langmuir circulation. However, one must recognize that Langmuir circulation is not the only mechanism by which the bubbles can be transported. We believe that 500 m² which corresponds to a 20 m \times 25 m area as claimed in Table 3.1 is an understatement of the spatial-reach.

From the literature, we conclude that the larger bubbles generated initially in the α and β -plumes are lost in at most a few minutes' time. The γ -plume which consists of smaller bubbles has the potential to last for extended periods. This is because their buoyancy is comparatively smaller and they are easily

TABLE 3.1: BUBBLE MODEL [1] (MONAHAN, 1993)

	α -plume	β -plume	γ -plumes	background
Time scale (seconds)	1.0	3.5–4.3	100–1000	-
Void fraction	10^{-2}	10^{-3}	10^{-7}	10^{-8}
$n(a = 100 \mu m)$ ($m^{-3}\mu m^{-1}$)	10^7 – 10^8	10^5 – 10^6	10^2 – 10^4	10^1 – 10^3
Horizontal scale (m^2)	0.2–1	8–50	100–500	-

suspended in the water column by oceanic turbulence. During this time of suspension, they dissolve slowly. The persistence time is generally unknown, but it is suggested they can be affected by dissolved gas concentrations and surfactant population. Furthermore, it is suggested in [17] that these smaller bubbles are coated with a layer of surfactants which further reduces their buoyancy (the surfactants have weights) and some bubbles are then incapable of surfacing, thus are left in the water for long periods. The persistence time of approximately 16 minutes reported in the table is just a conservative estimate as it is based on one experimental observation that the bubble persists for at least this amount of time on a particular day. As acknowledged by the author in [1], the actual persistence time is dependent on dissolved gas concentration and surfactant population, and both of these would be different for each experiment conditions. However, no analysis of the dissolution process is given in this literature [1].

On the other hand, since the bubble densities for the so-called γ -plume is not known in [1], authors in [31] fitted a model based on a linear decay for the bubbles densities from the β -plume to obtain the bubble densities for the γ -plume. The assumption that bubbles of all sizes just decay linearly with respect to time

is very weak. As such, we accept that the fitting is based on heuristics with the reference of prior bubble measurements [36], [37]. Since the actual bubble measurements are very rare, we can accept that these heuristics are considered best-guess decisions based on the available measurements at that time.

3.2 Bubbles Generated by Ships and Boats

Ships and boats are also known to generate bubbles. The bubbles are generated mainly through two mechanisms, first by the breaking of the bow waves, and by the cavitation from the propellers of the ships [38]. Bubbles generated by research vessels were studied in [39]. The author found that bubbles generated by the ship's propeller which is located beneath the hull could penetrate to a depth of 7–12 m. It is also claimed that these bubbles can last as strong acoustic scatterers for approximately 7.5 minutes, although the definition of “strong” is not exactly clear. In [40], the authors studied the bubbles created by a small motorboat. They noted that the bubbles mainly consist of bubbles from 20–200 μm , with void fraction decay constants between 40 – 60 s. Cross-ship-wake measurements were made by [41]. The initial bubble density at the start of the ship wake was given with an exponent of -3.6. The bubble densities in the ship wake were also given at four instances after the passing of the ship. As compared to the amount of literature devoted to bubbles generated by wind, those on bubbles generated by ships and boats are considerably less.

3.3 Impact of Bubbles on Acoustic Communication

Most literature on the impact of bubbles on communication relies on simulations based on the bubble model first proposed in [1], and further refined in [31] as

shown in Table 3.1.

In [42],[43], the authors assumed a “time-frozen” β -plume and computed the attenuation for an acoustic propagation through such a plume. As the β -plume consists of a huge amount of bubbles, with some of those in resonance with the acoustic frequency being deployed, naturally, the authors concluded the attenuation and sound refraction are the dominating factors of the propagation. As the β -plume only lasts a few seconds, the results are only representative when the replenishment happens at a rate of faster than a few seconds. The practicality of this assumption has yet to be verified.

Authors in [44] also assume a time-invariant bubble density for the β -plume. They computed a constant attenuation and sound speed change, which were fed into the simulation models to compute the communication performance. The simulation result thus shows that the high attenuation and sound refraction have a huge impact on the performance of the communication system. No reason was given as to how the β -plume could have lasted indefinitely.

In [45], the authors also assumed a time-invariant bubble density for a combination of the β -plume and γ -plume, therefore they computed a constant normalized attenuation and sound speed change. They evaluated the performance of their communication system based on this time-invariant and range-invariant bubble density, with a horizontal spatial extent of 200 m \times 200 m. It is not clear as to why the plumes could grow to such a huge size. They concluded that the attenuation has a large impact on the SNR and subsequently the packet error performance. The authors in [46] also reached the same conclusions that the attenuation and sound refraction from the dense

bubbles have the most prominent impact on communication during periods of high wind.

We independently evaluated the bubble spectral density stated in the β -plume in [31] with the effective medium theory (EMT) to obtain the attenuation for a frequency of 20 kHz. The attenuation is about 40–45 dB/m depending on the wind. With very frequent replenishment, such as those during very high wind (14–15 m/s), a constant strong attenuation is a possible scenario. However, it is only if the acoustic ray propagates directly through the bubble plume that would result in a 40 dB/m attenuation. The way in which rays interact with the bubble plume is dependent on the geometry of the channel. A direct propagation through a time-invariant plume is not always physically realistic. There are experimental observations where the communication performance actually improves when the dense bubbles completely screen off the surface arrival, causing the channel to be more benign, see Fig. 8 in [47]. As the bubbles are transient, they are constantly moving, dissolving, surfacing, and being replenished at the same time. The number of them is unlikely to be constant with respect to time, and neither will the attenuation and sound speed which is caused by this time-varying bubble population. Due to this, we reason that the approach of direct numerical evaluation of a time-invariant attenuation and sound speed change for a time-frozen bubble density is unlikely to model the time-varying experimental data. Moreover, we do not think that the larger bubbles which cause the high attenuation are the ones which have a more long-lasting effect in most low wind sea states.

3.4 Bubble Acoustics Theory

A review of the theory of bubble acoustics is presented as the theory is fundamental to the detection of the bubbles and the identification of their sizes. Bubble acoustics theory can be described as a special case of the Effective Medium Theory (EMT). The EMT is a physics model that describes the properties of a dispersive medium. The model was first proposed by Foldy in 1945 [48] and [49]. As the effective medium theory was meant to be general for any scatterer, the exact form of the scattering coefficient for the single bubble was not defined. To specifically address the bubbly medium, in 1989, Commander [50], further expanded on a series of work by Devin [51] and other authors and subsequently derived an expression for the scattering coefficient of a single bubble. They compared the model with existing experimental data and found a satisfactory fit between theory and experiment.

The dispersive property that the EMT refers to is the dependence of the attenuation and phase change on acoustic frequency. This is not the same as the dispersive channel which refers to a channel with intersymbol interference. The acoustic propagation is frequency-dependent because bubbles of different sizes have their respective resonance frequencies. The nearer an acoustic frequency to the resonance frequency, the stronger the attenuation. The frequency-dependent sound speed, which causes a frequency-dependent phase change is also coupled with the resonance frequency. This dispersive property is well-described in [52]. The limitations of the EMT is well discussed in [53]–[56].

3.4.1 The EMT

The attenuation and phase change of a plane wave can be written as a complex wavenumber,

$$P_0 e^{-\alpha x} e^{j(\omega t - kx)} = P_0 e^{j[\omega t - x(k - j\alpha)]}, \quad (3.1)$$

where,

- ω is the angular frequency,
- P_0 is the amplitude of the wave,
- k is the wavenumber.

Acoustic propagation in the bubbly medium can be characterized through the complex wavenumber [48],

$$k_m^2(\omega) = k_0^2(\omega) + \int_{a_{\min}}^{a_{\max}} h(a, \omega) n_s(a) da, \quad (3.2)$$

where,

- k_m is the complex wavenumber in the medium,
- k_0 is the wavenumber without bubbles, $k_0 = \omega/c$, c is the bubble-free sound speed,
- a is the bubble size,
- $h(a, \omega)$ is the scattering coefficient of one bubble of size a in μm ,
- a_{\min} and a_{\max} are the minimum and maximum bubble size taken into account,

- $n_s(a)$ is the scatterers spectral density which describes the amount of scatterers as a function of size per unit volume.

The above equation is the EMT. The scattering coefficient of a single bubble at a particular angular frequency is given as [35],

$$h(a, \omega) = \frac{4\pi a}{(\omega_0/\omega)^2 - 1 + i\delta}, \quad (3.3)$$

where the variables,

- δ is the damping constant of the bubble,
- ω_0 is the resonance frequency of this bubble.

The damping constant, δ is expressed as:

$$\delta = \frac{2}{\omega} \left[\frac{2\mu}{\rho a^2} + \frac{p_b}{2\rho a^2} \Im\{\phi\} + \frac{\omega^2 a}{2c} \right], \quad (3.4)$$

while bubble resonance frequency, ω_0 is expressed as:

$$\omega_0^2 = \frac{p_b}{\rho a^2} \left(\Re\{\phi\} - \frac{2\sigma}{ap_b} \right), \quad (3.5)$$

where,

- p_b is the gas pressure inside the bubble,
- ρ is the density of water,
- μ is the viscosity of water, and
- σ is the surface tension at the air-water boundary.

Here, the pressure inside the bubble is related to the pressure outside the bubble by the Young-Laplace equation,

$$p_b = p_h + \frac{2\sigma}{a}, \quad (3.6)$$

where p_h is the hydrostatic pressure at a particular depth, and both (3.4) and (3.5) have a common variable known as the Commander's Phi variable, which is given by,

$$\phi = \frac{3\gamma_h}{1 - 3(\gamma_h - 1)i\chi[(i/\chi_0)^{1/2} \coth(i/\chi_0)^{1/2} - 1]}, \quad (3.7)$$

where the variable χ_0 is defined to be

$$\chi_0 = D_t/(\omega a^2), \quad (3.8)$$

and,

- D_t is the thermal diffusivity, and
- γ_h is the heat capacity ratio.

The typical values of the physical parameters in (3.3) to (3.8) are shown in Table 3.2.

3.5 Summary

In this chapter, we gave a literature review of the oceanic bubble population, and subsequently a review of the impact of bubbles on acoustic communication systems. As most of these works focused on very high wind conditions where the injections are very frequent, they concluded that the attenuation and sound

TABLE 3.2: TYPICAL VALUES FOR PHYSICAL PARAMETERS

Parameter	Value
c	1520 m/s
p	998 kg/m ³
σ	0.0724 N/m
γ_h	1.4
D_t	2.08×10^{-5} m ² /s
P_h	1 atm (near the surface)
μ	0.00102 Pa/s

refraction are the prime contributors to the degradation of communication performance. The methodology used in these works of literature was to assume a “time-frozen” bubble density and compute a time-invariant attenuation and sound refraction which was then fed into simulation models. We found this approach to have neglected the transient nature of bubbles. We also argued that the impact which is more long-lasting and more far-reaching might not be the high attenuation which only persists during the first few minutes of the bubbles’ creation. Subsequently, a review of the theory of bubble acoustics was given.

Chapter 4

Bubble Measurement Techniques

Here, propagation measurement methods which are used in this thesis are described. We then demonstrate methods to measure propagation properties which are used to infer bubble populations in subsequent chapters. A validation between theory and experimental measurements is also given.

4.1 Controlled Experiment

We designed a controlled bubble producing mechanism and measured the acoustic impact of this controlled stream of bubbles. We compared the measured impact with the EMT predictions to relate the experimental prediction with the actual measured acoustic impact.

Controlled stream of bubbles

To generate a controlled stream of bubbles, we used a wooden bubble generator as shown in Fig. 4.1. The pores were in the microns range, as such, we were able to generate bubbles in the same size region. A high-resolution camera and a focusing lens were placed in front of the bubble generator and images of the bubbles were taken. In Fig. 4.2, a sample photograph of the bubbles is given. The optical characterization was performed with the help of the Center for Environmental Sensing and Modeling (CENSAM) at the Singapore MIT

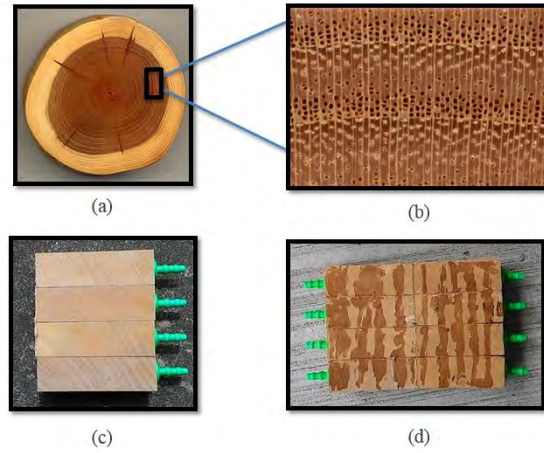


Figure 4.1: (a) and (b) show the wood pores. (c) and (d) show the wooden bubble generator.

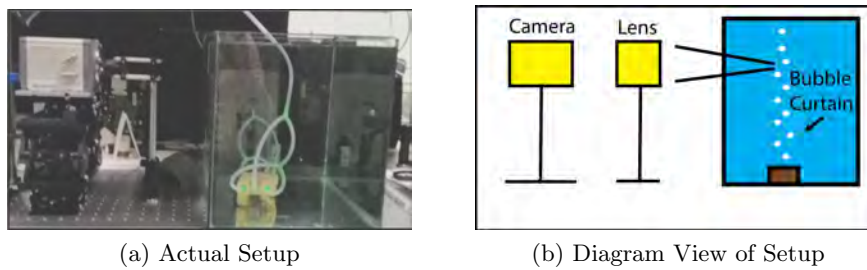


Figure 4.2: The optical imaging setup

Alliance for Research and Technology (SMART).

Bubble image processing

In Fig. 4.3, one of the photographs is shown. Only bubbles that were in focus by the camera were included, which were the black dots in the image. The rings and the circles that were blurred correspond to bubbles that were not in focus by the camera. The images are processed with NIH *ImageJ* image analyzing software. In Fig. 4.4, we show the histogram density and estimated kernel density function.

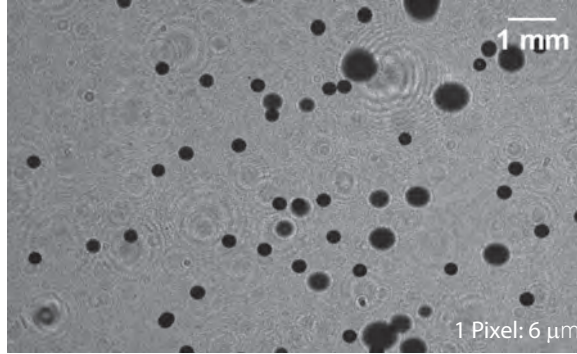


Figure 4.3: The raw image of the bubbles taken from the optical experiment. The black dots are the bubbles. The rings and the blurred circles are the bubbles that were not in focus.

The kernel density function is estimated with:

$$n(a) = \frac{1}{nh} \sum_{i=1}^n K_n\left(\frac{a - a_i}{h}\right), \quad (4.1)$$

where n is the total number of bubbles counted in all images, h is the bin width, a is the bubble size, and K_n is the Gaussian kernel function. The results are shown in Fig 4.4. The $n(a)$ obtained is fed into the EMT (3.2) to obtain the attenuation and sound speed change.

4.2 Acoustical Validation

We used an acoustic setup to examine the predicted theoretical value of the attenuation and sound speed for this controlled stream of bubbles. The bubble stream characterized optically was submerged into the acoustic setup to cross check both measured and predicted attenuation. Experiment setup is shown in Fig. 4.5. The top view is shown in Fig. 4.6. In the setup, two hydrophones were aligned in parallel in a tank filled with water. The bubble generator was

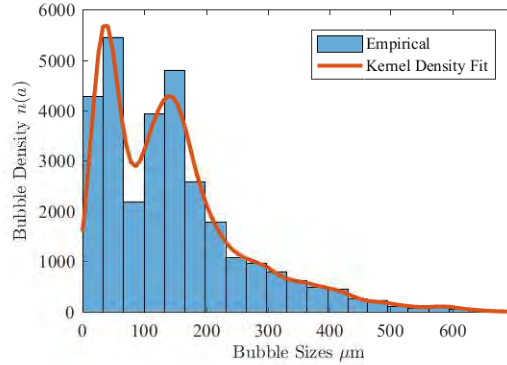


Figure 4.4: Empirical bubble density from the cross-sectional images and its kernel density fit.

placed in the middle of the two hydrophones. A steady stream of bubbles was produced. The transmitting and receiving hydrophones were customized directional hydrophones designed for an operation bandwidth of 10 kHz to 90 kHz. The transmitting hydrophone was connected to a power amplifier and the receiving hydrophone was connected to a signal amplifier, the amplifier gain was compensated in the measurement. Both were connected to a Data Acquisition System (DAQ), which was connected to a PC to transmit sinusoidal pulses of various frequency.

4.2.1 Signal transmission

A band-limited sinusoidal signal, $x(t)$ was transmitted through the setup without the bubble stream, the received signal was termed the reference signal, $x_r(t)$. Subsequently, the bubbles were turned on, and again the same $x(t)$ was transmitted through it, the received signal was termed sample signal and denoted as $x_s(t)$. Both signals were recorded by the Data Acquisition Device (DAQ).

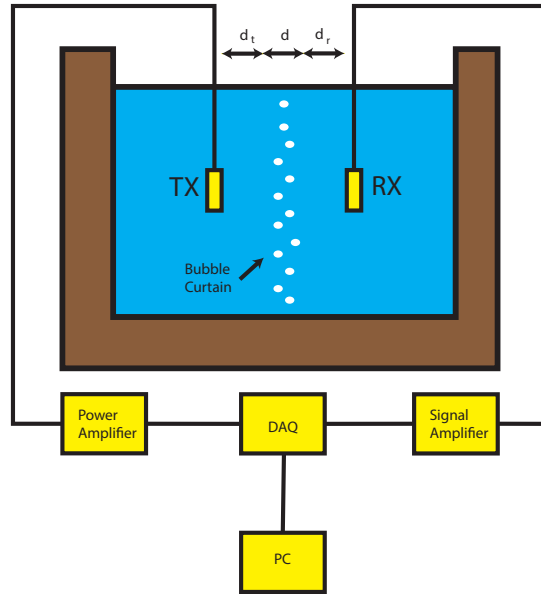


Figure 4.5: Tank experimental setup diagram for the measurement of attenuation and phase speed in the bubbly medium.

4.2.2 Data processing

All the relevant variables are listed in Table. 4.1. $X(\omega)$ and $X_r(\omega)$ are Frequency Responses (FR) of $x(t)$ and $x_r(t)$. The propagation of the reference signal can be written as:

$$\begin{aligned}
 X_r(\omega) = & \underbrace{X(\omega)}_{\text{Tx}} \cdot \underbrace{T(\omega)}_{\text{Tx FR}} \cdot \underbrace{e^{(-\alpha_0 - j\beta_0)d_t}}_{\text{Tx to BS}} \\
 & \cdot \underbrace{e^{(-\alpha_0 - j\beta_0)d}}_{\text{BS}} \cdot \underbrace{e^{(-\alpha_0 - j\beta_0)d_r}}_{\text{BS to Rx}} \cdot \underbrace{R(\omega)}_{\text{Rx FR}}.
 \end{aligned} \tag{4.2}$$

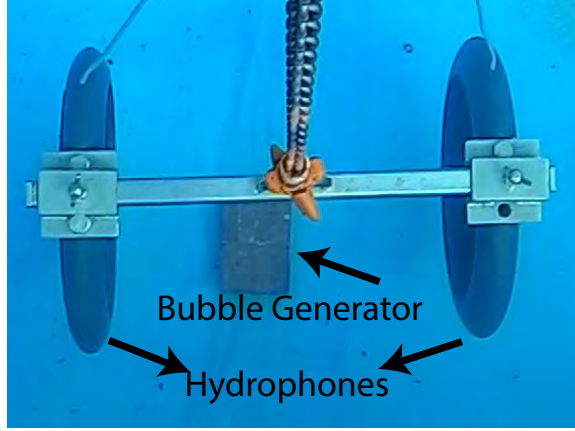


Figure 4.6: A photo of the tank experimental setup.

where BS stands for Bubble Stream. For sample signal, propagation can be written as:

$$\begin{aligned}
 X_s(\omega) &= X(\omega) \cdot T(\omega) \cdot e^{(-\alpha_0 - j\beta_0)d_t} \\
 &\cdot e^{(-\alpha_b - j\beta_b)d} \cdot e^{(-\alpha_0 - j\beta_0)d_r} \cdot R(\omega).
 \end{aligned}
 \tag{4.3}$$

By normalizing $X_r(\omega)/X_s(\omega)$, we are left with the complex wavenumber in the bubble wall.

$$\begin{aligned}
 X_N(\omega) &= \frac{X_s(\omega)}{X_r(\omega)} \\
 &= e^{(-\alpha_b + \alpha_0 - j(\beta_b - \beta_0))d},
 \end{aligned}
 \tag{4.4}$$

As such, by normalizing with respect to the reference received signal, the dependence of the received signal on four variables has been cancelled. Furthermore, within such a short distance it is possible to assume the attenuation

TABLE 4.1: VARIABLE DESCRIPTION

Variable	Description
$x(t)$	Transmitted signal
$x_r(t)$	Received signal without bubble wall
$x_s(t)$	Received signal with bubble wall
$X_r(\omega)$	Frequency domain representation of $x_r(t)$
$X_s(\omega)$	Frequency domain representation of $x_s(t)$
d_t	Distance between bubble wall and transmitter
d_r	Distance between bubble wall and receiver
d	Width of the bubble stream
$T(\omega)$	Transmitter frequency response
$R(\omega)$	Receiver frequency response
α_0	Attenuation coefficient of pure water
α_b	Attenuation coefficient of bubbly medium
β_0	Wavenumber of pure water
β_b	Wavenumber of bubbly medium

of pure water to be negligible, therefore:

$$X_N(\omega) = \underbrace{e^{(-\alpha_b)d}}_{A(\omega)} \cdot \underbrace{e^{-j(\beta_b-\beta_0)d}}_{e^{j(\phi)}}. \quad (4.5)$$

As such, one can shift the positions of the hydrophones, as long as the reference and sample signals are obtained with the same configuration, it does not affect the estimation of the complex wavenumber. In practice, we receive $x_s(t)$ within a window and perform $\text{FFT}\{x_s(t)\}$. We then normalize it with $\text{FFT}\{x_r(t)\}$ to obtain $X_N(\omega)$. As such, Amplitude Response $A(\omega)$ and the Phase Response $e^{j\phi}(\omega)$ is obtained. The absorption coefficient is estimated as:

$$\alpha_b(\omega) = -\frac{1}{d} \ln A(\omega), \quad (4.6)$$

$\alpha_b(\omega)$ is in nepers/m, a multiplication of a factor of 8.635 would result in a scale in dB/m. Absorption measurements in subsequent chapters is just performed

with this method. The window should be of reasonable size, typically, < 200 ms is sufficient for accurate measurements. The measured phase response and the wavenumber is related by:

$$\phi(\omega) = (-\beta_b + \beta_0)d, \quad (4.7)$$

The negative sign $-\beta_b$, is interpreted as the difference in the amount of phase produced per unit distance multiplied by the distance propagated. To obtain the sound speed of the acoustic wave in the bubbly medium, one has to obtain the net amount of excess phase that is produced only by the bubbly medium.

The net phase can be expressed as:

$$\phi = (-\phi_r(\omega)) - (-\phi_s(\omega)) + 2\pi\frac{d}{\lambda}, \quad (4.8)$$

The right-most term of $2\pi d/\lambda$ is because the wave propagates an extra distance of d in the absence of the bubble wall. To obtain the wavenumber of the bubbly medium, β_b , the net phase produced has to be normalized by the length the wave propagated,

$$\beta_b(\omega) = \frac{\phi(\omega)}{d}. \quad (4.9)$$

Finally, the sound speed is estimated by,

$$v(\omega) = \frac{\omega}{\beta_b(\omega)}. \quad (4.10)$$

In Fig. 4.7, we show the acoustic experiment results with the evaluation of EMT with the bubble density obtain from the photo images. As bubble density is estimated from a few cross-sectional images, the volume density of the bubbles is not known. As acoustic waves propagate through the volume instead of a cross-section, therefore, there is a scale factor mismatch between the results predicted by EMT and acoustic data. The mismatch is dependent on the focal length of the lens. We did not estimate this, so a multiplication of a constant scale factor to the EMT prediction is fitted to the experimental data. Both agree to a satisfactory extent.

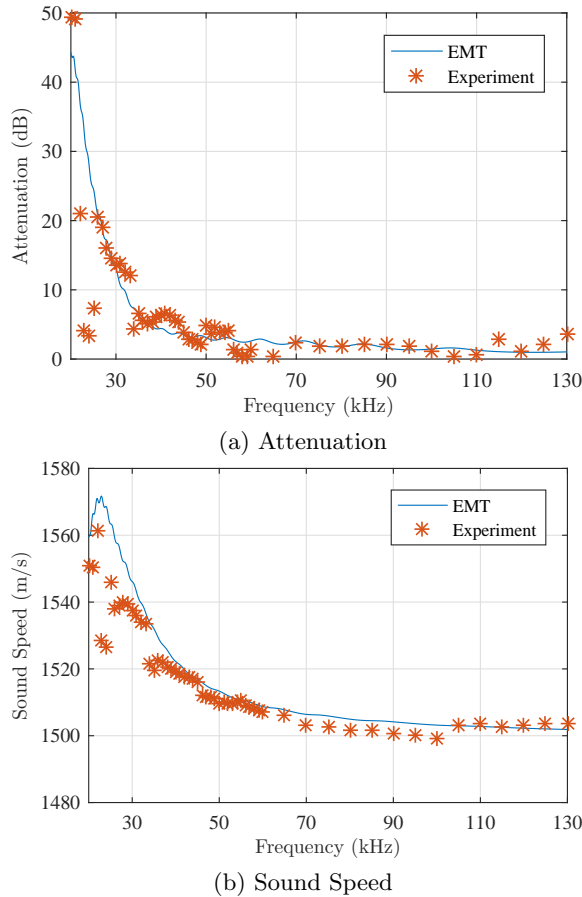


Figure 4.7: Solid line is the attenuation and sound speed given by the EMT with the bubble density estimated from the images. The dots are the acoustic experiment data points.

4.3 Summary

Here, propagation measurement methods were showed and validated with EMT theory. The measurement techniques for bubble inversion used in this thesis were shown to be substantiated.

Chapter 5

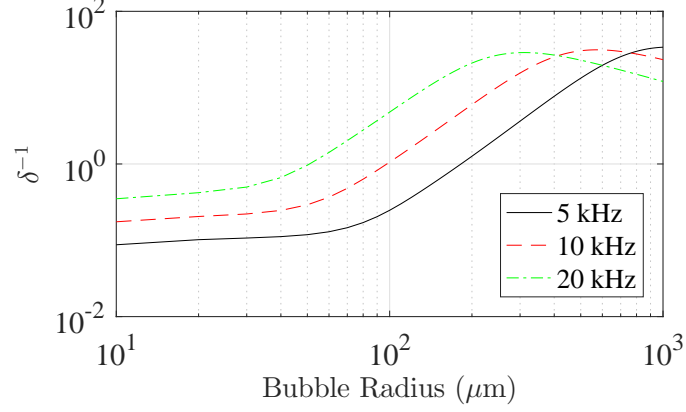
Persistence and Impact of Bubbles

In this chapter, we identify the actual impact and the time-frame of the impact of bubbles on acoustic communications. We find that although there is a high attenuation during the first few minutes after a bubble injection, the more long-lasting impact is the increase in time fluctuations of the channel. This is associated with small bubbles of sizes $100 \mu\text{m}$ and below. These bubbles are suspended and hence slowly dissolve in water. The lifetime of these bubbles can be in the order of hours, so does the channel variations. We quantify the impact on communications and show that this could potentially lead to a huge impact when the acoustic rays intersect a larger number of bubbles plumes as the path length extends. Subsequently, we quantify the longer-scale signal correlations due to the advection of inhomogeneous bubble clouds.

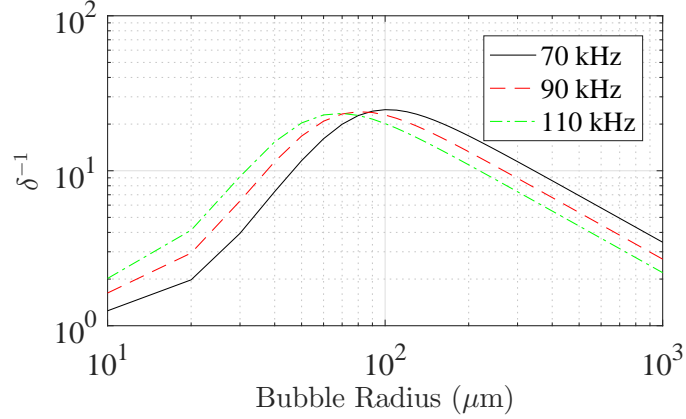
5.1 Choice of Acoustic Frequencies

The choice of acoustic frequencies for the inference of bubble size population depends on the intended size ranges. We first illustrate the attenuation of various frequencies with respect to their bubble sizes. The attenuation for a particular frequency is inversely proportional to the damping constant [52, pp. 300], we illustrate this by plotting the inverse damping constant with respect to each bubble size for a few frequencies in Fig. 5.1. One can evaluate (3.4) to obtain

the plots. In Fig. 5.1(a), the effects at the lower frequencies of 5, 10, 20 kHz



(a) δ^{-1} for 5-20 kHz for 10 μm to 1000 μm bubble.



(b) δ^{-1} for 70-110 kHz for 10 μm to 1000 μm bubble.

Figure 5.1: δ^{-1} for bubbles of 10 - 1000 μm evaluated with parameter values defined in Table 3.2 for various frequencies.

are shown, where the resonant bubble sizes are above 100 μm . Whereas in the second plot, we show the effects for the higher frequencies of 70, 90, 110 kHz, where the resonant bubble sizes are below 100 μm . In Fig. 5.1(a), the lower frequencies of 5, 10, 20 kHz only attenuates with the presence of bubbles larger than 100 μm because these frequencies are non-resonant for bubbles smaller than 100 μm (the flat plateau in Fig. 5.1(a)). One can also observe that since most of the bubbles that are smaller than 100 μm have little difference in damping

constant at these frequencies, consequently, as the 100 μm bubbles dissolve and reduce in size gradually, the change in acoustic impact is small throughout the whole dissolution lifetime. This provides the basis of the longevity of the channel variations as the bubbles dissolve.

Whereas in Fig. 5.1(b), the higher frequencies of 70, 90, 110 kHz attenuate strongly to the presence of bubbles smaller than 100 μm . These are the frequencies that will attenuate strongly when the smaller bubbles are present. Since we know that bubbles of 200 μm and above rapidly surface [40], and the resonance of them is around 16 kHz, the frequency band below 16 kHz is irrelevant. On the other hand, from bubble dissolution theory, we know that bubbles smaller than 10 μm dissolve around a few seconds. The ignorance of them only causes an uncertainty much smaller than the typical dissolution time of an hour for a 100 μm bubble. Since the resonance of them are around 86 kHz. Thus, the frequency band of 16 kHz to 86 kHz is reasonable.

5.1.1 Void Fraction

Since tracking of the size of each individual bubble across time is difficult, the void fraction, which is a collective measurement is commonly used to quantify bubble population. It is defined as:

$$\eta = \frac{4}{3}\pi \int_{a_{\min}}^{a_{\max}} n(a) a^3 da. \quad (5.1)$$

It is an integration of the air content from all the individual bubbles present in the measurement volume.

5.1.2 Inversion technique

EMT can be inverted to obtain the bubble spectral density estimates from the measured attenuation through a matrix inversion procedure,

$$\begin{bmatrix} \alpha(\omega_1) \\ \alpha(\omega_2) \\ \dots \\ \alpha(\omega_n) \end{bmatrix} = \begin{bmatrix} K(a_1, \omega_1) & \dots & K(a_m, \omega_1) \\ K(a_1, \omega_2) & \dots & K(a_m, \omega_2) \\ \vdots & \ddots & \vdots \\ K(a_1, \omega_n) & \dots & K(a_m, \omega_n) \end{bmatrix} \begin{bmatrix} n(a_1) \\ n(a_2) \\ \dots \\ n(a_m) \end{bmatrix}$$

$$n_{opt}(a) = \mathop{\text{arg min}} |\mathbf{K}\vec{n} - \vec{\alpha}|^2, \quad (5.2)$$

where \mathbf{K} is the imaginary part of the scattering coefficient. Researchers used the fact that the resonance scattering coefficient is much larger than the non-resonance scattering coefficient, and therefore simplified the inversion with an expression termed the Resonance Bubble Approximation (RBA) in [57, pp. 206] :

$$n(a) = \frac{\alpha(\omega)\delta(\omega, a)}{85.7a^3}, \quad (5.3)$$

where,

- $\alpha(\omega)$ is the absorption measured in dB/m,
- $n(a)$, is the bubble density spectra in number of bubbles/m³/μm.

This approximation has been applied in [14]–[16], [38], [41], [58] and was found to give accurate results. A more detailed description on the absorption measurement methods and the validity of the EMT is shown in Chapter 4.

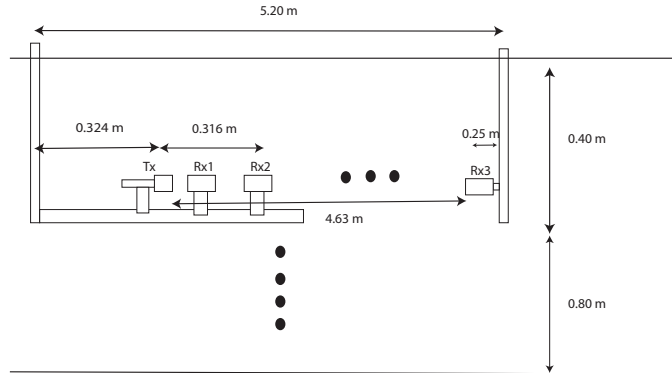


Figure 5.2: Schematic of the experimental setup. Tx is the projector used to transmit acoustic signals, Rx1 and Rx2 are the receiving hydrophones for estimation of bubbles. Rx3 is an additional receiving hydrophone located further in the channel.

5.2 Wind-Wave-Flume Experiment

The experiment was conducted in the Wind-Wave Flume at the Scripps Institute of Oceanography. The facility allowed us to generate controlled breaking waves similar to those in the ocean. To measure bubbles, we instrumented the flume with an ITC1032 projector to transmit sinusoidal pulses of discrete frequencies. These are termed the bubble probes, each probe has a discrete number of frequencies interpolated between 16–86 kHz. The frequency spacing was optimized based on the method suggested in [59]. Next, three ITC6050C hydrophones were used as receivers. Additionally, we generated Pseudo-random Noise (PN) sequences and interleaved them with the bubble probes. The PN sequence was used to study communication performance while the bubble probes were used to measure bubble evolution. The schematic of the setup is shown in Fig. 5.2. The interleaving structure is shown in Fig. 5.3.

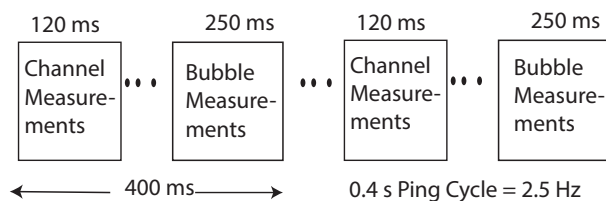


Figure 5.3: The interleaving structure of the bubble probes and the PN-sequence.

5.2.1 Experimental procedure

TABLE 5.1: STAGES OF EXPERIMENT

Stage	Wave	Wind	Flume State	Time
<i>A</i>	off	off	Flume at rest	1 min
<i>B</i>	on	off	Waves on	2–3 min
<i>C</i>	on	on	Injection phase	15 min
<i>D</i>	on	off	Buoyancy dominated phase	≈3 min
<i>E</i>	on	off	Dissolution dominated phase	< 18 min

The sequence of events and the corresponding stage of the bubble lifetime are shown in Table 5.1. In the beginning, the mechanical paddle and fan were off, the wind-wave channel was completely at rest (no wind and waves). This stage is labeled as Stage A. Subsequently, the paddle was turned on to produce waves. The wind-wave flume had 0.35 m surface waves oscillating at a frequency of 0.7 Hz. This was marked as Stage B. Next, we turned on the fan, and there was now wind blowing against the waves. This caused the waves to break and bubbles to be injected with them. This interval is termed the injection phase also labeled as Stage C. Subsequently, the fan was turned off to stop the wind, although there were still waves, these waves stopped breaking. Therefore, no more bubbles were being injected, thus the void fraction, η started to decay quickly, primarily from bubble loss due to buoyancy. As such, we termed this

the buoyancy dominated phase and labeled it as Stage D. After this stage, there is a period where a small amount of void fraction is observed for very long periods. We refer to this stage as the dissolution dominated phase and labeled as Stage E. This experimental procedure was repeated twice. The time gap between the two runs was 15 minutes.

5.2.2 Data processing: bubble probes

Absorption for each resonance frequency, ω_0 is obtained as:

$$\alpha(\omega_0) = \frac{A_{\text{bubbles}}(\omega_0) - A_{\text{no bubbles}}(\omega_0)}{d}, \quad (5.4)$$

where $A_{\text{bubbles}}(\omega)$ is the Fourier Transform (FT) of the received signal, $x_s(t)$ when bubbles are present. $A_{\text{no bubbles}}(\omega)$ is the FT of the received signal, $x_r(t)$ when no bubbles are present. Signal strength at corresponding bubble resonance frequency is obtained as the spectral component which shows the maximum signal energy.

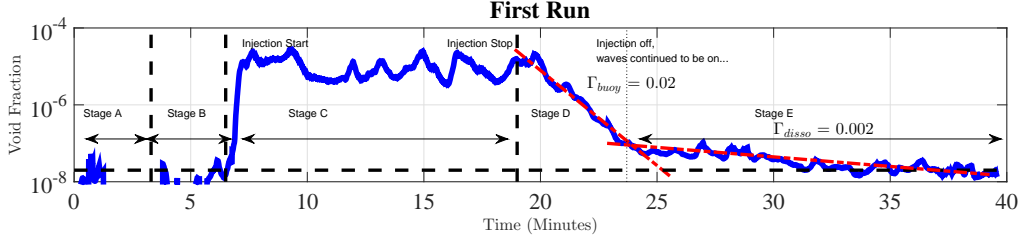
$$A(\omega_0) = \arg \max_{\omega_0} A(\omega), \quad (5.5)$$

subsequently, $n(a, t)$ is obtained from $\alpha(\omega, t)$ with (5.3). Where t is the time index of the bubble probe. Next, we integrated the bubble density to obtain the void fraction, $\eta(t)$ with (5.1). The void fraction estimates were obtained at a rate of 2.5 Hz.

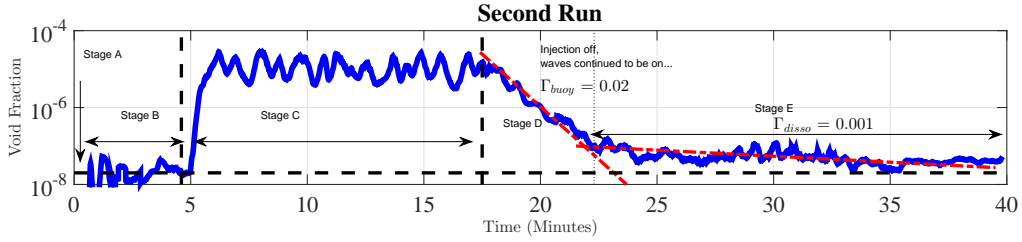
$$\alpha(f) = 20 \log_{10} \frac{p_b(f)}{p_{\text{ref}}(f)} / \text{Distance} \quad (5.6)$$

5.3 Bubble Measurement Results

5.3.1 Void fraction results



(a) First experiment run



(b) Second experiment run

Figure 5.4: Void fraction as a function of time. The solid lines are the experiment data and the dashed lines are the fitted exponential decaying trends.

We present results from two runs of the experiment. In Fig. 5.4, we show the void fraction η , as a function of time for both runs. Initially, the flume is completely at rest (no wind and waves), there are no bubbles. The small peak is due to a glitch in the paddle. Subsequently, there is a small η of 10^{-8} due to random turbulent motions generated by waves. Next in Stage C, the waves break and bubbles are injected thus η surged. We fit an exponential decay to the decreasing trend of void fraction during the buoyancy dominated stage:

$$\eta(t) = \eta_0^{\text{bouy}} e^{-\Gamma_{\text{bouy}} t}, \quad (5.7)$$

where η_0^{bouy} is the initial void fraction at the injection and Γ_{bouy} is the buoyancy

decay constant. This is performed with least-squares fitting. The buoyancy decay constant is identical for both runs, suggesting that the buoyancy process is consistent during the two runs. After the buoyancy dominated phase, the decay rate changes dramatically, signaling a change in the regime of bubble loss. The decay after this time is mostly due to the dissolution of the bubbles. We also model the void fraction decay in this stage as an exponential decay with:

$$\eta(t) = \eta_0^{\text{disso}} e^{-\Gamma_{\text{disso}} t}, \quad (5.8)$$

where Γ_{disso} is the dissolution decay constant. The dissolution decay constant fitted is much smaller than the buoyancy decay constant, one can see that the dissolution process last much longer than the buoyancy process. The second run shown in Fig. 5.4(b) is largely the same as the first run. However, the dissolution decay constant in the second run is smaller as compared to the first run. We believe this is because after the first run, a large number of bubbles were injected into the flume. These bubbles eventually dissolved to become dissolved gas, therefore the second run was likely started with a higher dissolved gas concentration. As the bubble dissolution rate is negatively dependent on the dissolved gas concentration, this translates into a longer bubble lifetime. The summary of the void fraction measurements is given in Table 5.2.

TABLE 5.2: ESTIMATED CONSTANTS FOR VOID FRACTION DECAY

-	η_0^{bouy}	η_0^{disso}	Γ_{bouy}	Γ_{disso}
Run 1	10^{-4}	10^{-7}	0.02	0.002
Run 2	10^{-4}	10^{-7}	0.02	0.001

5.3.2 Bubble spectral density results

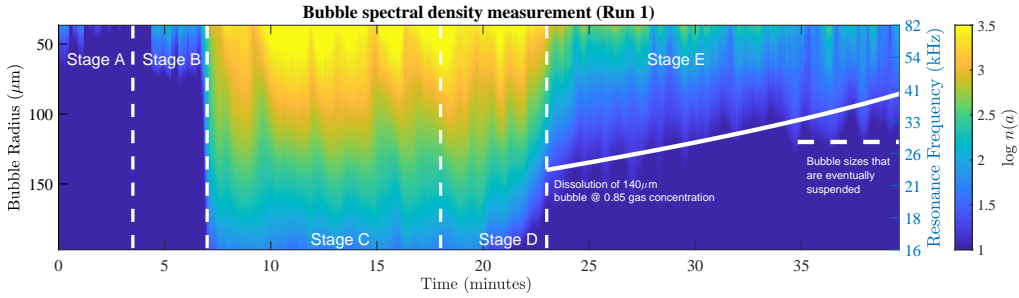
In Run 1, Stage A and B had almost no bubbles. In stage C, there is a large number of bubbles. In Stage D, the larger bubbles have a larger buoyancy and hence they rise to the surface in a shorter amount of time. Subsequently at Stage E, one can see that the loss mechanism of the bubbles starts to change. Bubbles smaller than a particular size are suspended by wave-induced turbulence. During this time, the bubbles undergo the dissolution process, where their radii decrease over time due to air diffusing from the bubbles. In the second run, in stage B, there were some leftover bubbles from the previous run. In stage D, the trend is similar. In stage E, we can observe that the bubbles dissolve more slowly as compared to run 1.

5.3.3 Dissolution analysis

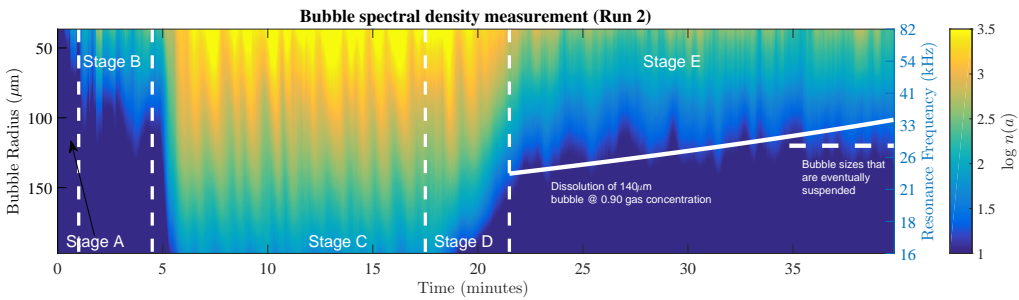
We give an analysis of the bubble dissolution process. The bubble dissolution process is well captured by the Epstein and Plesset equation [60],

$$\frac{da}{dt} = -D \frac{1 - \gamma + \frac{2\sigma}{P_a a} \left[\frac{\chi}{a} \right]}{1 + \frac{4\sigma}{3P_a a}}, \quad (5.9)$$

where $\chi = RT/K_H$. The model is a differential equation which gives the radius of a single bubble with respect to time as it dissolves in water. Specifically, it predicts the reduction in the size of a single bubble due to air diffusing from the air-water boundary of the bubble as time passes by. This equation has been experimentally verified to be accurate for the bubble sizes that affect the frequency band of interest in this paper [61]. To validate the premise



(a) First experiment run: The white solid line is the evaluation of (5.9) of a 140 μm bubble at 0.85 dissolve gas concentration ratio



(b) Second experiment run: The white solid line is the dissolution curve from (5.9) at 0.90 dissolve gas concentration,

Figure 5.5: Bubble spectral density measurement from the first and second run. On the left vertical axis is the bubble size, and on the right vertical axis is the corresponding resonance frequency of the bubble.

of a dissolution dominated trend in Stage E, we evaluate (5.9) to predict the maximum bubble size observable, $a_{\max}(t)$, as the bubbles dissolve. The evaluation is performed with a fourth-order Runge Kutta method with typical parameter values as shown in Table 5.3. We use 0.85 for γ , as this is a typical value for the dissolved gas concentration for the temperature on that day (293 K) [61]. The evaluation results for $a_{\max}(t)$ is shown in Fig. 5.6.

From our bubble spectral density measurements, we observe at the start of Stage E, the maximum observable bubble size is around 140 μm . Since from the start of the dissolution dominated phase until the end is approximately 17 minutes, the theoretical dissolution of a bubble of 140 μm in size for the same

TABLE 5.3: TYPICAL PHYSICAL PARAMETER VALUES IN (5.9)

Symbol	Parameter	Value
D	Diffusivity of air in water	$2 \times 10^{-9} \text{ m}^2/\text{s}$
σ	Surface tension	0.0724 N/m
R	Universal gas constant	0.08206 atm/(mol K)
T	Temperature	293 K
K_H	Henry's law constant	1614 atm mol
γ	Dissolved gas concentration ratio	0.85
P_a	Atmospheric pressure	1 atm

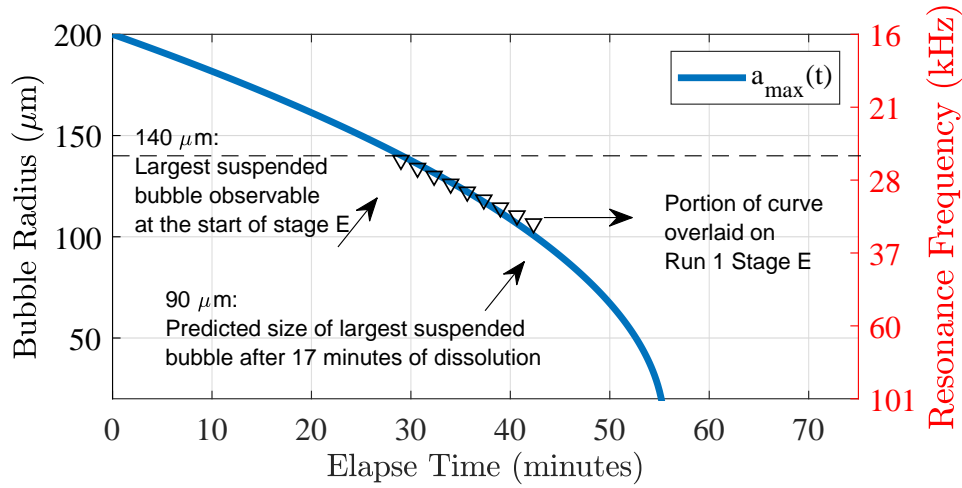


Figure 5.6: Theoretical dissolution curve from (5.9) at a dissolved gas concentration of 0.85.

17 minutes is overlaid on our bubble density measurements. This is shown in Fig. 5.5 (Stage E). We find a close agreement of the theory and measurement from the 23rd to the 35th minute, suggesting that the bubbles are indeed dissolving. However, after the 35th minute, the bubbles stop dissolving and are stabilized. This could be due to surfactants covering the surface of the bubble and thus preventing air from diffusing into the water through the air-water boundary.

By comparing the dissolution trend in both run 1 and 2, one can see that

although the bubbles that are initially suspended remained at $140\ \mu\text{m}$ and below, the rate at which the bubbles reduce in size is much slower. After reconciliation, we recognize this is due to a higher dissolved gas concentration in run 2. The dissolved gas concentration increased because the bubbles (air) which were injected in the first run dissolved to become dissolved gas. As the water is now more saturated with gas, subsequent dissolution becomes slower, and as a result, the bubbles stay even longer. For a quantitative comparison, we compare the measurements with a dissolution trend of a $140\ \mu\text{m}$ bubble at 0.9 dissolved gas concentration. We evaluate (5.9) and overlay the dissolution curve on the measurements in Stage E of Fig. 5.5(b). The slower dissolution can be explained. This thus indicates that a higher gas concentration is likely during the second run. Lastly, at the end of the experiment, again the bubbles are stabilized. Importantly, we see that the dissolved gas concentration and the stabilization effect play a significant role in the longevity of the suspended micro-bubbles. With the right conditions, the suspended micro-bubbles have the potential to last for long periods. Just by assuming the bubbles were to dissolve in water without surfactants alone, the bubbles' lifetime would have been a few tens of minutes, as can be seen for the dissolution of a $140\ \mu\text{m}$ bubble as shown in Fig. 5.6.

5.4 Discussion

From the experiments and quantitative modeling, we observe that both the dissolved gas concentrations and stabilization effect contributed to the longevity of the suspended micro-bubbles. Given that the lifetime of the suspended

micro-bubbles greatly exceeds the rate at which ship passes by in busy shipping lanes (e.g., hours of lifetime as compared to a ship every 5-10 minutes in Singapore waters), we argue that the under favorable current conditions a persistent layer of micro-bubbles could be formed within the vicinity of the shipping lanes. This is because the injection rates are much higher than the lifetime of these bubbles. Furthermore, the constant injection of bubbles also drives up the dissolved gas concentration which causes subsequent injections to last even longer, therefore, making a persistent presence of micro-bubbles in the vicinity of busy shipping lanes likely. We summarize the key findings from the bubble measurements:

- After injection, there are a lot of bubbles that last for a few minutes. The attenuation during this period is high.
- The large bubbles rise up and are rapidly lost, but the smaller bubbles are eventually stabilized. These small bubbles have the potential to last for hours. We refer to them as the *suspended micro-bubbles*.
- The suspended micro-bubble cloud consists of bubble sizes of about 100 μm and below. The void fraction in these clouds is about 10^{-7} .

The high attenuation from the dense bubble clouds is only confined to the locality of the injection, typically in shipping lanes or in areas with strong winds, and only at times when the injection occurs. What is more likely to be experienced by typical underwater acoustic communication channels is the dissolution dominated phase (Stage E). This is because, during this phase, the bubbles are diffused and can be carried (advected by currents) to much further

locations. The spatial scale of the suspended micro-bubbles extends as far as the currents can carry them during their lifetimes. As such, we put forward the argument that the suspended micro-bubbles are the ones that present a more persistent challenge to communication systems. Thus, we focus on the characterization of the suspended micro-bubbles next.

5.5 Impact on Communication Systems

5.5.1 Stochastic nature of the micro-bubbles

Acoustic propagation through bubbles is characterized by (3.2). As the micro-bubbles cloud only consists of a small number of bubbles with a void fraction of around 10^{-7} , the integral term in (3.2) results in a value that is small as compared to the bubble-free wavenumber, k_0 . By moving the k_0^2 term in (3.2) down to the denominator, we get:

$$k_m^2/k_0^2 = 1 + \frac{1}{k_0^2} \int_{a_{\min}}^{a_{\max}} h(a, \omega) n(a) da, \quad (5.10)$$

Then moving the square term to the right,

$$k_m/k_0 = \left[1 + \frac{1}{k_0^2} \int_{a_{\min}}^{a_{\max}} h(a, \omega) n(a) da \right]^{1/2}, \quad (5.11)$$

As such, we can approximate (5.11) with a Taylor series when the second term is small.

$$k_m \approx k_0 + \frac{1}{2k_0} \int_{a_{\min}}^{a_{\max}} h(a, \omega) n(a) da. \quad (5.12)$$

Note that $(1+x)^\alpha \approx (1+\alpha x)$ when x is small. The Taylor series approximation is numerically verified to be valid with a void fraction of 10^{-7} . Since bubbles that are suspended are around $100 \mu\text{m}$ and below, and a $100 \mu\text{m}$ bubble resonates at 33 kHz near the surface, it is reasonable to assume that for communication systems which operate at frequencies below 33 kHz , the resonance effect is not dominant. The respective resonance frequencies of the micro-bubbles can be obtained from the right vertical axis of Fig. 5.5. One can see that in Stage E, since most systems are out of the resonance region of suspended bubbles, scattering coefficients for bubbles of different sizes shows very little difference in values as compared to those in resonance (the plateau in Fig.5.1(a)). One can also deduce that as these bubbles dissolve, the change in the acoustical impact is small throughout the whole dissolution lifetime.

As these bubbles are randomly advected by turbulence, the number of them which instantaneously interacts with the acoustic rays changes from time to time. This causes a quasi-stationary time fluctuation of the complex wavenumber.

$$k_m(t) = k_0 + \Delta k(t), \tag{5.13}$$

where the fluctuation of the wavenumber, Δk is due to the random movement of these sub-resonance scatterers which have largely uniform scattering coefficients. Since the variations are mostly driven by turbulence, it is reasonable to assume the statistics of the variations to be stationary for the time-frames relevant to communications. This is because, under steady advection, the time-coherence of the turbulent motion is on the scale of minutes to hours [62], [63]. To model the

stochastic effect of the turbulence, we note that the bubble-free wavenumber, k_0 is a constant, while the variations caused by the turbulence-advected micro-bubbles, $\Delta k(t)$ are random. As such, we can use a generic stationary random process, $R_p(t)$ to model the variations, where $R_p(t)$ has a variation distribution and a Power Spectral Density (PSD) associated with it. The distribution describes the excursion from the mean and the PSD characterizes the time-dependent correlations.

$$k_m(t) = k_0 + R_p(t), \quad (5.14)$$

We expect that the variation distribution to follow a Gaussian distribution because by the central limit theorem (CLT), a propagation through a multiplicative concatenation of a large number of random scatterers would result in a Gaussian distribution of the variations in the dB scale. Shown as follows,

$$\log(X_1 X_2 X_3 \dots) = \log X_1 + \log X_2 + \log X_3 + \dots, \quad (5.15)$$

where X is a random variable representing the scattering coefficient of one bubble. If we model the distribution as Gaussian, we can further extract the standard deviation from the random process, and use a standard normal distribution as a base with the standard deviation describing the extent of the excursion. Shown as follows:

$$k_m(t) = k_0 + \sigma_k \zeta(t), \quad (5.16)$$

where,

- σ_k is the standard deviation of the variations of the wavenumber,
- $\zeta(t)$ is a generic random process with a standard normal distribution and a PSD associated with it.

As the real part of the complex wavenumber is the phase and the imaginary part is the amplitude, we have only three variables to determine. First, σ_a , the standard deviation of the amplitude variation, second, σ_θ , the standard deviation of the phase variation, and third, the PSD of $\zeta(t)$. Subsequently, we extract these statistics from the PN-sequence and quantify the impact of this variation on the performance of communication systems.

5.5.2 Pseudo-random noise sequence during experiment

The PN-sequence probes were in the frequency range of 18 kHz to 30 kHz, modulated at baseband data-rate of 12 kbps with a BPSK modulation scheme. The carrier frequency was centered at 24 kHz. The PN-sequence was generated with a maximal length sequence of $m = 9$, with a repetition of T_{rep} of 3, which resulted in $N_c = (2^m - 1)T_{rep} = 1533$ chips. When the number of chips is divided by the data rate, this produced a probe length of approximately 120 ms.

5.5.3 Channel estimates

We match filtered the received and transmitted probes to estimate the channel,

$$R_{xy}(\tau) = E\{\tilde{x}(t)\tilde{y}(t - \tau)\}, \quad (5.17)$$

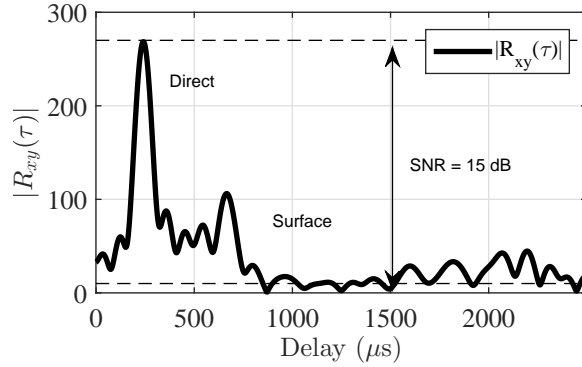
where $x(t)$ is the transmitted probe and $y(t)$ is the received probe, and $\tilde{x}(t)$ and $\tilde{y}(t)$ are the complex baseband envelopes of those signals. Here, τ is the time delay. We extracted the amplitude and phase from the output of the matched filter, as the phase and amplitude of each path are the delayed and attenuated copies of the autocorrelation function of the transmitted signal, $R_{xx}(\tau) = E\{\tilde{x}(t)\tilde{x}(t - \tau)\}$.

$$R_{xy}(\tau) = \sum_{p=1}^P a_p e^{-j\theta_p} |R_{xx}(t - \tau_p)|, \quad (5.18)$$

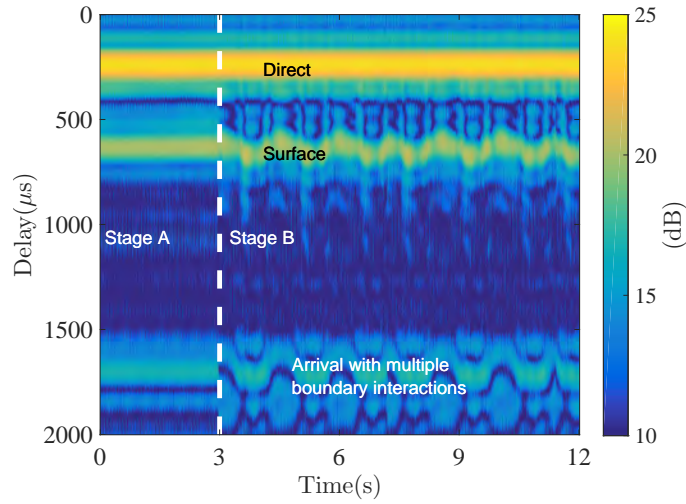
Here, a_p is the instantaneous amplitude for each path. τ_p is the arrival time delay for a specific path. P is the number of discrete paths which had amplitudes above a certain threshold. Further, θ_p is the residual phase of each path $\theta_p = 2\pi f_c \tau_e$, and τ_e is the excess delay within the minimum resolution.

5.5.4 Choice of window length

We balanced the contention between the quality of the channel estimates and the channel sampling rate by specifying the minimum Signal to Noise Ratio (SNR) for the application. Subsequently, we determined the corresponding window length required. This length thus limits the sampling rate of the channel. The minimum window length was 12 ms for Rx2. This corresponded to a channel sampling rate of 83 Hz. There was no overlap between the windows. As such, each channel estimate was a snapshot that was independent of the previous one. A good review regarding the trade-off between the quality of the channel estimate and the channel sampling rate can be found in [64], [65].



(a) CIR at Rx2 at Stage A



(b) CIR at Rx2 at transition from Stage A to Stage B

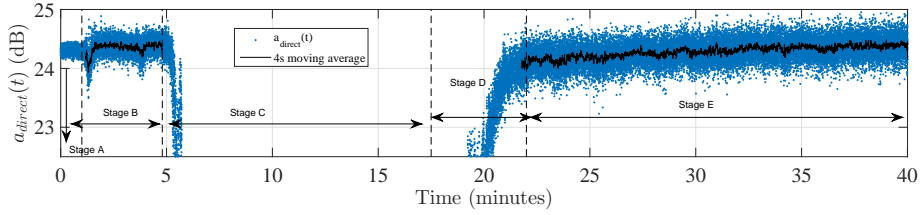
Figure 5.7: (a) shows the channel estimates of the channel at Rx2 at Stage A. (b) shows a concatenation of the snapshots of CIRs during the transition from Stage A to Stage B.

5.5.5 Data processing

In Fig. 5.7(a), we show the estimation of the channel at Rx2 during Stage A. The impulse response shows two significant peaks. The two peaks obviously corresponded to different paths. The direct and surface paths are identified by geometry as shown in Table 5.4. Subsequently, in Fig. 5.7(b), we show a concatenation of the snapshots of the channel during the transition from Stage A to Stage B. One can see that the surface path starts to oscillate when there

TABLE 5.4: MODEL CALCULATIONS OF PATH ARRIVAL TIME AND OBSERVED ARRIVAL TIME.

Path	Modeled Arrival Time	Observed Arrival Time
Direct	$0.316/1520 = 0.2$ ms	0.2 ms
Surface	$\sqrt{0.316^2 + (0.80)^2}/1520 = 0.6$ ms	0.7 ms



(a) Amplitude of direct path. Thin solid line is the 4-second moving average value.

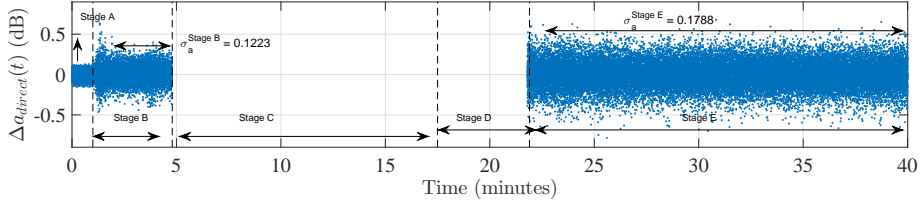

 (b) The amplitude fluctuations, $\Delta a(t) = a_{\text{direct}}(t) - \bar{a}_{\text{direct}}(t)$, $\bar{a}_{\text{direct}}(t)$ was the 4-second moving average.

Figure 5.8: Amplitude and amplitude fluctuation of direct path. Data show increase in variability during Stage E.

are waves present, but more importantly, the direct path is unaffected by wave movements. As such, by extracting the amplitudes and phases from the direct path only, the phase and amplitude variations from the moving surface are eliminated. This allows us to isolate the variations due to transducer movements and bubble motion alone. We extract the amplitude and the phase of the direct path from each channel snapshot as follows:

- For every time snapshot, t_n ,
- Find the first maxima in $R_{xy}(\tau, t_n)$ above a threshold and note its

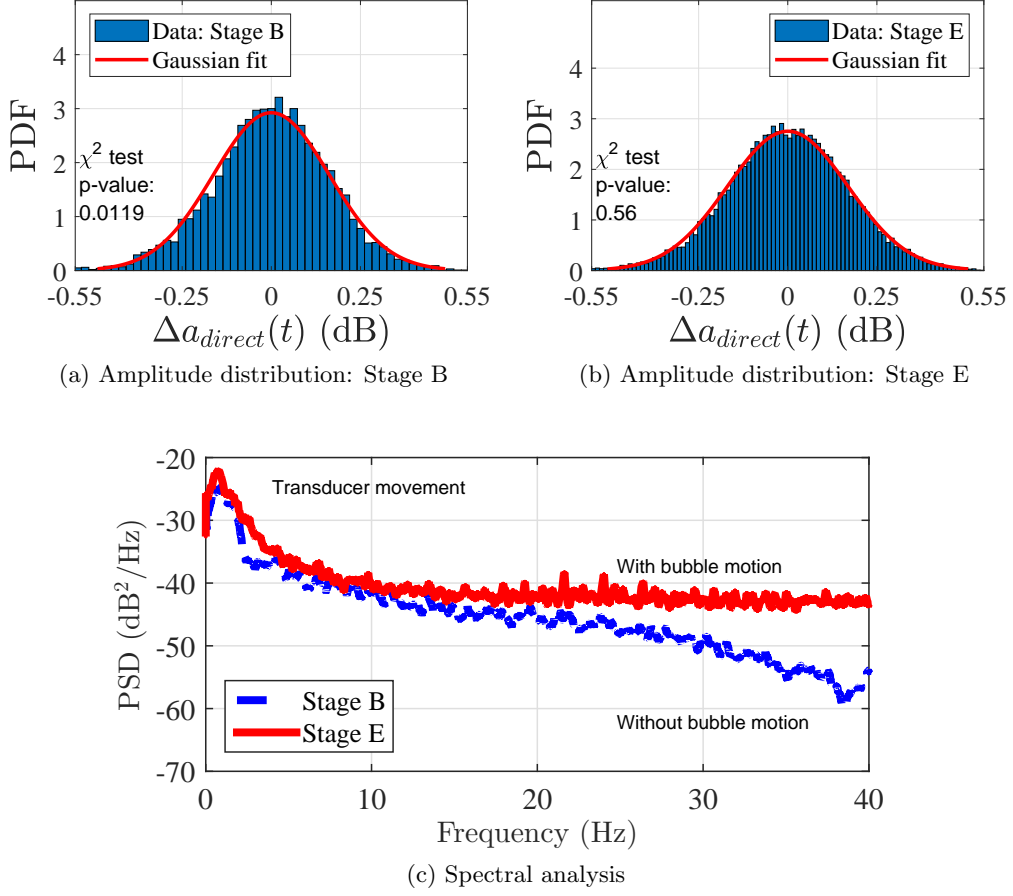
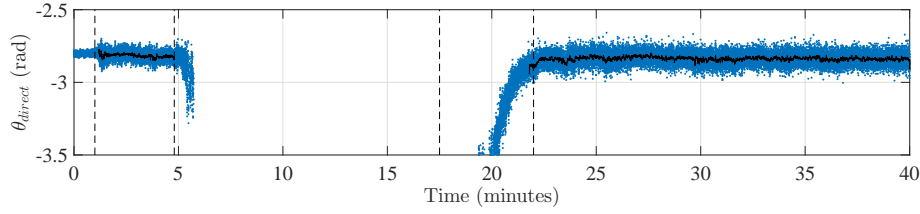


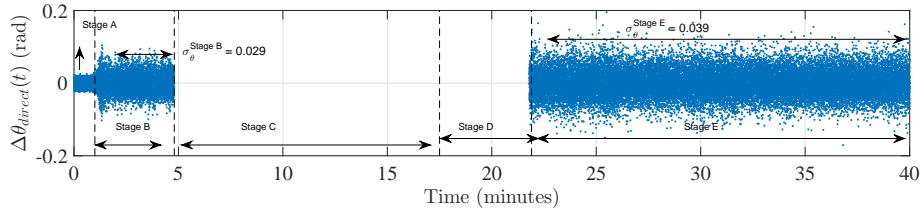
Figure 5.9: Amplitude distribution and power spectral density (PSD) of the variations in Stage B and Stage E. From (a) to (b), there is an increase in width of the distribution following the presence of micro-bubbles in Stage E. In (c), data show an increase in variations at the higher frequencies after micro-bubbles were introduced.

corresponding delay time as: τ_{direct} ,

- For τ_{direct} , assign $a_{\text{direct}}(t_n) = |R_{xy}(\tau_{\text{direct}}, t_n)|$, and $\theta_{\text{direct}, t_n} = \angle R_{xy}(\tau_{\text{direct}}, t_n)$,
- Compensate phase associated with delay by: $\theta_{\text{direct}, t_n} = (\tau_{\text{direct}, t_n} - \tau_{\text{direct}, t_0})2\pi f_c / \Delta\tau + \angle R_{xy}(\tau_{\text{direct}}, t_n)$.



(a) Phase of direct path. Thin solid line is the 4-second moving average value.



(b) Phase fluctuations, $\Delta\theta(t) = \theta_{\text{direct}}(t) - \bar{\theta}_{\text{direct}}(t)$, $\bar{\theta}_{\text{direct}}(t)$ is the 4-second moving average.

Figure 5.10: (a) is the extracted phase in radians. (b) is the phase fluctuations after de-trend operation. The standard deviation in Stage B is 0.029 and the standard deviation in Stage E is 0.039.

5.5.6 Results

Amplitude fluctuations

In Fig.5.8(a), initially in Stage A, the variability is low, as the channel is at rest. During Stage B, the variability increases as there are wave-induced transducer motions. At Stage C, the channel is completely blocked. At Stage D, the signal recovers rapidly due to buoyancy. At Stage E, there is a slow recovery due to the dissolution of bubbles. To remove the trend on longer time-scales, we perform a de-trend operation with a moving average of 4 seconds. The results are shown in Fig. 5.8(b), the variability increased in Stage E, which is due to propagation through the suspended micro-bubbles.

In Fig. 5.9(a) and (b), the amplitude distribution of the direct path in Stage B and E are shown respectively. We observe an increase in variability from

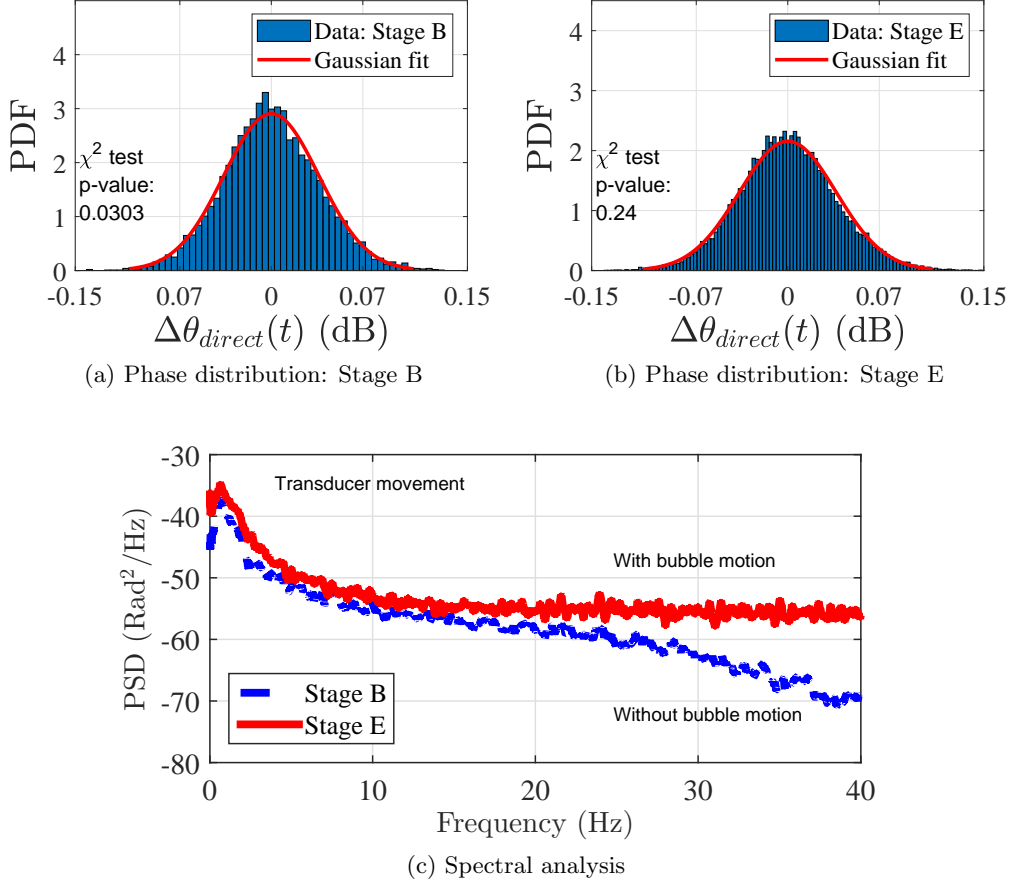


Figure 5.11: Phase distribution and PSD of the variations in Stage B and E.

the data. Data was compared to a fitted Gaussian distribution. The resulting standard deviation is 0.12 dB for Stage B and 0.18 dB for Stage E. Subsequently, we show the spectral analysis of the amplitude variations in Fig. 5.9(c). While time-correlations on 1–10 Hz scale are almost identical, (wave-induced transducer motion is consistent), however, time-correlations from 20 Hz onwards is different. We believe this is due to the fast turbulent motion that is randomly transporting the bubbles. As for the standard deviation of the variations, the fluctuation is linearly proportional to the intersecting distance between the path and the plume, $\sigma_a = \sigma_a^0 d$ [66], where σ_a^0 is the normalized variability per meter. For a

plume intersecting distance (distance from Tx to Rx2) of 0.36 m, an increase in standard deviation of 0.06 dB is measured, thus the variability per meter is approximately 0.16 dB/m. In the case of a ship wake plume, an intersecting length of somewhere between 10^0 m to 10^2 m is possible, depending on channel geometry and plume size. Thus, the possible values of the standard deviation, σ_a lie somewhere between 0.16 dB to 16 dB depending on the extent the path and plume intersects.

Goodness of fit of proposed distribution

The goodness of fit of the Gaussian distribution was quantified with a χ^2 test. We show the p-values of the χ^2 test in In Fig. 5.9(a) and (b). A larger p-value for the χ^2 test indicates a better fit of the data with the proposed distribution. The D^2 parameter of the χ^2 test is first computed as:

$$D^2 = \sum_{i=1}^k \frac{(N_k - m_k)^2}{m_k} \quad (5.19)$$

where:

- k is the number of bins.
- N_k is the observed number of outcomes in each bin.
- m_k is the expected number of outcomes according to the specified model.

If the fit is good then D^2 will be small. Under the χ^2 test D^2 follows a χ^2 distribution with $k-1$ degree of freedom. As such, the p-value is computed as:

$$p_{\text{val}} = 1 - \frac{1}{\Gamma(A)} \int_0^{D^2/2} t^{A-1} e^{-t} dt \quad (5.20)$$

where $A = (k - r_p - 1)/2$, and r_p is the number of parameters specifying the distribution. The specifics to perform the χ^2 test can be found in [67].

Phase fluctuations

Phase variability is shown in Fig. 5.10 (a) and (b). The trend is largely similar to that of the amplitude fluctuation, with the recovery of the phase being attributed to the recovery of the sound speed in the bubbly medium. De-trend operation with a 4-second moving average is performed. Residual phase variability is shown in Fig. 5.10(b). In Fig. 5.11, we show the distribution of the phase fluctuations, similar to the amplitude fluctuations, we observe an increase in variability of the phase. Phase time-correlations exhibit a similar trend to the amplitude time correlations. The increase in standard deviation of the variability is 0.01 rad for 0.36 m, therefore the variability per meter is 0.0278 rad/m. Thus for a ship wake plume, depending on the intersecting length between the path and plume, the increase in variability should lie somewhere between 0.0278 rad to 2.78 rad. The p-values of the distribution fit are also given in Fig. 5.10 (a) and (b).

5.5.7 Impact of variability on communication

The communication impact of the micro-bubbles is shown in Fig. 5.12. The adaptive Decision Feedback Equalizer (DFE) with the least-mean-squares (LMS) algorithm is applied with the following parameters as shown in Table 5.5. The performance metric is the Mean Square Error (MSE).

$$\text{MSE} = 10 \log_{10} \frac{1}{N_d} \sum_{i=1}^{N_d} |d_i - \hat{d}_i|^2, \quad (5.21)$$

where d_i is the actual symbol transmitted, and \hat{d}_i is the soft decision of the equalizer, while N_d is the total number of symbols. Fig.5.12(a)-(c) shows the constellation diagram of the equalized received symbols in Stage A, B, and E respectively, and MSEs shown in their respective plots. Although the DFE is able to track the slow variation through the adaptation of the filter coefficients [68], faster variations are reflected in the increased MSE, this can be seen as the MSE increases from Fig.5.12(a)-(c). The MSE in Fig. 5.12(a) is mostly due to inherent noise. The MSE in Fig. 5.12(b) is due to wave motions. In Fig. 5.12(c), from Stage B to E, the MSE further increases by 0.58 dB, this is due to the propagation through micro-bubbles. The increase in variability is not visually apparent due to the small intersecting length in the controlled flume. However in actual scenarios, we expect the variability to increase drastically. As the intersection length between the ray and micro-bubbles is much larger. A projected variability for an intersecting length of 100 m is added to the measured signal. We show the projected variability in Fig. 5.12(d).

TABLE 5.5: DFE PARAMETERS

Parameter	Value
Feedforward taps	50
Feedback taps	50
μ_{step}	0.001

5.6 Large Scale Variations

We characterize the slow variations that were superimposed on the fast variations described earlier. The slow variations are attributed to the large scale advection of the inhomogeneous bubble clouds. Because bubble clouds exist in distinct

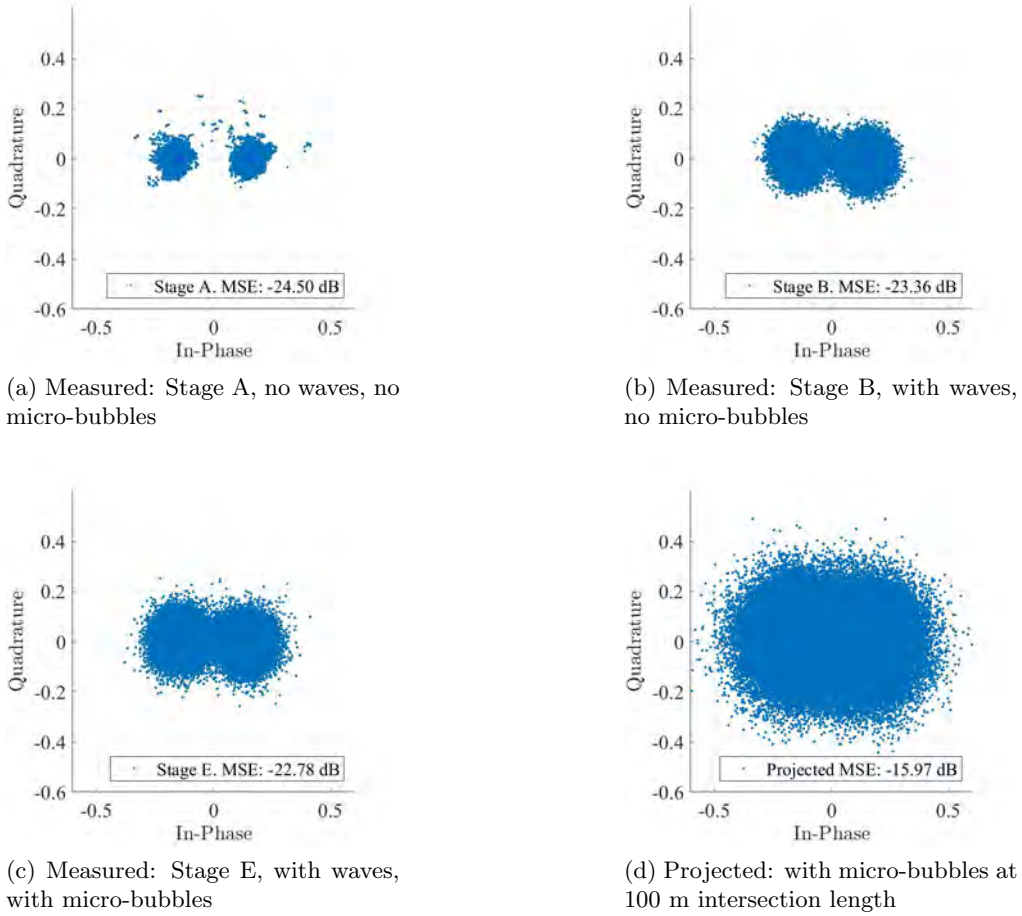


Figure 5.12: (a)-(c), the output of the DFE after equalization for Stage A, Stage B and Stage E. The figure in (d) shows the projected variability at an intersecting length of 100 m based on the measured variability.

plumes, the number density of them across space is largely inhomogeneous. As these bubble clouds are being transported by the currents on a periodic basis, they produce time-correlations of the signal on a few minutes' intervals. This is illustrated with data from Rx3.

5.6.1 Channel impulse response of Rx3

Fig. 5.13 shows the time varying CIR of Tx–Rx3. Arrival association is shown in Table 5.6. Geometry is as shown in Fig. 5.2. The only additional information

TABLE 5.6: MODEL CALCULATIONS OF IMPULSE RESPONSE ARRIVAL TIME VS EXPERIMENT OBSERVED ARRIVAL TIME.

Path	Modeled Arrival Time	Observed Arrival Time
Direct	$4.63/1520 = 3.03$ ms	2.97 ms
Surface	$\sqrt{4.63^2 + 2(0.40)^2}/1520 = 3.09$ ms	3.08 ms
Bottom	$\sqrt{4.63^2 + 2(0.80)^2}/1520 = 3.22$ ms	3.22 ms
Left/Right path(1)	$\sqrt{4.63^2 + 2(1.15)^2}/1520 = 3.40$ ms	3.34 ms
Left/Right path(2)	$\sqrt{4.63^2 + 2(1.15)^2}/1520 = 3.40$ ms	3.46 ms

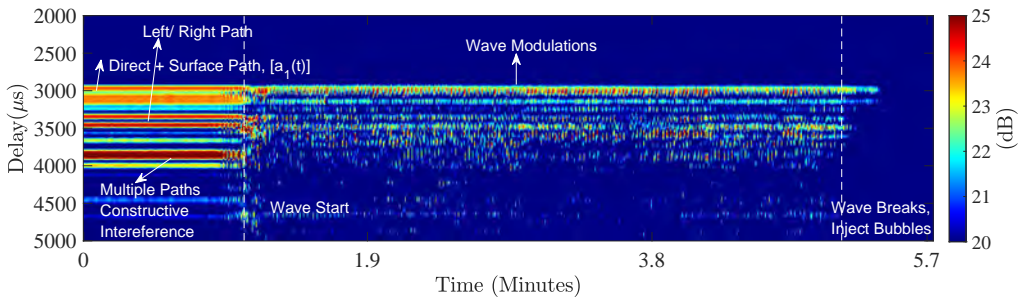


Figure 5.13: First segment, CIR at Rx3 when the channel is static initially. On the labels are assigned paths of each arrival based on calculations from channel geometry. The second segment is when there were only waves. Wave height is 0.35 m peak to peak, this corresponds to ≈ 0.23 ms delay time fluctuation. Third segment is when the bubbles were just injected.

that is needed to predict the arrivals is the width of the flume, which is 2.3 m. Channel sampling rate is 2.5 Hz. The path/arrival association is shown in Fig. 5.13, the first arrival is an unresolvable composite of the direct and surface path. The second group is the left/right path and the third group is a constructive interference of multiple boundary interactions. When the waves are turned on, the constructive interference quickly vanishes as the wavelength of the acoustic signal is much shorter than the height of the waves. This causes the phase of the signals to statistically cancel each other and result in an incoherent

loss. The wave modulations onto the acoustic signal can be seen in the flickering of the first arrival. When bubbles are injected, the surface-related arrivals are first attenuated, the direct path which is deeper in the channel is only attenuated a few seconds later when the bubbles are carried downwards by the turbulent forces.

5.6.2 Data processing

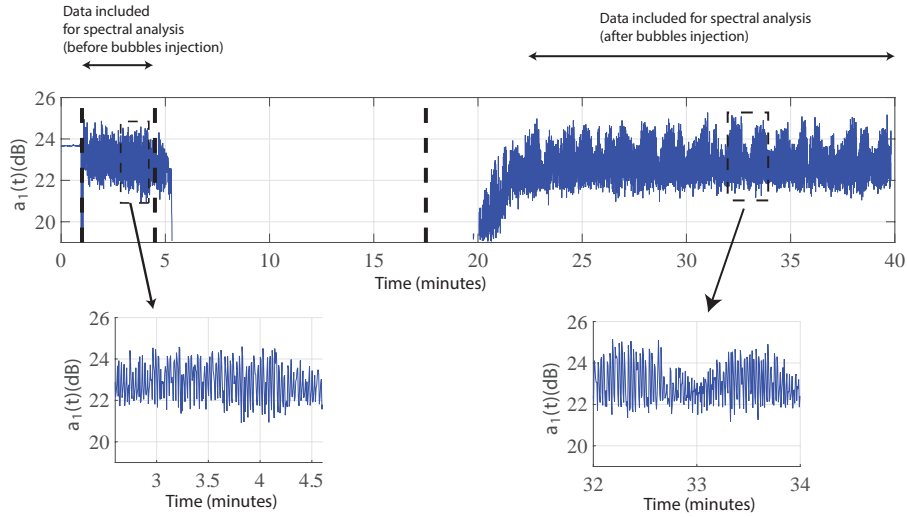


Figure 5.14: In the upper panel, the amplitude of the first most energetic arrival at Rx3 is shown. On the two lower panels, we show an enlarged view of the variations in a time-frame of 2 minutes for both before and after the injection. While the oscillation on a 2 s interval is largely similar, the modulating envelope on a minute to minute basis is distinctly different.

The first most energetic arrival, $a_1(t)$ in Fig. 5.14 is a composite of the surface and direct path. In Stage A, the amplitude had very little variation. Subsequently, in Stage B, the amplitude starts to fluctuate. Upon examining the cyclic structure of the fluctuations, the natural frequency of the fluctuations is almost identical to the natural frequency of the waves, suggesting that the

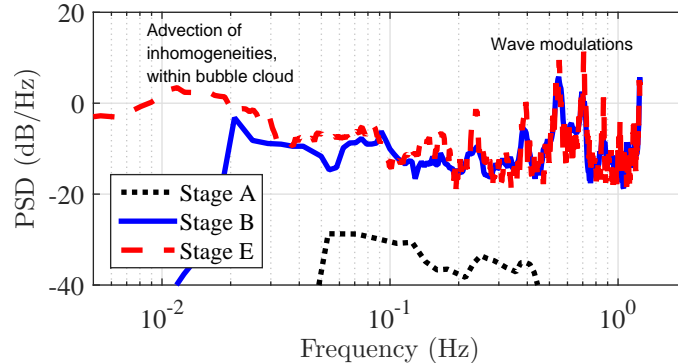


Figure 5.15: The power spectral density (PSD) of the variations. On the blue solid line is the spectra at Stage B (only waves), on the red dashed line is the spectra at Stage E (waves and micro-bubbles advection). On the black line is the spectra in Stage A (electrical noise only). The wave modulations remained the same, but the sub-hertz band is distinctly different.

cyclic fluctuation is mostly due to waves. The wave motion is integrated into the arrival because the time separation of the direct path and surface path is less than the delay time fluctuation caused by the wave motion. In Stages C and D the attenuation is high. Then at Stage E, we observe that the signal strength recovers to a steady-state. The wave modulation patterns remained the same, as the waves were controlled to be identical throughout the experiment. More importantly, the modulating envelope on a minute to minute basis is distinctly different. This is attributed to the advection of the inhomogeneous structure of the bubble clouds.

5.6.3 Spectral analysis

Fig. 5.15 shows the spectral analysis for Stage A, B and E respectively. The variations at Stage A is small, the power of the variations is at a level of around -40 dB. In Stage B and E, spectral components due to the surface waves at 0.3-0.8 Hz are identical (waves were controlled). More importantly, spectral

components at the lower frequencies from 0.1 Hz to 0.01 Hz were stronger, we attribute this to the advection of bubble clouds which have inhomogeneous bubble population in them. They have correlation time-scales in the order of minutes.

5.6.4 Mitigation

Since we observe a correlation time scale in the order of minutes, adaptive modulation may be used to mitigate against ill-effects of bubbles. Adaptive modulation requires that the channel coherence time exceed the round-trip delay time by a few orders of magnitude [8]. For a typical deployment range of a few kilometers, the round trip propagation time is in the order of seconds, while the correlation time scale of the large scale advection of bubbles is in the order of minutes. This opens up opportunities for channel conditions to be fed back to the transmitter for the scheme to be tuned accordingly.

5.7 Summary

We designed an experiment to understand the impact of bubbles on acoustic communication. We found that after a bubble injection event, the high attenuation due to dense bubble clouds typically lasted a few minutes, during which the larger bubbles rose up to the surface through buoyancy. Eventually, there was a portion of small bubbles which were suspended and remained in the water for long periods. During this phase, the bubble lifetime was governed by dissolution, a much slower process than buoyancy. These bubbles lasted longer and caused a more persistent impact on communication.

The suspended micro-bubbles can last for hours if the bubbles are stabilized

by “dirty” seawater. As the spatial effect of these bubbles can be extended as far as the currents can carry them during their long lifetimes, the suspended micro-bubbles can have an impact in places quite far from the sources of these bubbles.

Although the attenuation from the suspended micro-bubbles is usually small, they act as random moving scatterers and increase channel variability. We provided a statistical characterization of the variability in terms of its amplitude and phase distribution, as well as their time correlation. The performance of communication algorithms in such elevated variability channels is poorer, unless the algorithms specifically address the time variability. The understanding of the generation and dissipation mechanism of bubbles can enable the practitioner to design communication systems catered for the specific environment. In all, the more long-lasting impact of bubbles on communication is the rapid channel fluctuation. These are caused by micro-bubbles in the size of $100 \mu\text{m}$ and below. As such, we proceed to answer the spatial-reach of the micro-bubbles in the next chapter.

Chapter 6

Micro-bubble Advection from Shipping Lanes

In the previous chapter, we concluded that after every bubble injection, bubbles that persist are the smaller ones which are around $100 \mu\text{m}$. As these bubbles are suspended, their lifetimes are determined by the dissolution process. As such, we hypothesized that they can be advected by the currents to distant locations. The spatial-reach is thus determined by how far the currents can advect them during their dissolution lifetime. In this chapter, a model is formulated based on this idea to predict the spatial-reach of the micro-bubbles. To validate our hypothesis, we conduct an experiment within a suitable distance (based on modeling results) from the shipping lanes. During the experiment, waves of micro-bubble advection hundreds of meters away from the ships are observed. The amount of micro-bubbles is dependent on the strength of the current and the proximity of the ships to the measurement system. During a micro-bubble advection wave, the size and amount of bubbles are reduced slowly until the next wave arrives, thus suggesting simultaneous dissolution and advection processes behind the observed decay in the number of bubbles during each wave.

6.1 Collective Lifetime of Bubbles

As discussed earlier, the spatial-reach of micro-bubbles is dependent on their life-time and the strength of the advective currents. We first address the life-time

of bubbles. As seen in the previous chapter, the lifetime of a single bubble is modeled by the bubble dissolution equation [60] given by (5.9). The size reduction of one bubble due to air diffusing from the air-water boundary can be computed by:

$$a(t) = \int \frac{da}{dt} dt. \quad (6.1)$$

One can use numerical methods such as the Runge Kutta method to evaluate the integral. As bubbles seldom exist in isolation, and concurrently, the tracking of the size of each individual bubble across time is difficult, as a result, the measurement quantities usually take into consideration the bubbles as a whole. The void fraction defined in (5.1) is one such example. The time-evolution of the void fraction is generally a function of the evolution of the bubble density and the evolution of the bubble radius:

$$\eta(t) = \frac{4}{3}\pi \int_{a_{\min}}^{a_{\max}} n(a, t) a^3(t) da. \quad (6.2)$$

Given that the micro-bubbles are mainly lost through dissolution, and the evolution of one particular bubble size is given by, $a_i(t) = \int \frac{da}{dt} dt$, evaluated based on initial size from creation a_i . Therefore, the functional dependence of η with respect to a , t , and $n(a, t)$, can be simplified to:

$$\eta(t) = \frac{4}{3}\pi \int_{a_{\min}}^{a_{\max}} n_d(a) a^3(t) da. \quad (6.3)$$

Where $n_d(a)$, is the initial bubble density during the start of the suspension stage. To further elaborate, it is simpler to visualize the same equation in the

discrete domain:

$$\eta(t) \approx \frac{4}{3}\pi \sum n_d(a_i) a_i^3(t), \underbrace{[a_i - a_{i-1}]}_{\Delta a} \quad (6.4)$$

where Δa is an infinitesimally small radius bin. From the above equation, one can easily see that the collective lifetime of bubbles under the dissolution process is given by the summation of the time-evolution of bubbles in each infinitesimally small bin multiplied individually with the number of them during the initial suspension stage. Thus by knowing $a_i(t)$ and $n_d(a)$, one can easily compute the void fraction evolution, $\eta(t)$. Given that we have experimentally observed $\eta(t)$ to follow an exponential decay, $\eta(t) = \eta_0 e^{-\Gamma_u t}$, the decay constant Γ_u can be estimated by a least square estimator:

$$\Gamma_u = \arg \min_{\Gamma} \sum_{t=0}^{t=T} \left(\ln \frac{\eta(0)}{\eta(t)} - \Gamma t \right)^2, \quad (6.5)$$

where $\eta(t)$ is just a numerical evaluation of (6.3). The decay constant of the void fraction, Γ_u can be determined based on the physical parameters governing dissolution by applying (6.3) and (6.5). The bubble density at the dissolution dominated phase in Chapter 5 is determined to follow a power law, where $n_d(a) = n_0 a^{\nu_d}$, and n_0 is 6.5×10^{-11} , while $\nu_d = -3$. Based on $n_d(a)$ and the $a_i(t)$ evaluated from Table 5.3, we can easily evaluate $\eta(t)$ and thus compute Γ_u . The void fraction decay constant, Γ_u , estimated for the values in Table 5.3 results in a decay constant of 5.66×10^{-4} , or a half-life, $T_{\frac{1}{2}} = \ln 2 / \Gamma_u$ of 1300 seconds. This indicates that under pure dissolution alone, the void fraction would decrease by half every 1300 seconds (20 minutes), as shown in the evaluation results in Fig. 6.1.

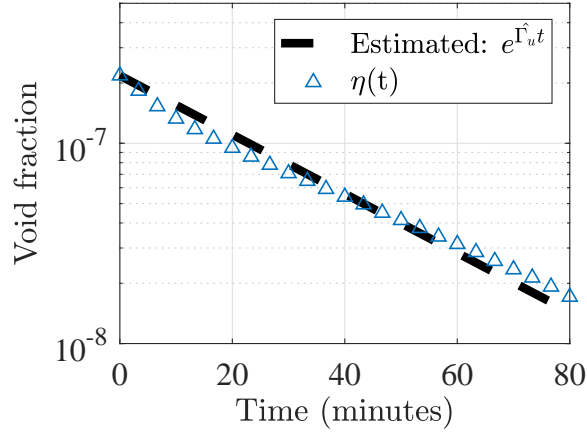


Figure 6.1: Model evaluation against estimated decay constant, Γ_u .

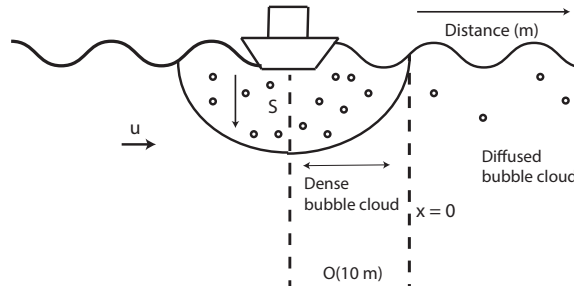


Figure 6.2: Conceptual diagram of the advected bubbles from the shipping lanes. u is the current strength.

6.2 Modeling the Spatial-reach of Micro-bubbles

The conceptual diagram for the advection of micro-bubbles is shown in Fig. 6.2. Immediately below the shipping lanes, there are clouds of dense bubbles larger than $100 \mu\text{m}$ created in great quantities. The behavior of these dense bubbles is different from the diffused micro-bubbles which are advected by currents. As the main focus is the advected micro-bubbles, the origin of the frame of reference is set at a few tens of meters away from the shipping lanes as shown in Fig 6.2. We start the frame of reference here because the larger bubbles have a buoyancy

lifetime of a few minutes, and with the current strengths measuring at typically a few cm/s, these large bubbles can at most travel a few tens of meters before surfacing. As such, the spatial scale of the large bubbles is very much smaller than the micro-bubbles. We call this the edge of the dense bubble clouds for the ease of reference. This is the location where the larger bubbles exist in quantities that are no longer significant.

On the other hand, smaller bubbles have longer lifetimes, in the order of hours, because their life-times are determined by the dissolution process which is a much slower process compared to buoyancy. As such, they can be advected to distant locations. Our objective is therefore to model the distribution of the bubbles as a function of distance from the shipping lanes:

We start from the general advection-diffusion-equation (ADE):

$$\frac{\partial \eta}{\partial t} = \left(\underbrace{-u \frac{\partial \eta}{\partial x}}_{\text{Advection}} + \underbrace{D_{td} \frac{\partial^2 \eta}{\partial x^2}}_{\text{Turbulent diffusion}} \right) + \underbrace{S}_{\text{Injections}} - \underbrace{\Gamma_u \eta}_{\text{Dissolution loss}} \quad (6.6)$$

where u is the current strength, D_{td} is the turbulent diffusion constant, S is the source amount, and Γ_u is the dissolution loss constant. The ADE captures the space and time variations of the property of interest, which in our case is the void fraction. As we are interested in the far-range region of a few hundred meters away, the travel-time of these bubbles is at least a few tens of minutes. Assuming that ships to arrive more frequently and therefore at shorter intervals as compared to the travel time of the bubbles, we expect the bubbles which are advected to these ranges to be a composite result of multiple injections by different ships. For this, we consider averaging time scales of a few tens of

minutes, within this window the time-transient of the void fraction is set to be zero:

$$\frac{d\eta}{dt} = 0. \quad (6.7)$$

As we have assumed that the source, S is an averaged injection over multiple ship injections over a few tens of minutes time-scale, the time-dependence of the source is suppressed.

$$\frac{dS}{dt} = 0, \quad (6.8)$$

and

$$\int \frac{dS}{dt} = 0 + C_s \quad (6.9)$$

where C_s is the initial void fraction. As such, the partial differential ADE with two dependent variables (6.6), (space and time) can be simplified to a time-averaged, space dependent ordinary differential equation:

$$u \frac{d\eta}{dx} = D_{td} \frac{d^2\eta}{dx^2} - \Gamma_u \eta. \quad (6.10)$$

From (6.10), one can easily deduce that one of the possible solutions is an exponential dependence of the void fraction with respect to distance from the edge of the shipping lanes:

$$\eta(x) = \eta(0)e^{\lambda_{ADD}x}, \quad (6.11)$$

To avoid confusion with the other x variable used in this thesis, we change the

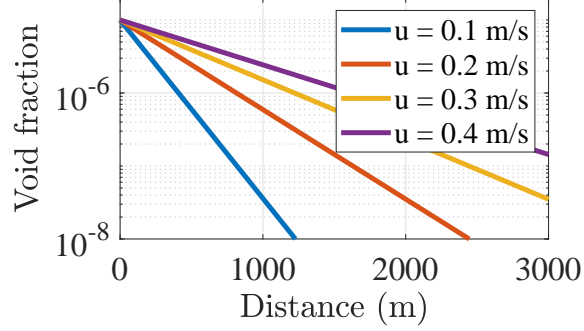


Figure 6.3: Void fraction with respect to distance from shipping lane (- O(10 m))

variable x to d_e where d_e is the distance from the edge of the dense bubble cloud.

$$\eta(d_e) = \eta(0)e^{\lambda_{\text{ADD}}d_e}, \quad (6.12)$$

While $\eta(0)$ is the void fraction at the edge of the dense bubble cloud, which is C_s . With simple algebra, the Advection-Diffusion-Dissolution (ADD) exponential loss constant, λ_{ADD} can be determined from (6.10) as:

$$\lambda_{\text{ADD}} = \frac{u - \sqrt{u^2 + 4D_{td}\Gamma_u}}{2D_{td}}, \quad (6.13)$$

where, D_{td} , the turbulent diffusivity, is a parameterization of the random motions in the ocean which causes area-wise spreading of the bubbles in both the horizontal axes. The typical horizontal turbulent diffusivity on this scale is around $0.1 \text{ m}^2/\text{s}$ [69, pp. 295]. With typical current values of 0.1–0.4 m/s (these are current strengths typically encountered in Singapore waters), and an initial void fraction of $\eta(0) = 10^{-5}$, we evaluate (6.10) to predict the spatial reach of these micro-bubbles. This is shown in Fig. 6.3. One can observe that



Figure 6.4: Experiment nodes deployment.

given typical current strength of $0.1 - 0.4$ m/s, a void fraction of above 10^{-8} at a distance of a few kilometers is possible. As such, we choose to deploy the bubble resonator at a distance of around 1 km from the center of the official shipping lanes.

6.3 Experiment Description

We conducted an experiment in the vicinity St. John Islands in Singapore on 28th November 2018. The GPS coordinate of the location was 1.22N 103.85E. The aerial view of the experimental setup is shown in Fig. 6.4. A bubble resonator was deployed to measure the advected micro-bubbles from the shipping lane. The technique to measure bubbles is the RBA as described in the previous section. The bubble resonator was suspended by a lever from the boat and submerged 1 m into the water. This is as shown in the cross-sectional view in Fig. 6.6.

The official shipping lane was around 1 km away from the bubble resonator. However, some ships come as close as 200–500 m from the bubble resonator. The

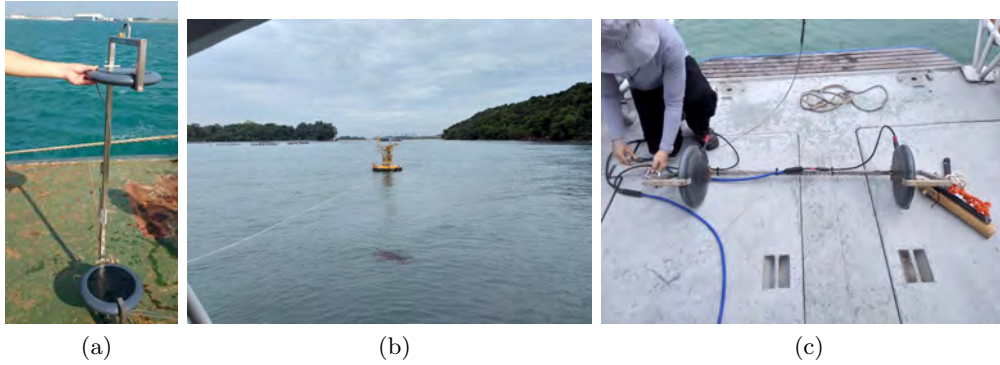


Figure 6.5: (a) Bubble resonator. (b) The buoy and Node C. (c) Deploying the bubble resonator.

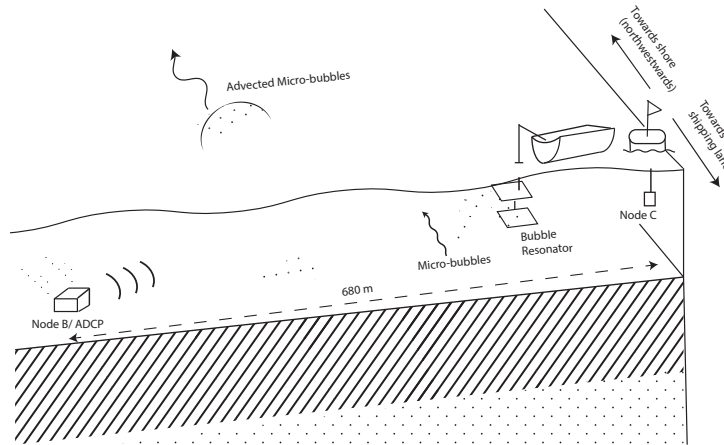


Figure 6.6: Cross-sectional view of the communication nodes deployment.

GPS locations of all the ships passing by the shipping lanes were recorded by an Automatic Identification System (AIS) receiver. These location logs were further processed to obtain the distance of all the ships at all times from the bubble resonator. Node B and Node C marked on the map were the acoustic modems whose data are analyzed in the next chapter. The ADCP which recorded the currents profile was bottom mounted together with Node B. The cross-sectional view of the deployment is shown in Fig. 6.6. Some photos of the deployment are shown in Fig. 6.5.

6.4 Experiment Results

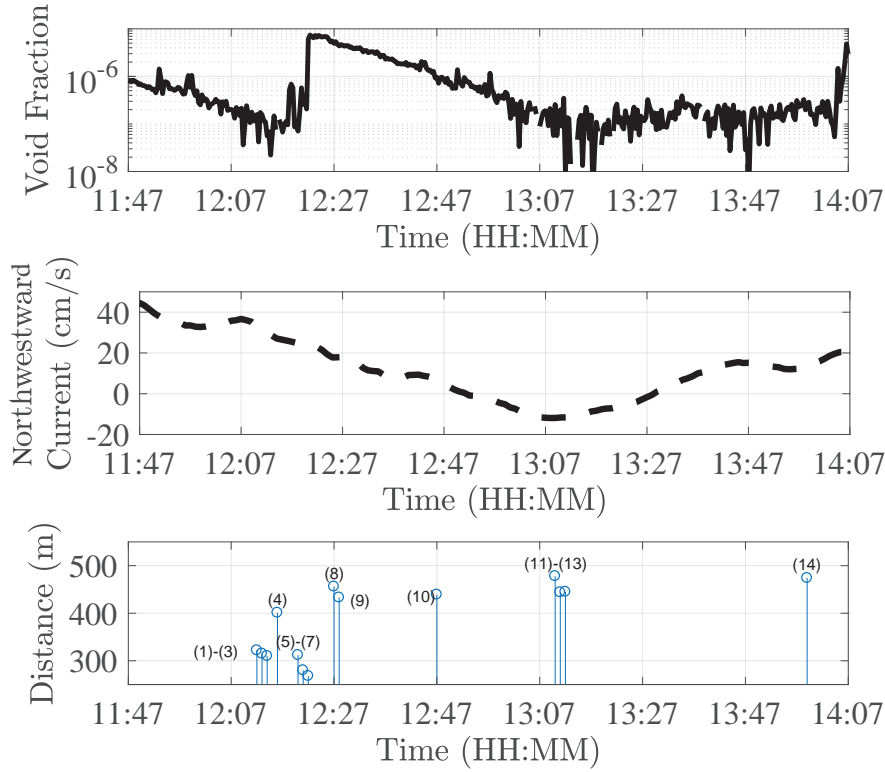


Figure 6.7: The upper panel is the void fraction measured on the bubble resonator. The middle panel is the current measurement from the ADCP. The lower panel is the ship arrivals from the AIS data. Distance is calculated as the nearest distance of the ship from the bubble resonator.

The measurement results are shown in Fig 6.7. On the upper panel is the void fraction measured on the bubble resonator. We started the bubble measurement at 11:47 am. On the middle panel, the current measurements are time-synchronized to the bubble measurements. The current is projected northwestward which points from the shipping lane towards the direction of the island. On the lower panel, we show the ship arrivals from the AIS data. We show ships which arrive within 500 m of the bubble resonator. We list all 14

ships which passed by with labels 1–14, and show their nearest distances from the bubble spectrometer on the vertical axis in the lower panel of Fig. 6.7. The Maritime Mobile Service Identity (MMSI) and images of these ships are all given in Fig. 6.8. Among the 14 ships, there is one USA warship (label 6) and one USA aircraft carrier (label 8) which passed by the straits of Singapore on that day.

During the measurements, we observed two waves of advected micro-bubbles. The first wave was seen at 11:47 am. We believe this is due to a previous advection wave which passed through the bubble resonator, and we were only observing the tail end of the advection wave. After the first wave subsided, the second advection wave started at 12:20 pm. The void fraction surged to a level of 5×10^{-6} and slowly decayed. We believe that this is due to advection and dissolution processes at work concurrently. Further, the void fraction was dependent on both the ship arrivals and currents. The ships created the bubbles and the currents advected them into the channel. One can observe that the second advection wave was triggered when there was a sudden burst of ship arrivals in the shipping lanes (labels (1)-(7)). During this time, the currents were moving in the direction from the shipping lane towards the bubble resonator, and after some time, the void fraction measured with the bubble resonator at 300 m away surged. We believe that the observed delay is due to the advection of bubbles over a distance of approximately 300 m to 400 m. In Fig. 6.9, which depicts the bubble spectral densities measured, one can see that during both the advection waves, the observable bubble sizes diminished slowly, indicating that bubbles from the shipping lane dissolved slowly as they were being advected into

CHAPTER 6. MICRO-BUBBLE ADVECTION FROM SHIPPING LANES

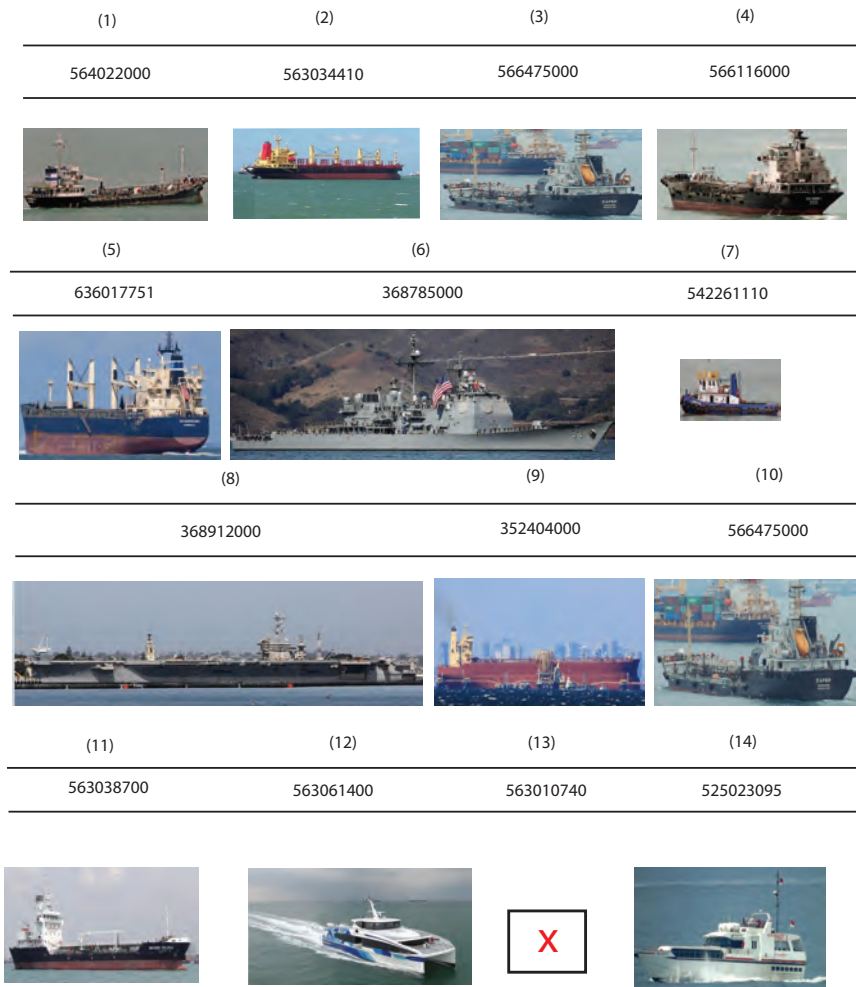


Figure 6.8: Ships which passed through the shipping lane on the day of experiment. The ship information is retrieved from the AIS logger. In brackets are the labels, below the brackets are MSSI of the ships. The red cross indicates that there is no image available for that ship.

6.5. COMPARISON OF MODEL AND EXPERIMENTAL DATA

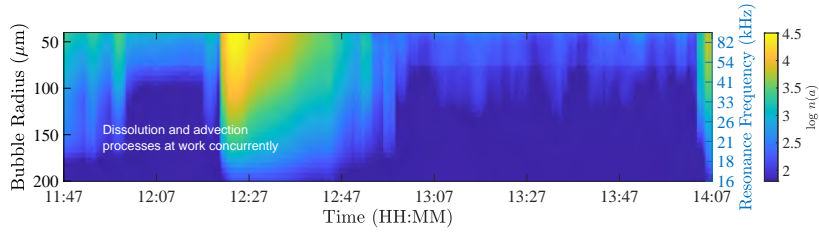


Figure 6.9: Bubble spectral density measurements.

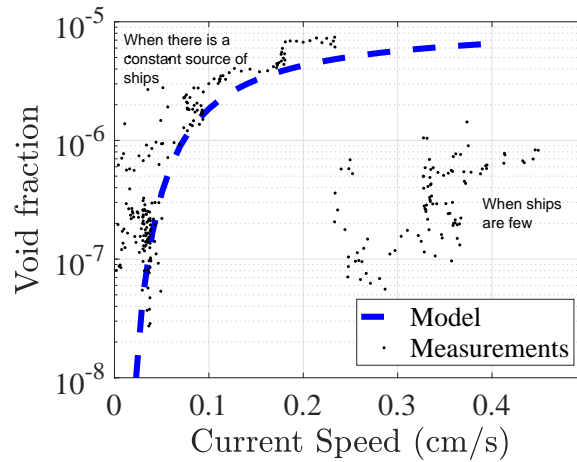


Figure 6.10: Void fraction with respect to current strength (model against experiment data), for a fix distance (300 m) from the shipping lane.

the channel. The bubble sizes that persist were in also in the order of $100 \mu\text{m}$, similar to the experiment we conducted in the previous chapter. We recognize that the bubbles during the second wave are likely a congregation of all the bubbles produced by ships (1)-(7). We see that when the currents are mild, the number of bubbles advected into the channel is comparatively less, regardless of the shipping activity.

6.5 Comparison of Model and Experimental Data

In Fig. 6.10, we show the comparison between the observed void fraction and the modeled void fraction against current strength. On the blue dash line is the

void fraction at a distance of 300 m with respect to current strength. This is obtained by fixing the range variable to 300 m and varying the current strength, u . The range of 300 m is chosen as it is the average distance of ships from the bubble spectrometer. This is estimated from the AIS logs.

The void fraction data and current strength data from Fig. 6.7 are time-aligned and plotted on the same plot. We find that during times when the ship arrivals were frequent, the model does give a good indication of the void fraction expected. However, when the ships were few, even though the currents were favorable, there were fewer bubbles to be advected and hence the void fractions were low despite the currents were high. The analytical model we propose only considers the case of constant injection and hence is representative of the experiment data when the ships are frequent.

We find that this model does give a coarse indication of the void fractions to be expected with respect to distance. However, during the experiment, the void fractions are transient with respect to time. The measured void fraction is dependent on varying currents, and the proximity of ships to the bubble resonator, and the frequency of ship arrivals. Furthermore, all these factors are time-varying in nature. Therefore using deterministic models to describe the whole process is cumbersome. We believe that a statistical description is more suitable for such a scenario. However, the experimental validation of these models would require more data over many bubble advection waves.

6.6 Summary

In the previous chapter, we hypothesized that micro-bubbles can be advected to distant locations, and the spatial reach should be determined by the extent the currents can advect them during their dissolution lifetimes. In this chapter, a model to predict the spatial reach of micro-bubbles was formulated. We found that micro-bubbles can potentially travel a few kilometers. Based on modeling, we conducted an experiment within the kilometer proximity of the shipping lanes. In the experiment, we observed micro-bubbles being advected hundreds of meters away from the ship injections. The amount of micro-bubbles is dependent on the current strengths and the proximity of the ships from the measurement system. During a micro-bubble advection wave, the size and amount of bubbles slowly reduce until the next wave arrives, thus suggesting simultaneous dissolution and advection processes behind the observed void fraction decay. Direct observation of the periodic advection of micro-bubbles thus paves the way for the analysis of the impact of these bubbles on communications which will be described in the next chapter.

Chapter 7

Impact of advected micro-bubbles on communications

In the previous chapter, we observed bubbles advected from the shipping lane. Here, we present a characterization of a class of shallow water channels where micro-bubbles advected from distance locations are known to exist.

7.1 Introduction

Standardization of channel models has been an important issue in the underwater acoustic communication community [3]. Although it has been suggested that there are no typical underwater acoustic channels, and each channel is different from one another [47], it can still be extremely useful if a few classes of channel models can be proposed along with the measurements and description of the pertinent physical process that drives the random variations. This is better than just merely performing the statistical characterizations of the channel itself, as it allows a generalization of the characterization into a class of channels that share the same physical commonality [70]. Similar efforts have also been seen in terrestrial wireless communication where channel models are sub-categorized to a few classes such as urban, suburban, mountainous and indoors channels [71]. This can be a paradigm that the underwater acoustic communications community can adopt, however, this must be done by taking into consideration the unique propagation features that only exist in the

underwater channel. In line with this effort, we characterize a class of channels in the shallow waters where micro-bubbles are known to exist due to advection from a far-away source such as a shipping lane.

7.2 Experiment Description

The experimental setup here is the same as the one described in chapter 6. We only add a few more descriptions pertaining to the communication setup here. Node B acted as the transmitter and Node C acted as the receiver. Node C was surface-mounted with a buoy at a depth of 1 m and Node B was bottom-mounted at a depth of 6 m. The experiment data we processed corresponded to the time frame from 11:15 am to 14:07 pm. We sent PN-sequence probe modulated with a BPSK scheme. The carrier frequency was 24 kHz and the data rate was 24 kbps. The PN-sequence was generated with a maximal length sequence of $m = 12$, which resulted in $N_c = (2^m - 1) = 2047$ chips. Each chip was $41.6 \mu\text{s}$ in length. The sampling rate was 1 sample per symbol.

7.3 Data Processing

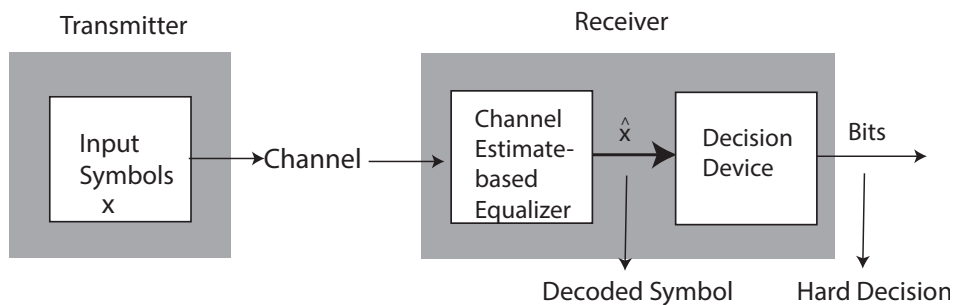


Figure 7.1: Block diagram of the signal flow.

The data processing chain is shown in Fig. 7.1. For notation purposes, we

denote vectors as lower-case boldface letters, matrices as upper-case boldface letters, while lower case letters denote scalar quantities. The superscript, $*$ represents complex conjugate transpose. The input-output relationship between the transmitted and received symbols can be written via a linear relationship:

$$\mathbf{y} = \mathbf{X}\mathbf{c} + \mathbf{n}, \quad (7.1)$$

as shown in (7.2).

$$\underbrace{\begin{bmatrix} y(0) \\ y(1) \\ y(2) \\ y(3) \\ y(4) \\ y(5) \\ \vdots \\ y(N) \end{bmatrix}}_{\mathbf{y}:(N+1) \times 1} = \underbrace{\begin{bmatrix} x(0) & 0 & 0 \\ x(1) & x(0) & 0 \\ x(2) & x(1) & x(0) \\ x(3) & x(2) & x(1) \\ x(4) & x(3) & x(2) \\ x(5) & x(4) & x(3) \\ \vdots & \vdots & \vdots \\ x(N) & x(N-1) & x(N-2) \end{bmatrix}}_{\mathbf{X}:(N+1) \times M} \mathbf{c} + \underbrace{\begin{bmatrix} n(0) \\ n(1) \\ n(2) \\ n(3) \\ n(4) \\ n(5) \\ \vdots \\ n(N) \end{bmatrix}}_{\mathbf{n}:(N+1) \times 1} \quad (7.2)$$

where \mathbf{y} is the received symbols vector, \mathbf{X} is the transmitted symbol matrix, \mathbf{n} is the noise vector. N is the number of symbols within a block, and the block length has to be longer than the delay spread of the channel, M , where M is the delay spread measured by the number of symbols it spans. The Minimum Mean

Square Estimator (MMSE) is used to first estimate the channel [72, pp. 361] .

$$\hat{\mathbf{c}} = [\mathbf{X}\mathbf{X}^*]^{-1}\mathbf{X}^*\mathbf{y}, \quad (7.3)$$

This channel estimate is applied to equalize the received signals, $\hat{\mathbf{x}} = \hat{\mathbf{c}} \circledast \mathbf{y}$.

Next, a hard decision device, which reduce the soft estimates to a binary bit:

$$D_{\text{bit}} = \begin{cases} 1, & \text{if } \hat{x} > 0 \\ -1, & \text{if } \hat{x} < -1, \end{cases} \quad (7.4)$$

is used to obtain a symbol hard decision, D_{bit} . This is used to compare the actual transmitted symbols, \mathbf{x} against D_{bit} . Bit errors are obtained from the differences. Also, for each block of soft estimates, we append a subscript, t , written as $\hat{\mathbf{x}}_t$, where t is the time index of the block, and each block consist of 2047 symbols. The input SNR estimate, γ_{SNR} for each block, γ_{SNR}^t , is based on the definition of the signal to dispersion ratio in [73].

7.3.1 Experimental Results

Hard decision analysis

We first show the hard decision results in Fig. 7.2(a). Each data point corresponds to one block. The data show a SNR variability of approximately 10 dB throughout the whole experiment of approximately 3 hours. During this time, a SNR dependent BER is observed. Also, the SNR is dependent on the time of the day which is in turn related to the number of bubbles observed. One can see that the lower performance is observed when more bubbles are

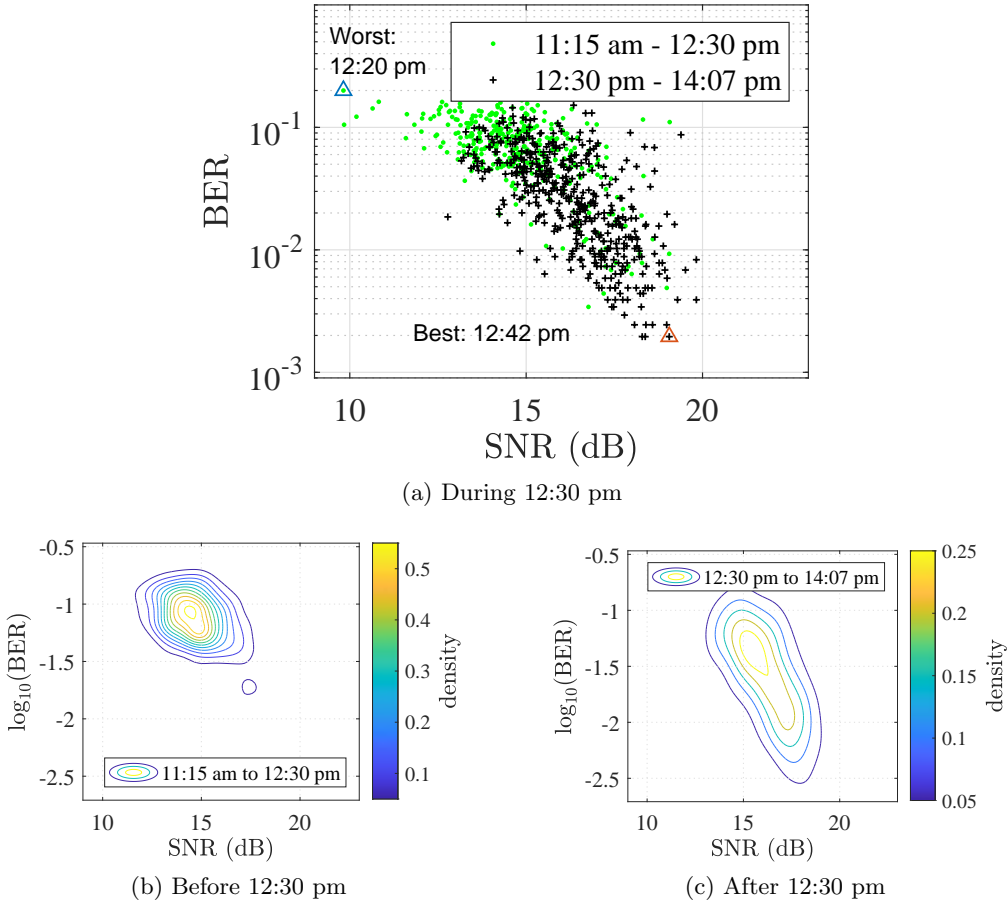


Figure 7.2: The observed BER to SNR data points during the experiment. The light green dots represent data points from the time-frame of 11:15 am to 12:30 pm where bubble advectons are observed at the bubble resonator. Whereas black crosses represent data points from the time-frame of 12:30 pm to 14:07 pm, this corresponds to the time where bubbles are observed to be fewer on the bubble resonator.

advected into the channel, while the converse is observed when fewer bubbles are observed. This thus indicates that the advected micro-bubbles scatter a portion of the signal energy and cause a drop in signal strength. One can see that the BERs and SNRs as a function of time is randomly fluctuating. This fluctuation be better represented by a two dimensional random variable. The PDF of the random variable can be estimated from the data in Fig. 7.2(a) directly. In this case, we do not assume any analytical form of the PDF. We estimate a kernel

density directly from the data, which is non-parametric description of the joint PDF of the two variables. The formula for the bivariate kernel density is given by:

$$\hat{f}_{\mathbf{H}}(\mathbf{z}) = \frac{1}{n} \sum_{i=1}^n \mathbf{K}_{\mathbf{H}}(\mathbf{z} - \mathbf{z}_i) \quad (7.5)$$

where \mathbf{z} is a bivariate random variable, $\{\mathbf{z}_1, \mathbf{z}_2\}^T$, and \mathbf{z}_1 and \mathbf{z}_2 represents BER and SNR respectively. $z_{1,i}$ is the i^{th} data point of the SNR while $z_{2,i}$ is the i^{th} data point of the BER. The Kernel density $\mathbf{K}_{\mathbf{H}}(\dots)$ used is the multivariate normal kernel density. $\mathbf{K}_{\mathbf{H}}(\mathbf{x}) = (2\pi)^{-1} |\mathbf{H}|^{-1/2} e^{-\frac{1}{2} \mathbf{x}^T \mathbf{H}^{-1} \mathbf{x}}$. \mathbf{H} is the covariance matrix. We estimated the numerical kernel density with with respect to the two variables the SNR and BER for the two time-frames where before and after 12:30 pm in Fig. 7.2(b) and (c). One can see that the data is more centred at the lower SNR-BER regime when more bubbles were found and the density is more spread out when less bubbles were found. There were still occasions of low SNR during the later period is because the bubble spectrometer only measures the bubbles at a single point in the link. Because micro-bubbles could have been advected anywhere along the link track, the occurrence of the lower SNR regime is not surprising. In Fig. 7.3, we also show the CIR before and after 12:30 pm. The CIR is obtained at a rate of 2 samples per minute. One can observe that the CIR is stronger after the two bubble advection waves. This again suggests that the bubbles scatter a portion of the signal energy. Although no new bubble cloud advection is observed from the bubble spectrometer after 12:30 pm, there are still occasionally some signal strength dips in the CIR. This is because node B (the transmitter) is nearer to the shipping lane as compared to the bubble resonator,

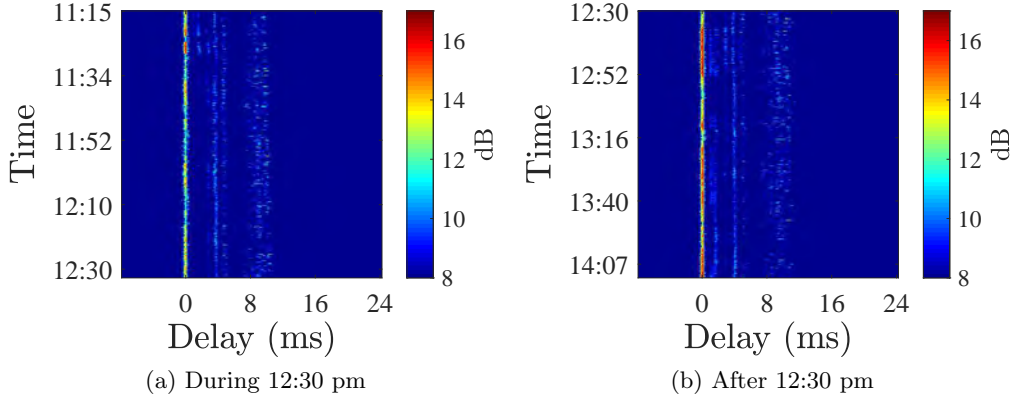


Figure 7.3: CIRs before and after 12:30 pm.

although the currents are not as strong to advect the bubbles till node C, there could still be some bubble clouds which might have been advected into the link between node C and node B. These bubbles are present in the channel but are not observable by the bubble resonator.

Intra-block variability analysis

As the delay spread is extremely long in shallow water channels, typically around 30–40 ms [74], [75],¹ the coherence bandwidth can be about 30–20 Hz. As the time-correlations of the random motion associated with these bubbles can be higher than 40 Hz as seen in chapter 5, by this, most shallow water channels with micro-bubble advection is an overspread channel by this criterion (Coherence Bandwidth < Doppler Spread). As such, other than inter-block fading, one has to consider intra-block fading (channel variability within the estimation block). The residual signal prediction error is one metric to quantify the channel variability on an intra-block basis [76]. It is defined as the remaining variability of the

¹By a 25 dB from the strongest arrival criterion.

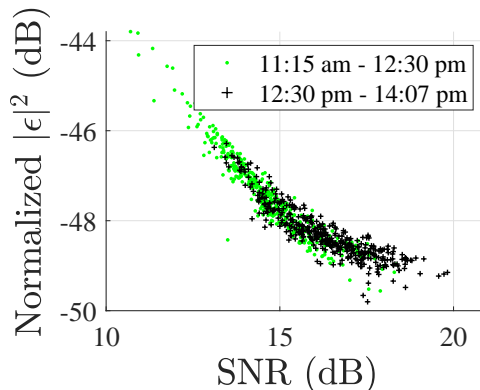


Figure 7.4: Intra-block variability

signal that is not captured in the channel estimate:

$$\epsilon^2 = |\mathbf{y} - \mathbf{x}^T \hat{\mathbf{c}}|^2 \quad (7.6)$$

This estimate has also been used to quantify the intra-packet variability in [6]. In Fig. 7.4, we show the channel variability by plotting the normalized residual signal prediction error, $|\epsilon^2|/\gamma_{\text{SNR}}$ [6], against γ_{SNR} for each probe. It can be seen that there exists an inverse relationship between the SNR and the residual prediction error. Higher residual errors and low SNRs are more likely to be observed during the period where more bubbles are observed, while the converse is true. This also suggests that other than scattering a portion of the signal energy, the bubbles also enhance the variability of the channel.

7.3.2 Noise analysis

The SNR measure used in this analysis is the signal to dispersion ratio [77] which is an SNR estimate when the noise is impulsive and follows an Symmetric

α Stable distribution (S α S) distribution. It is computed as such:

$$\text{SNR (dB)} = \gamma_{\text{SNR},i} = 10 \log_{10} \frac{P_s}{2\gamma^{2/\alpha}}, \quad (7.7)$$

where P_s is the mean square amplitude of the received signal and α is the characteristic exponent that determines the heaviness of the tail probabilities, while γ is the scale parameter, also known as the dispersion parameter, determines the spread of the distribution just as the variance in a Gaussian distribution does. We used this SNR estimate rather than the estimate when the noise is Gaussian, $10 \log_{10} \frac{P_s}{\sigma_{\text{noise}}^2}$, where σ_{noise} is the standard deviation of the noise as we observed that the measured noise is indeed impulsive. This SNR estimate is a more appropriate SNR measure when the noise is impulsive [73]. The fit of the noise data with respect to the S α S distribution and the normal distribution is shown in Fig. 7.5. We estimate the α with [78], and γ with [79]. The estimated α is 1.71 and γ is 9.6×10^{-4} . γ does not vary by more than 1% throughout the experiment. In Fig. 7.5, as compared to the Gaussian distribution, the S α S distribution is a much better model in terms of describing the tail probabilities of the data.

Statistical channel variations

We estimate the CIRs by cross-correlating the received and transmitted channel probes.

$$R_{xy}(\tau) = h(\tau) = E\{x(t)y(t - \tau)\}, \quad (7.8)$$

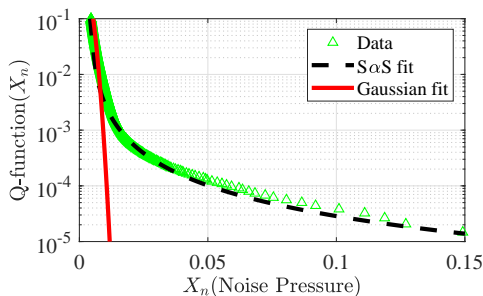
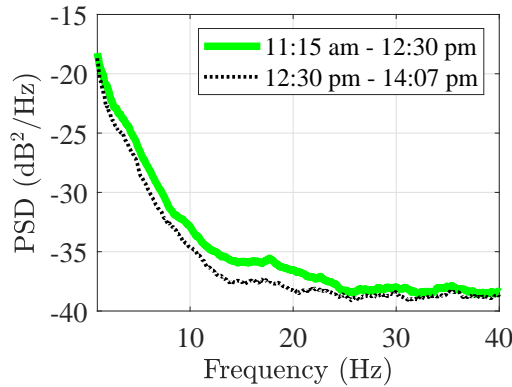
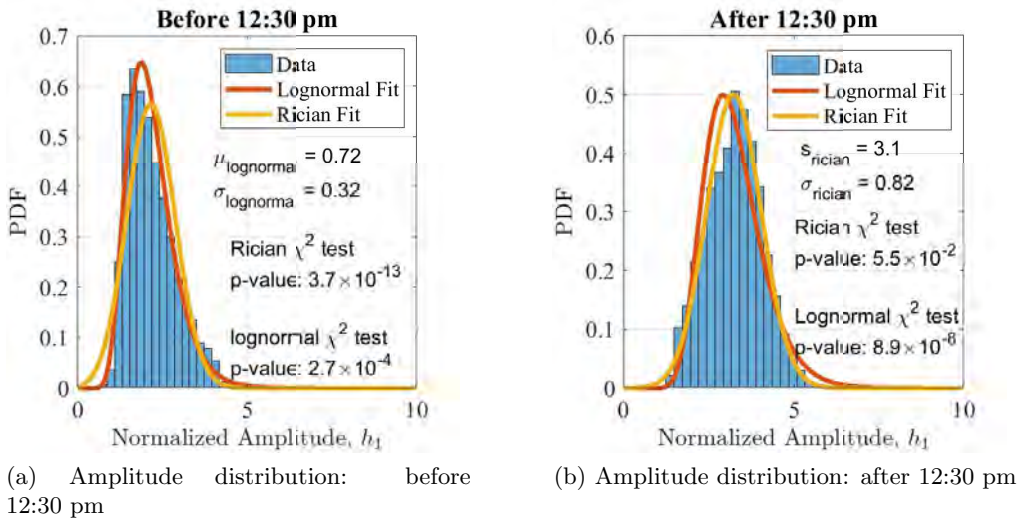


Figure 7.5: Q-function with respect to X_n . X_n is evaluated at various noise amplitude, n . $Q_x(X_n)$ is the probability that the random variable takes a value larger than n . It can be seen that the S α S distribution is a much better model in describing the tail probabilities of the data.

where $x(t)$ is the transmitted probe and $y(t)$ is the received probe. The amplitudes of the first most energetic arrival, $h(\tau_1)$ is then extracted. The channel sampling rate is 85 Hz. In Fig. 7.6(a)-(b), we show the amplitude distribution of the first most energetic arrival, $h(\tau_1)$, before and after 12:30 pm. We fit the amplitude distribution with a lognormal distribution when more bubbles are observed. Whereas when the bubbles are fewer, the data better fits a Rician distribution with a higher averaged channel amplitude. The p-values of the distribution fit are given in Fig. 7.6(a)-(b). The higher the p-value the better the fit. Although the Lognormal distribution fit is not impressive in this case, we provide a fit with this distribution based on the theoretical argument that a multiplicative concatenation of a large number of random scatterers results in a Gaussian distributed amplitude in the dB scale. In the linear scale, this translates into a Lognormal distribution. On the other hand, during low bubble population periods, the amplitude distribution follows a Rician distribution better, due to a low amount of scatterers and a stronger direct path signal contribution. The p -value of the χ^2 test for the fit of the data with the proposed

distribution is given in their respective plots. Also, in Fig. 7.6(c), we show the PSDs for the amplitudes of the first most energetic arrival before and after 12:30 pm. One can see that when more bubbles are observed, the PSD exhibit higher variations.



(c) Spectral analysis of $h(\tau_1)$ before and after 12:30 pm

Figure 7.6: Amplitude distribution and PSD of first most energetic arrival before and after 12:30 pm.

Observation of the soft estimates

In Fig. 7.7, we show the constellations for the soft estimates during the best and worst periods in the experiment. In Fig. 7.7 (a), the worst performance is

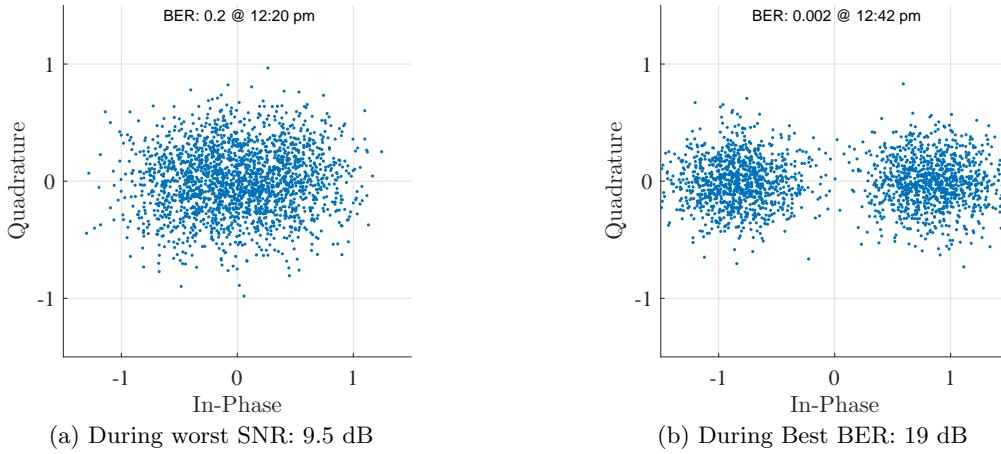


Figure 7.7: Constellation diagram of the estimated transmitted symbols by the MMSE equalizer.

shown, which is at 12:20 pm. This corresponded to the time when the second wave of bubble advection is at its strongest point. The SNR observed is 9.5 dB and the BER is 0.2. The best case is as shown in Fig. 7.7 (b) the SNR is 19 dB, the BER is 2×10^{-3} . This corresponded to the time where the advection currents were low and concurrently there were no ships in the vicinity.

7.4 Soft estimates analysis

Because the noise variance, σ_{noise}^2 did not change significantly during the experiment, most of the SNR variations are due to the changes in P_s , the received signal strength. Again, assuming that most of the variations in P_s are due to energy scattering by bubbles, we intend to determine if there are any other impact(s) other than the SNR variations we see from the experiment data.

As P_s is calculated as $P_s = \frac{\sum_{i=1}^{M_k} |y(i)|^2}{M_k}$, where M_k is the number of symbols in a block, the SNR is inherently a block-averaged based energy measure. The impact of the fast variations caused by these fast moving bubbles could be

masked off unknowingly. In this section, we intend to determine the impact of bubbles on a symbol to symbol basis. For this, we examine the distribution of the error estimates as a function of SNR regimes. The error estimates on a symbol basis is computed as such:

$$\mathbf{e}_i = \hat{\mathbf{x}}_i - \mathbf{x}_i, \quad (7.9)$$

where $\hat{\mathbf{x}}_i$ is the estimated symbol from the equalizer and \mathbf{x}_i is the actual symbol transmitted. Both $\hat{\mathbf{x}}$ and \mathbf{x} are vectors and each element of the vector is the estimated symbols $\hat{x}(t)$ and actual transmitted symbols, $x(t)$ in a transmission block. There are 2046 symbols in a block, and $i = 817$ blocks across the experiment time frame. The subscript i denotes the time index number with reference to the experiment time. During each time index, i , an SNR estimate is also calculated, γ_i^{SNR} . We examine how does the distribution of \mathbf{e}_i changes with respect to γ_i^{SNR} . In Fig. 7.8, we show a diagram describing the error estimates in the constellation diagram. We characterize the distribution of the amplitude of the error estimates $|\mathbf{e}_i|$ and angle of the error estimates $\angle|\mathbf{e}_i|$ as a function of SNR.

In Fig. 7.9(a)-(c), we show the distributions of the amplitude of the error estimates, $|e|$ for 3 SNR regimes. One can observe that all the amplitude of the error estimates for the 3 SNR regimes follow a Rayleigh distribution given by:

$$f(|e|) = \frac{|e|}{\sigma_r^2} e^{-\frac{|e|^2}{2\sigma_r^2}} \quad (7.10)$$

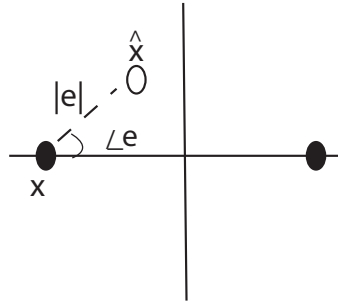


Figure 7.8: Amplitude and phase of the error estimates.

where σ_r is the standard deviation of the Rayleigh distribution and we denote $\sigma_{r,i}$ as the standard deviation for the particular SNR regime. One can see that the higher the SNR the lower the error amplitude variance. The p-values of the χ^2 test is also given in given in Fig. 7.9(a)-(c). The Rayleigh distribution fit is generally good for all SNR regimes. The p-values are smaller than 0.05, which means that the test would have pass within a 5% confidence interval. Next, in Fig. 7.10, we show the phase of the error estimates, $\angle e$ for the 3 partitions. One can see that the distribution of the phase deviates from the Gaussian distribution as the SNR deteriorates. This suggests that there exist correlations between the phase of the error estimates and the SNR. We believe that this is due to the residual phase in the carrier. This phenomenon is similar to the case of carrier phase offsets in other areas of communications, which is caused by oscillator crystal imperfections [80, pp. 620–623]. In our case, we believe that this residual phase is caused by the rapid fluctuations of the physical medium, by which random movements of the micro-bubbles is a large contributor. We find that the Von Mises distribution, which is derived from the time-dependence of the phase,

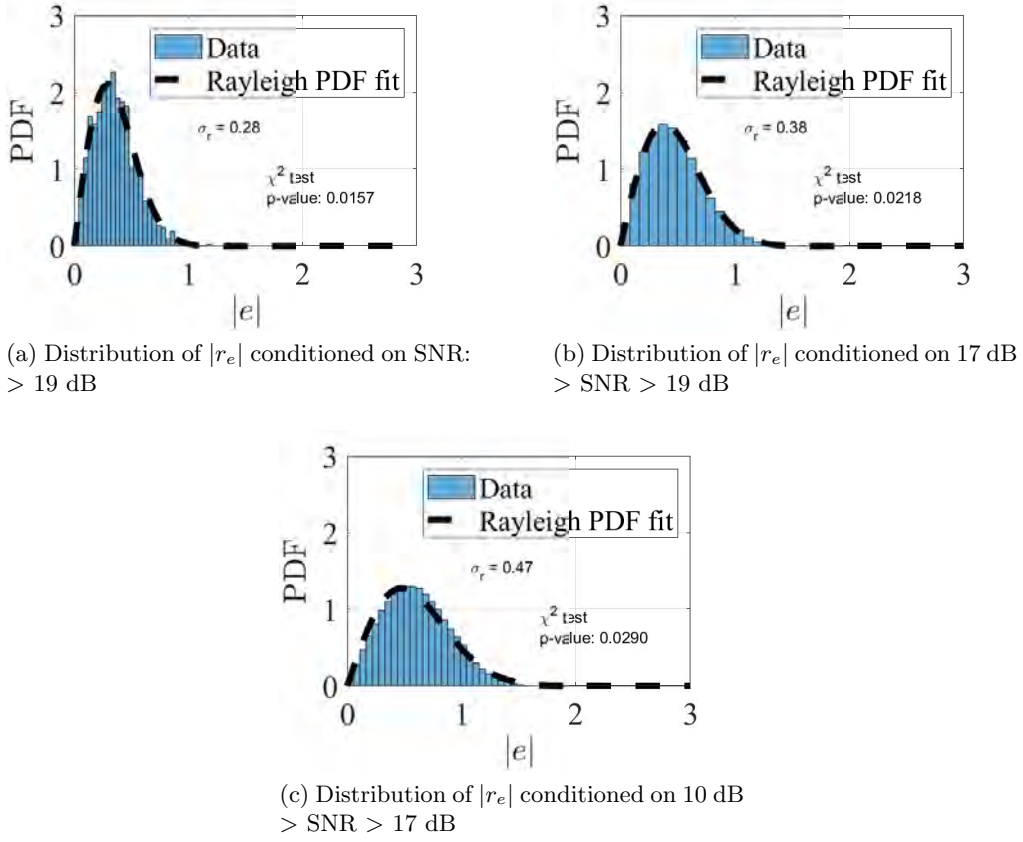


Figure 7.9: Distribution of the SDEs conditioned on various SNR regions.

fits the data well, this is shown in Fig. 7.10. The PDF of the Von Mises model is given by [81]:

$$f(\theta_r) = \frac{\exp(\beta \cos \theta_r)}{2\pi I_0(\beta)}, \text{ for } -\pi \leq \theta_r \leq \pi, \quad (7.11)$$

where β is the phase reference, which is approximately equal to the inverse of the variance of the phase, θ_r [82], while $I_0(\beta)$ is the modified Bessel function of the zero order. In Fig. 7.10, as indicated by the p-values, the Von Mises distribution provides a better fit to the phase data as compared to the Gaussian distribution for all three cases.

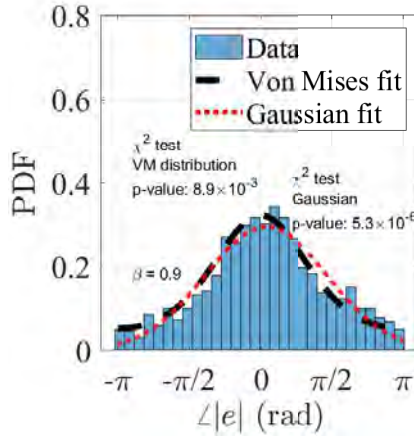
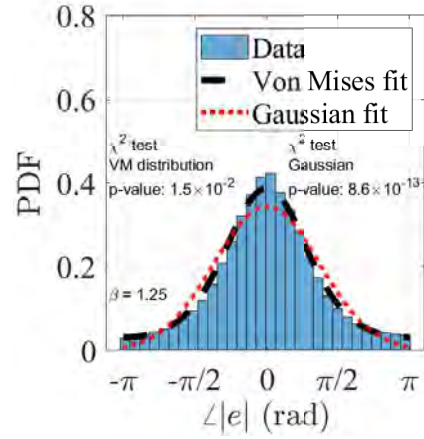
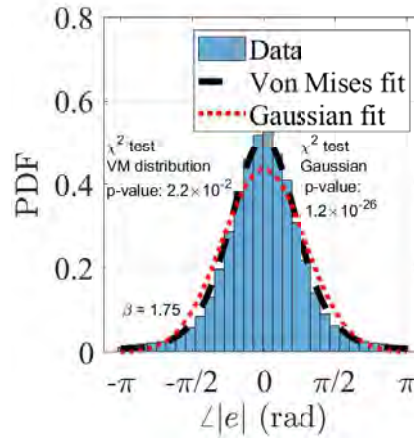
(a) Distribution of $\angle r_e$ conditioned on SNR: > 19 dB(b) Distribution of $\angle r_e$ conditioned on $17 \text{ dB} > \text{SNR} > 19 \text{ dB}$ (c) Distribution of $\angle r_e$ conditioned on $10 \text{ dB} > \text{SNR} > 17 \text{ dB}$

Figure 7.10: Distribution of the SDEs conditioned on various SNR regions.

From the data analysis, we highlight the main findings.

- The communication performance is dependent on the number of bubbles present in the medium.
- The bubbles scatter acoustic energy and decrease the SNR. Concurrently, they also increase the variability due to their cumulative random motion.
- The amplitudes fit a lognormal distribution better when more bubbles

are observed, whereas when lesser bubbles are observed, they fit a Rician distribution better.

- The distribution of the phase of the error estimates is SNR dependent. This suggest that bubbles which cause SNR dips also cause phase variability.

7.5 Long-term Channel Variations

We compute the channel gain as a function of time, $h_g(t_p)$ for each probe with:

$$h_g(t_p) = \sum_{i=1}^M h(t_p, \tau_m), \quad (7.12)$$

where, M is the total number of taps and m is the tap index, and t_p is the time index of the probe, and τ_m is the delay of the arrivals. Spectral analysis is performed on $h_g(t_p)$ with respect to the time axis to obtain $H_g(k)$ by applying the Discrete Fourier Transform.

$$H_g(k) = \frac{1}{T} \sum_{t=0}^{T-1} h_g(t) e^{-j\frac{2\pi}{T}kt}. \quad (7.13)$$

Results are shown in Fig.7.11. The measured spectrum shows two distinct trends which are watershed around the frequency of 3×10^{-3} Hz (around 5.5 minutes). For time-correlations of the signal below 5.5 minutes, we find that a simple Autoregressive (AR) model with an order of one fits the measured data well. However, the AR(1) model deviates strongly for time-correlations on the scale above 5.5 minutes. The data are fitted with the AR(1) model with coefficient p_1 of -0.97 at a sampling frequency, f_s of 1/3 seconds. Since we have observed that the micro-bubbles are long-lasting and they exist in distinct clouds,

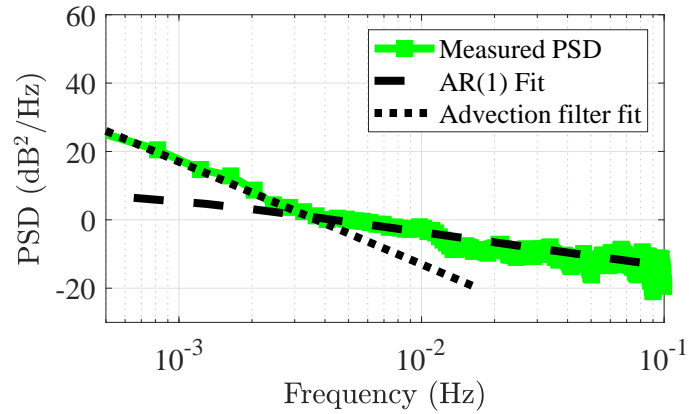


Figure 7.11: Spectral analysis of measured $H(t_p)$ and the fits of the two models. The dashed-line is the AR(1) fit, while the dotted line is the advection filter fit.

and as they are advected across the channel periodically, they are concurrently dissolving and being advected out. During this time, their cumulative population decrease with an exponential law as a function of time (See Fig. 6.7). As such, attenuation of the signal with time can also be described with an exponential law, $A(t) = A_0 e^{-\alpha_d t}$. This is illustrated in Fig. 7.12. As an exponential decay is a first-order model, the next sample in the decay should only be determined by the previous sample, therefore this explains the good fit of the channel correlations with the AR(1) model for correlations below 5 minutes. However, on a scale of

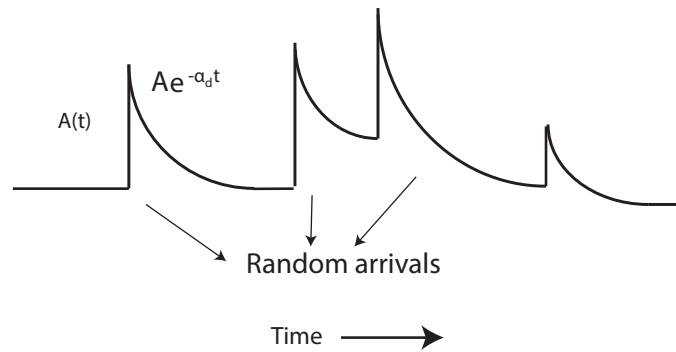


Figure 7.12: Proposed physical model for the random bubble cloud arrivals.

above 5 minutes, we deduce that the correlations are determined by large-scale advection process and the random ship arrivals which advect the bubbles into the communication channel. We propose a filter to emulate the variations on this scale. The PSD of the filter transfer function is given by:

$$S(f) = \frac{A}{1 + (f/f_m)^3}, \quad (7.14)$$

where A is fitted to be 5×10^{10} and f_m is fitted to be 10^{-6} . The sampling frequency, f_s is $1/60$, which corresponds to 1 sample per minute. The evaluation of the filter is given in the dotted line of Fig. 7.11. With the understanding of the long time-scale correlations of the channel, designers can propose adaptive strategies that work on different time-scales to mitigate the adverse effects of the channel.

7.6 Summary

In this chapter, we studied the communications signals from the field experiment. We found that the bubbles scatter a portion of the signal energy and caused a SNR variation of around 10 dB throughout the experiment. Other than the SNR dips, the bubbles also caused channel variability on an intra-block scale. We gave a statistical characterization of the channel before and after the two bubble advection waves, and we found that when more bubbles were observed, a Lognormal distribution fitted the amplitude distribution better. Whereas when fewer bubbles were observed, a Rician distribution fitted the amplitudes better. We also found that channel variability was positively correlated with the number of bubbles. Next, we gave a statistical characterization of the long-term signal

correlations. We found that correlations below 5 minutes were well modeled by an AR(1) model, which can be explained by the exponential decay of the bubbles. Correlations above 5 minutes were found to be determined by the large scale advection and random ship arrivals. A model was proposed to fit the data.

Chapter 8

The Stabilization of Micro-bubbles

In the previous chapters, we saw that the source of the ill-effects of bubbles is ultimately due to the longevity of the micro-bubbles. Surfactant stabilization was suggested as the main mechanism behind the prolonged lifetime [17]. Surfactant is a blanket term for surface-active agents which has hydrophobic tendencies (not attracted to water). These include living creatures such as micro-organism, inorganic hydrocarbon compounds, such as, ship engine oils, petrol, and also organic compounds such as amino acids, carbohydrates and fatty acids [83]. Currently, most works in the literature assume an empirically estimated discount to the known air to water diffusion constant [17],[84]–[86]. While this discount may be tuned empirically for every different environment to fit the experimental data, it does not shed light on the physical process governing the impeded dissolution process. In this chapter, we formulate a physics model to describe the surfactant stabilization process, we give an analytical expression of the dissolution in the presence of surfactants. We then show an experiment to tease the effect of surfactant stabilization and show the model agrees with the experiment data. The results can be used to explain the presence of the long-lasting bubbles observed.

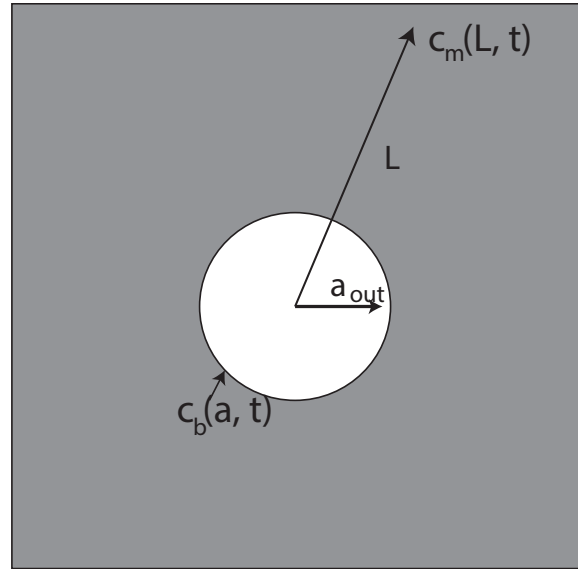


Figure 8.1: Bubble dissolution model

8.1 Theoretical Model

Consider an infinite 2-D plane as shown in Fig.8.1. The grey portion is the solvent, while the white portion is the solute. For our case, the solvent is water and the solute is air. The solute is circular with a radius a_{out} . The radius of the solvent, L is infinite. $c_b(t)$ and $c_m(t)$ are the concentrations of air (gas) in the solute and solvent respectively, these are functions with respect to time. Because the concentration of air in the bubble and the concentration of air in the water changes with time. This is because, the solute will diffuse through the air-water boundary into the solvent due to the diffusion process. The time-derivative for the concentration of the solute is proportional to its spherical size. The time-derivative is written by the Laplacian of the solute concentration.

$$\frac{dc(a, \theta, \phi)}{dt} = D\nabla^2 c(a, \theta, \phi). \quad (8.1)$$

Using the Laplacian identify formula, $\nabla^2 c(a, \theta, \phi)$ can also be written as:

$$\nabla^2 c(a, \theta, \phi) = \frac{\delta^2 c(a, t)}{\delta a^2} + \frac{2}{a} \frac{\delta c(a, t)}{\delta a}. \quad (8.2)$$

Assuming the system is in steady state, i.e. $\nabla^2 c(a, \theta, \phi) = 0$, one can see that the solution is just the Laplace solution, this is the same solution as the heat equation:

$$c(a, t) = Q_c(t) + \frac{R_c(t)}{a}, \quad (8.3)$$

where $Q_c(t)$ and $R_c(t)$ are just determined by the boundary and initial conditions. The steady state we are assuming here is taken at a very small time interval, where the a_{out} , $c_b(t)$, and the solute concentration in the solvent, $c_m(t)$ are temporarily frozen in time. The tracking of the bubble radius as it slowly decrease is repeated over the many small frozen steps subsequently.

Further, taking the boundary conditions to be: $c(a_{out}, t) = c_b(t)$, which means the gas concentration at the air-water boundary is equal to the gas concentration of air at 1 atm, i.e. $c(\infty, t) = c_m(t)$. And also, one can see that the concentration of gas in the whole medium is equal to the dissolved gas concentration in water, therefore the initial conditions can be set to be $c(a_{out}, 0) = c_b(0)$ and $c(r, 0) = c_m(0)$ where $a > a_{out}$. From this, we obtain:

$$Q_c(t) = c_m(t), \quad (8.4)$$

and,

$$R_c(t) = a_{out}(c_b(t) - c_m(t)), \quad (8.5)$$

As such, from (8.3):

$$c(a, t) = c_m(t) + \frac{a_{out}(c_b(t) - c_m(t))}{a}. \quad (8.6)$$

Also, by differentiating with respect to the radius, we obtain:

$$\left[\frac{\delta c(a, t)}{\delta a} \right]_{a,t} = \frac{c_m(t) - c_b(t)}{a}, \quad (8.7)$$

where a is the bubble radius at the current time step.

On the other hand, according to the Ideal Gas Law:

$$P_b V_b = nRT, \quad (8.8)$$

where P_b and V_b is the gas pressure and gas volume inside the bubble.

Differentiating the gas law with respect to time yields:

$$\frac{dn}{dt} = \frac{1}{RT} \frac{d(P_b V_b)}{dt}, \quad (8.9)$$

Applying the Young-Laplace Equation:

$$P_b(t) = P_h + \frac{2\sigma}{a(t)}, \quad (8.10)$$

along with the volume of the bubble:

$$V_b(t) = \frac{4}{3}\pi a(t)^3, \quad (8.11)$$

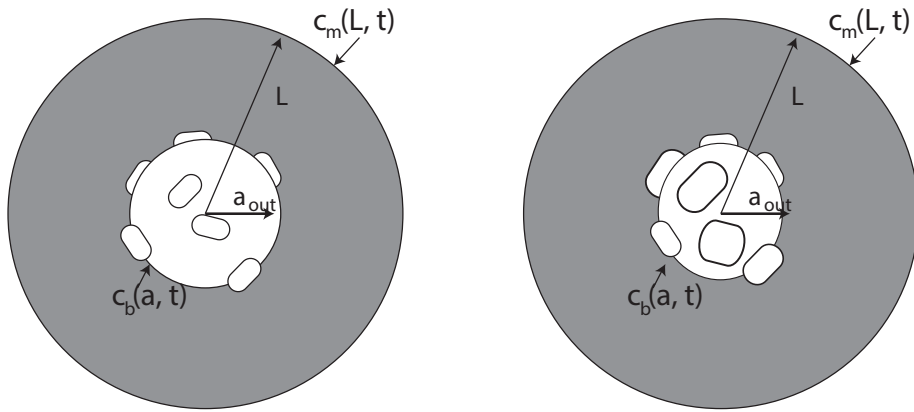
with Henry's law:

$$c(a_{out}, t) = P_b(t)/K_H, \quad (8.12)$$

By plugging (8.12) and (8.11) and (8.10) into (8.9), we obtain:

$$\frac{dn}{dt} = \frac{4\pi}{3RT} \left[3a^2 P_h \frac{da}{dt} + 4a\sigma \frac{da}{dt} \right], \quad (8.13)$$

and $\frac{dn}{dt}$ is just the mass flux out-flowing from the bubble.



(a) Initial surfactant coating

(b) After the bubble diffuses for some time

Figure 8.2: Dissolution in the presence of surfactants

Further, from Fick's Law, the mass exchange from any two mediums which has a different concentration of mass is proportional to its surface area into its concentration gradient:

$$\frac{dn}{dt} = A_S D \left[\frac{\delta c}{\delta a} \right]_{a_{out}, t}, \quad (8.14)$$

D is also known as the diffusion constant, this constant is unique for any two substances. Diffusion from air to water is empirically known to be

2×10^{-9} m²/s [61], [84]. As shown in Fig. 8.2, we can see that the surface area available for the diffusion of gas can be written as:

$$A_s = (4\pi a^2 - \epsilon(4\pi a_0^2)), \quad (8.15)$$

Where $4\pi a^2$ is the surface area of the bubble and $\epsilon(4\pi a_0^2)$ is the surface covered by surfactants, in which we assume is impermeable. The surfactant covered area is dependent on the initial radius at the creation because the larger bubbles have more tendency to coat surfactants. ϵ is just a factor that depends on the population of surfactants present in the water. One can see that just by equating (8.13) and (8.14), we get:

$$\frac{4\pi}{3RT} \left[3a^2 P_h \frac{da}{dt} + 4a\sigma \frac{da}{dt} \right] = (4\pi a^2 - \epsilon(4\pi a_0^2)) D \frac{dc}{da}, \quad (8.16)$$

the concentration gradient of $\frac{dc}{da}$ is obtained in (8.7) as:

$$\frac{dc}{da} = \frac{c_m(t) - c_b(t)}{a(t)}, \quad (8.17)$$

By the Young-Laplace Equation, we take:

$$c_b(t) = \frac{P_h + 2\sigma/a_{\text{out}}(t)}{K_H}, \quad (8.18)$$

and by Henry's Law, we take:

$$c_m(t) = P_{\text{medium}}/K_H = \gamma P_h/K_H, \quad (8.19)$$

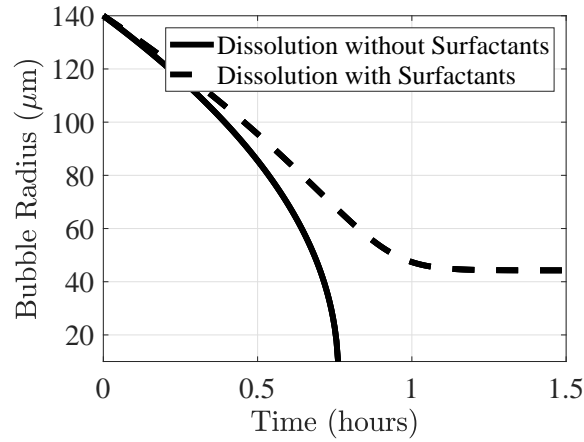


Figure 8.3: A comparison of dissolution with and without surfactants. The curves are evaluated with $\epsilon = 0.1$ which corresponds to 10% of the surface of the original bubble is coated with surfactants. The bubble stabilizes once it dissolves until the surfactant area covers the whole diffusing surface.

By substituting, (8.18) and (8.19) into (8.17), then substituting it again into (8.16), we obtain an analytical expression for the dissolution of a bubble in the presence of surfactants:

$$\frac{da}{dt} = (a^2 - \epsilon(a_0^2)) \frac{3RTD}{K_H a} \frac{P_h(\gamma - 1) - 2\sigma/a}{3a^2 P_h + 4\sigma a}, \quad (8.20)$$

In Fig. 8.3, this expression is evaluated in comparison with the standard E-P dissolution model in (5.9). The same dissolved gas concentration at 90% and a $140\mu\text{m}$ initial bubble radius is used for both evaluation: The physical parameter values used for both evaluation are shown in Table 8.1. One can easily see that the diffusion rate is slower in the presence of surfactants. Subsequently, as the surfactants cover the whole surface of the bubble, the bubble stops dissolving and is almost persistent, this happens at a radius of around $40\mu\text{m}$ at around 1 hour later. This bubble will continue to persist indefinitely until a sudden rupture.

This stabilized bubble has been experimentally observed by [87], it lasted a few days until it finally ruptured due to some random pressure forces. We examine the experimental dissolution with an experiment as described next.

TABLE 8.1: PHYSICAL PARAMETER VALUES IN (5.9) AND (8.20)

Symbol	Parameter	Value
D	Diffusivity of air in water	$2 \times 10^{-9} \text{ m}^2/\text{s}$
σ	Surface tension	0.0724 N/m
R	Universal gas constant	0.08206 atm/(mol K)
T	Temperature	293 K
K_H	Henry's law constant	1614 atm mol
γ	Dissolved gas concentration ratio	0.9
P_a	Atmospheric pressure	1 atm
ϵ	Surfactant coverage	10%

8.2 Experiment Description

8.2.1 Sampling location

We set up a controlled experiment and sampled waters from 4 locations in Singapore. This is to systematically study the effect of the properties of seawater on the lifetime of bubbles. The four locations are shown in Fig. 8.4. They are namely: the Marina, St. John Island's jetty, St. John Island's, and a coral reef island named Sisters' Island.

8.2.2 Experiment setup

There were in total 5 samples, one as a control and the other four as experiment variables. The control was artificial saltwater which has no surfactants, and the 4 experiment variables were four sampled water from various locations with different amounts of surfactants. Saltwater was used as a control instead of



Figure 8.4: Map of Singapore and the four locations where water was sampled.

freshwater because it is known that the salt would prevent coalescent of bubbles, as such smaller bubbles are generated in larger quantities after a bubble injection event [88]. The experiment setup is shown in Fig. 8.5. A metal container, 60 cm \times 30 cm is used. Two hydrophones, one as a source and the other as a receiver was used to measure absorption. The absorption was inverted for the bubble spectral density, which was then used to compute the void fractions over time. The bubble spectral density and void fraction computations were similar to the procedure as described in Chapter 5.1.2. A constant water level of 37 cm was used for every experiment run. To avoid contamination, the container was cleaned and wiped thoroughly every time the water was changed. The wooden bubble generator has pores in the micron ranges and was verified to be able to produce a majority of bubbles lying in the range of 200 μm to 20 μm . This is verified from the image analysis in Chapter 4.1. A flow generator was turned on at around 30 -35 L/minute. The wooden bubble generator was connected to an air pump with a flow rate of around 1 - 2 L/minute.

8.2. EXPERIMENT DESCRIPTION

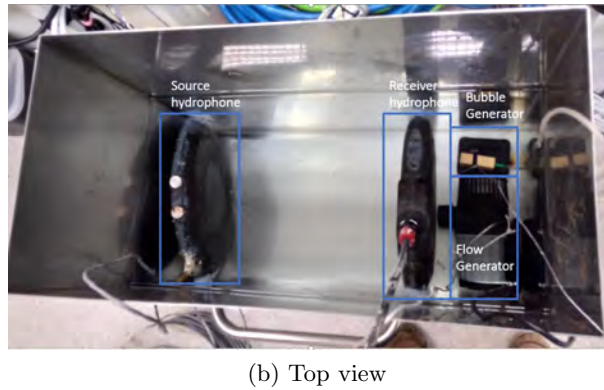
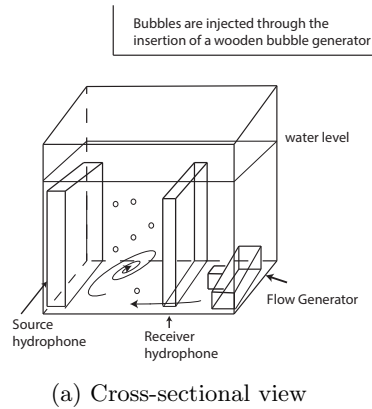


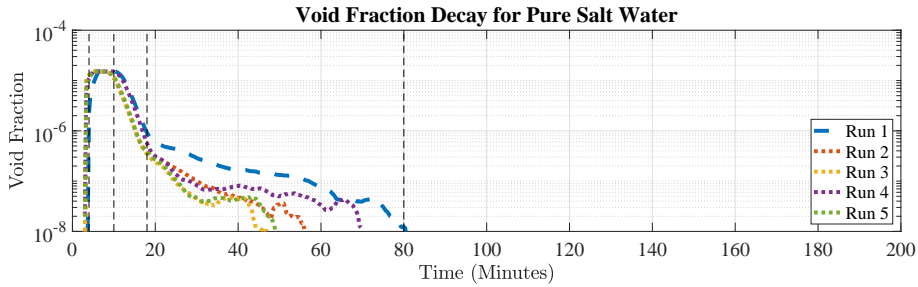
Figure 8.5: Stabilization experiment setup

8.2.3 Experiment procedure

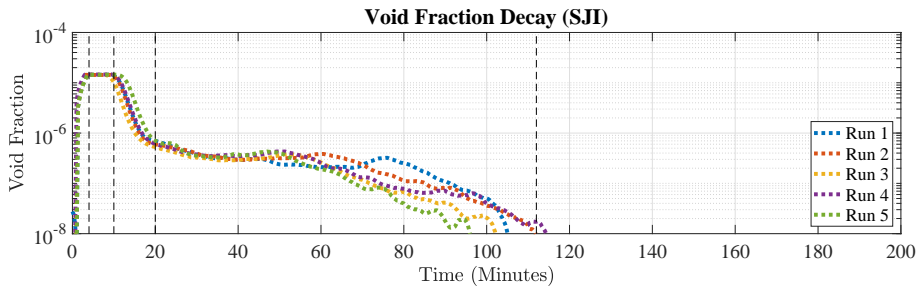
Artificial saltwater of 35 ppt salinity was prepared by adding the right amount of salt into pure water. The volume of water was: $37 \text{ cm} \times 30 \text{ cm} \times 60 \text{ cm} = 66.6$ liters of water. To make 35 ppt of salinity, we added 2.3 kg of salt ($66.6 \times 35 \text{ g of salt} = 2.3 \text{ kg}$). We stirred the solution for 3 hours and used a conductivity sensor to confirm the salinity. The actual conductivity values matched the targeted salinity within 5 %. We turned on the flow generator to simulate ocean turbulence. We then inserted a wooden bubble generator connected to an air pump to generate bubbles for 5 minutes. We removed the bubble generator and let the bubbles decay without further injection. We

repeated this procedure 5 times. The dissolved gas concentration was always set at 100 % during the start by using a dissolved oxygen sensor to measure the dissolved oxygen in the water before every run.

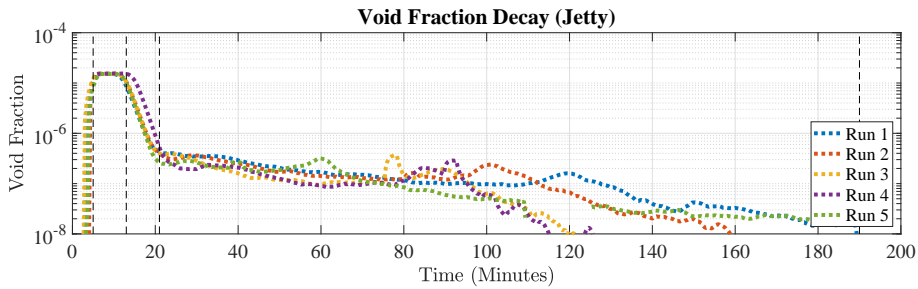
8.2.4 Experiment results



(a) Experiment results: artificial pure salt water



(b) Experiment results: St. John Island



(c) Experiment results: Jetty

Figure 8.6: Stabilization Experiment Results (1)

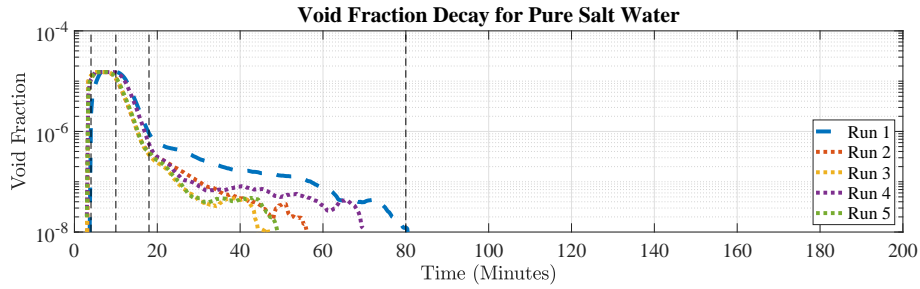
We show the experiment results in Fig. 8.6 and Fig. 8.7. Between the first two vertical dotted lines marks the injection phase. Injection is for 5 minutes, then bubble generator is removed. Subsequently, marked between the second

and third dotted lines, one can see that the void fraction drops drastically, this is the buoyancy dominated phase. The void fraction decays rapidly due to large bubbles surfacing. The time-frame of the buoyancy dominated phase is independent of the sample water, this is because the amount of surfactants has a negligible effect on the buoyancy of the larger bubbles. After around 5 minutes, the void fraction stabilizes at somewhere around 10^{-7} and starts to slowly decay. This is the dissolution dominated phase. This is marked by the third and fourth dotted lines. One can easily see that the duration of the dissolution dominated phase is highly dependent on the sample water. This is because the dissolution process itself is dependent on the surfactants population of the water.

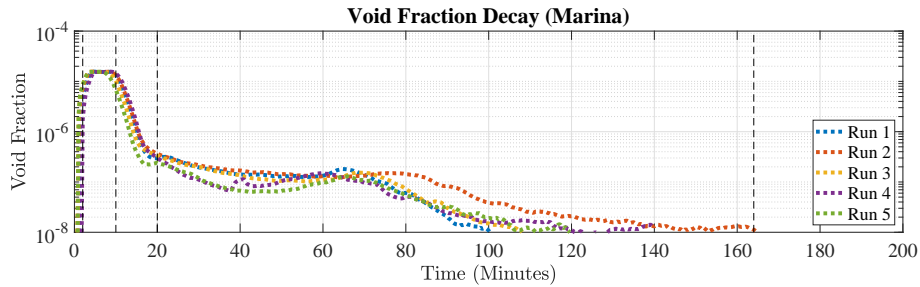
One can observe that bubbles in pure saltwater have the shortest collective lifetime. The void fraction decays to 10^{-8} in around 30–60 minutes. There are variations in the bubbles' lifetime in each run because the number of bubbles which are fully coated with surfactants is different in each run. Other than the surfactant population, the dissolution lifetime of bubbles is also dependent on the dissolved gas concentrations. Although we ensured that the dissolved gas concentration is always at 100 % before the start of the experiment. The dissolved gas concentration hardly stays constant throughout the whole dissolution lifetime, which is due to the temperature difference that causes gas exchange between the water and atmosphere.

For sampled water from various locations, we see that the dissolution dominated phase is always longer than that of the pure saltwater. The longest length of dissolution lifetime is around 3 hours, this is for the water at Coral Reef Island (Sisters' Island). We suspect this is due to the higher number of

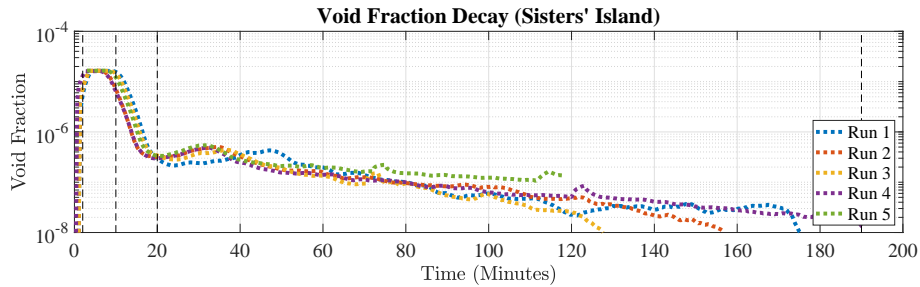
microorganisms in the coral reefs. Microorganisms are also a form of surfactant. From this, we can see that the lifetime of a bubble can be prolonged significantly by stabilizing factors in the ocean.



(a) Experiment results: artificial pure salt water



(b) Experiment results: Marina



(c) Experiment results: Sisters' Island

Figure 8.7: Stabilization Experiment Results (2)

8.3 Comparison between Theory and Experiment

To compute the void fraction decay under stabilized bubbles, we use equation (6.4) to compute the void fraction decay with respect to time. Instead of using the E-P dissolution model (5.9) which doesn't take into account surfactants, we

8.3. COMPARISON BETWEEN THEORY AND EXPERIMENT

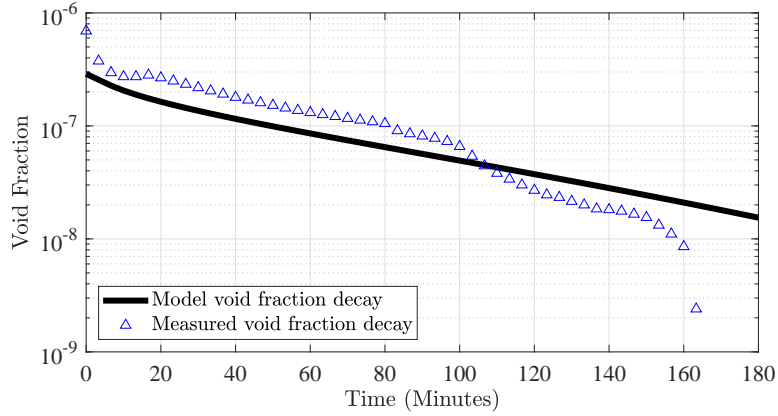


Figure 8.8: Stabilized void fraction decay model vs. experiment data observation

generated $a_i(t)$ with the stabilized dissolution model in (8.20). We used $n_d(a) = n_0 a^{\nu_d}$, where n_0 is 6.5×10^{-11} , and $\nu_d = -3$, this is the bubble density power law fit at the start of the dissolution dominated phase. We used a Δa of $1 \mu\text{m}$ and we used an ϵ of 5%. For comparison, we used the data from the void fraction decay of Sisters' Island (Run 3). In Fig. 8.8, we show the comparison between data and model, one can observe that the surfactant stabilized dissolution model explains the data well until the 150th minute. The modeling results continue to persist at a level of 10^{-8} for an indefinite amount of time, as the model assumes that all the bubbles during the suspension stage are stabilized and do not dissolve anymore. However, the data suggest a sudden decrease in void fraction after the 150th minute. This could be due to the stabilized bubble experiencing a sudden rupture. In all, the actual lifetime of the bubbles is highly variable, depending on the number of bubbles being fully coated with surfactants. The theoretical modeling result opens up the possibility for the bubble to last longer in the presence of surfactants.

8.4 Summary

From the experiments, the bubbles' lifetime in "dirty" seawater with surfactants can be as long 3 hours, this is much longer than the 1 hour in saltwater without surfactants. While the standard dissolution theory predicts the bubble's lifetime for pure saltwater well, it does not explain the 3-hour long lifetime in "dirty" seawater. This is because the standard dissolution theory was never meant to describe dissolution in the presence of surfactants. Our theory of surfactant stabilization through a partial coating can be an explanation for the observed bubble lifetime, as it predicts a bubble persistence of more than 1 hour. As the bubbles' lifetime is now much longer, this will have an impact on the spatial-reach of the bubbles, because these bubbles can now survive advection by currents for a longer period and thus can reach further distances.

Chapter 9

Conclusions & Future Research

9.1 Conclusions

In this thesis, a few questions on the impact of bubbles on acoustic communications were answered. We first answered the question behind the longevity of the bubbles. After the creation of bubbles, we found that while larger bubbles surface rapidly, micro-bubbles persist. These bubbles stayed longer and their lifetimes are determined by the dissolution process. We found that through the stabilization effect which impedes the dissolution of bubbles, the lifetime of these bubbles could reach 3 hours. The impact of these micro-bubbles on acoustic communication is the increased rapid channel fluctuations. As the lifetime of the small bubbles is long, so do the persistence of the rapid channel variations. Statistical characterization of the channel fluctuations was also given.

Next, we answered the question regarding the spatial extent of bubbles. As micro-bubbles have the potential to last for long periods, we predicted that they could be advected by currents to distant locations. A model was formulated to predict the spatial extent of bubbles and a relationship between the number of bubbles with respect to distance from the shipping lane was obtained. When we conducted an experiment within the kilometer proximity of the shipping lanes, we observed that when the currents were favorable, these bubbles can be found

in amounts as predicted by the models we proposed.

Subsequently, we showed the communication performance in the channel affected by advected bubbles from the shipping lanes. The BER performance was correlated to the number of bubbles found in the channel. Although BER performance is dependent on SNR, it is not the sole determinant. The BER is also determined by the rapid channel fluctuations in which bubbles are the main contributor. Next, a statistical characterization of the long-time-scale correlations is also given. These correlations can be useful in designing adaptive strategies.

Further, since we found that the source of the ill-effects of bubbles was due to the longevity of the bubbles, we conducted a systematic study on the effect of the stabilization process on the bubbles. We gave a theoretical analysis and obtained a new expression for the theoretical dissolution of a single bubble in the presence of surfactants. A controlled experiment was conducted and it was found that the measured lifetime of bubbles can be explained by the theoretical predictions.

In all, we provided an understanding of the physics pertaining to the effect of bubbles on underwater acoustic communication. We also quantified the impact of bubbles on communications measured in the field. The models we proposed could be used for a class of channels where intermittent bubble injections are present. These could be places of low wind, coral reefs or places in the proximity of shipping lanes.

9.2 Future Research

9.2.1 Mitigating the Impact of Bubbles

Channel coding

In chapter 7, we characterized the impact of bubbles. We know the impact of bubbles is reflected in the rapid channel variations and SNR fluctuations. However, communication strategies to mitigate the impact has yet to be addressed. We believe that channel coding can mitigate the impact of rapid channel fluctuations. However, the choice of code and code length has to be chosen in a way based on the channel characterization. This is one possible solution to address rapid variations.

Adaptive strategies

In chapter 7, we illustrated the time-correlation of the signals in the scale of minutes which is related to the advection and dissolution of bubbles. As the feedback time for a typical acoustic link is in the order of seconds, this opens an avenue for the channel to be fed back to the transmitter for the modulation scheme to be tuned. The choice of modulation scheme and how frequent the adaptation should be performed are topics that should be addressed in the future.

Networking solutions

In an underwater acoustic network, whenever a certain link encounters a degradation due to bubbles. The affected link should be automatically detected and rerouted.

Disruption Tolerant Networks (DTN)

The problem of unreliable communication links can be addressed by DTN. The nodes should have the ability to store the information and send it at a later time. Understanding how long the degradation persists is important for the design of the network.

Bibliography

- [1] E. C. Monahan, "Natural physical sources of underwater sound: A model for variations in the range and depth dependence of the sound speed and attenuation induced by bubble clouds under wind-driven sea surfaces," *B. R. Kerman Ed. Boston, MA: Kluwer*, 1993.
- [2] J. Partan, J. Jurose, and B. N. Levine, "Proceedings of the first acm international workshop on underwater networks,," in *WUWNet 2006*, 2006.
- [3] A. Song, M. Stojanovic, and M. Chitre, "Editorial: Underwater acoustic communications: Where we stand and what is next?" *IEEE J. Ocean. Eng.*, vol. 44, no. 1, 2019.
- [4] M. Chitre, K. Pelekanakis, and M. Legg, "Statistical bit error trace modeling of acoustic communication links using decision feedback equalization," *IEEE J. Ocean. Eng.*, vol. 38, 2013.
- [5] P. Qarabaqi, "Statistical characterization of a class of underwater acoustic communication channels," Ph.D. dissertation, MIT, 2014.
- [6] T. C. Yang, "Properties of underwater acoustic communication channels in shallow water," *J. Acoust. Soc. Amer.*, vol. 131, 2012.
- [7] M. Chitre and G. Chua, "Modeling realistic underwater acoustic networks using experimental data," in *Conference Record - Asilomar Conference on Signals, Systems and Computers*, 2015.
- [8] P. Qarabaqi and M. Stojanovic, "Adaptive power control for underwater acoustic communications," in *OCEANS 2011 IEEE - Spain*, 2011.
- [9] R. Andreja, A. Rameez, D. M. Tolga, J. G. Proakis, and M. Stojanovic, "Adaptive ofdm modulation for underwater acoustic communications: Design considerations and experimental result," *IEEE J. Ocean. Eng.*, vol. 39, 2014.
- [10] B. Mauro, R. Stefano, and C. Roberto, "Channel estimation or prediction for uwa?" in *OCEANS-Bergen, 2013 MTS*, 2013.
- [11] S. Shankar and M. Chitre, "Tuning an underwater communication link," in *2013 MTS/IEEE OCEANS - Bergen*, 2013.
- [12] P. Anjani and M. Chitre, "Model-based data-driven learning algorithm for tuning an underwater acoustic link," in *Underwater Communications Networking (Ucomms 2018) Lerici*, 2018.
- [13] M. Stojanovic, J. A. Catipovic, and J. G. Proakis, "Phase-coherent digital communications for underwater acoustic channels," *IEEE J. Ocean. Eng.*, vol. 19, no. 1, 1994.
- [14] H. Medwin, "In situ acoustic measurements of microbubbles at sea," *J. Geophys. Res.*, vol. 82, no. 6, pp. 971–976, 1977.
- [15] —, "Acoustical determination of bubble size spectra," *J. Acoust. Soc. Amer.*, vol. 62, p. 1041–1044, 1977.
- [16] N. Breitz and H. Medwin, "Instrumentation for *in-situ* acoustical measurements of bubble spectra under breaking waves," *J. Acoust. Soc. Amer.*, vol. 86, pp. 739–743, 1989.

BIBLIOGRAPHY

- [17] S. A. Thorpe, "On the clouds of bubbles formed by breaking wind-waves in deep water, and their role in air sea gas transfer," *Philosophical Transactions of the Royal Society of London. Series A Mathematical and Physical Sciences*, vol. 304, no. 1483, 1982.
- [18] H. Medwin and A. C. Daniel, "Acoustical measurements of bubble production by spilling breakers," *J. Acoust. Soc. Amer.*, vol. 88, no. 1, p. 411, 1990.
- [19] M. D. Anguelova and P. Huq, "Characteristics of bubble clouds at various wind speeds," *J. Geophys. Res.*, vol. 117, 2011.
- [20] A. L. Walsh and P. J. Mulhearn, "Photographic measurements of bubble population from breaking waves at sea," *J. Geophys. Res.*, vol. 92, no. 13, 1987.
- [21] S. Baldy, "Bubbles in the close vicinity of breaking waves' statistical characteristics of the generation and dispersion mechanism," *J. Geophys. Res.*, vol. 93, no. C7, 1988.
- [22] H. Medwin and N. D. Breitz, "Ambient and transient bubble spectral densities in quiescent seas and under spilling breakers," *J. Geophys. Res.*, vol. 94, no. C9, 1989.
- [23] I. Leifer and G. D. Leeuw, "Bubbles generated from wind-steepened breaking waves: 1. bubble plume bubbles," *J. Geophys. Res.*, vol. 111, 2006.
- [24] E. Lamarre and W. K. Melville, "Void-fraction measurements and sound-speed fields in bubble plumes generated by breaking waves," *J. Acoust. Soc. Amer.*, vol. 95, no. 3, p. 1317, 1994.
- [25] —, "Air entrainment and dissipation in breaking waves," *Nature*, vol. 351, p. 469, 1991.
- [26] J. Wu, "Individual characteristics of whitecaps and volumetric description of bubbles," *IEEE J. Ocean. Eng.*, vol. 17, p. 150, 1992.
- [27] C. E. Blenkinsopp and J. R. Chaplin, "Bubble size measurements in breaking waves using optical fiber phase detection probes," *IEEE J. Ocean. Eng.*, vol. 35, no. 2, p. 388, 2010.
- [28] E. C. Monahan and M. LU, "Acoustically relevant bubble assemblages and their dependence on meteorological parameters," *IEEE J. Ocean. Eng.*, vol. 15, no. 4, p. 340, 1990.
- [29] G. B. Deane and M. D. Stokes, "Scale dependence of bubble creation mechanisms in breaking waves," *Nature*, vol. 418, pp. 839–844, 2002.
- [30] M. Ainslie, "Effect of wind-generated bubbles on fixed range acoustic attenuation in shallow water at 1-4 khz," *J. Acoust. Soc. Amer.*, vol. 118, no. 6, pp. 3513–3523, 2005.
- [31] J. Novarini, R. Keiffer, and G. Norton, "A model for variations in the range and depth dependence of the sound speed and attenuation induced by bubble clouds under wind-driven sea surfaces," *IEEE J. Ocean. Eng.*, vol. 23, no. 4, pp. 423–438, Jan 1998.
- [32] M. Hall, "A comprehensive model of wind-generated bubbles in the ocean and predictions of the effects on sound propagation at frequencies up to 40 khz," *J. Acoust. Soc. Amer.*, vol. 86, no. 3, p. 1103, 1989.

-
- [33] R. Vossen and M. Ainslie, “The effect of wind-generated bubbles on sea-surface backscattering at 940 hz,” *J. Acoust. Soc. Amer.*, vol. 130, no. 5, p. 3413, 2011.
- [34] S. Mcdaniel, “Vertical spatial coherence of backscatter from bubbles,” *J. Acoust. Soc. Amer.*, vol. OE-12, no. 2, 1987.
- [35] K. Sarkar and A. Prosperetti, “Coherent and incoherent scattering by oceanic bubbles,” *J. Acoust. Soc. Amer.*, vol. 96, no. 1, 1994.
- [36] P. A. Kolavayev, “Investigation of the concentration and size distribution of wind-produced bubbles in the near-surface ocean layer,” *Oceanology*, vol. 16, 1976.
- [37] B. D. Johnson and R. C. Cooke, “Bubble populations and spectra in coastal waters: A photographic approach,” *J. Geophys. Res.*, vol. 87, 1979.
- [38] R. Wildt, *Physics of sound in the sea*,. National Defense Research Committee, Tech. Rep. Div. 6. Summary, 1949, vol. 8.
- [39] M. V. Trevorrow, “Acoustical measurements of microbubbles within ship wakes,” *J. Acoust. Soc. Amer.*, vol. 95, no. 4, p. 1922, 1994.
- [40] S. Vagle and H. Burch, “Acoustic measurements of the sound-speed profile in the bubbly wake formed by a small motor boat.” *J. Acoust. Soc. Amer.*, vol. 117, 2005.
- [41] S. Stanic, J. Caruthers, R. R. Goodman, E. Kennedy, and R. A. Brown, “Attenuation measurements across surface-ship wakes and computed bubble distributions and void fractions,” *IEEE J. Ocean. Eng.*, vol. 34, no. 1, Jan 2009.
- [42] C. A. Boyles, A. P. Rosenberg, and Q. Zhang, “Modeling the effect of bubble plumes on high frequency acoustic propagation in shallow water,” in *IEEE/MTS 2013 OCEANS - San Diego*, 2013.
- [43] —, “Underwater acoustic communication channel characterization in the presence of bubbles and rough sea surfaces,” in *OCEANS 2011 IEEE - Spain*,, 2011.
- [44] K. Saraswathi, S. Ravishankar, and V. Singh, “Underwater communications in the presence of bubbles and doppler shift.” in *2017 International Conference on Advances in Computing, Communications and Informatics, ICACCI 2017*, 2017.
- [45] A. K. Mandal, S. Misra, T. Ojha, M. K. Dash, and M. S. Obaidat, “Effects of wind-induced near-surface bubble plumes on the performance of underwater wireless acoustic sensor networks,” *IEEE Sensors Journal*, vol. 16, 2016.
- [46] H. S. Dol, M. Colin, M. Ainslie, P. A. Walree, and J. Janmaat, “Simulation of an underwater acoustic communication channel characterized by wind-generated surface waves and bubbles,” *IEEE J. Ocean. Eng.*, vol. 38, no. 4, pp. 642–654, Oct 2013.
- [47] P. A. Walree, “Propagation and scattering effects in underwater acoustic communication channels,” *IEEE J. Ocean. Eng.*, vol. 38, no. 4, pp. 614–631, Oct 2013.
- [48] L. Foldy, “The multiple scattering of waves,” *Phys. Rev.*, no. 67, pp. 107–119, 1945.

BIBLIOGRAPHY

- [49] E. L. Carstensen and L. L. Foldy, "Propagation of sound through a liquid containing bubbles,," *J. Acoust. Soc. Amer.*, vol. 19, 1947.
- [50] K. Commander and A. Prosperetti, "Linear pressure waves in bubbly liquids: Comparison between theory and experiments,," *J. Acoust. Soc. Amer.*, vol. 85, no. 2, p. 732, 1989.
- [51] J. C. Devin, "Survey of thermal radiation and viscous damping of pulsating air bubbles in water,," *J. Acoust. Soc. Amer.*, vol. 31, 1959.
- [52] H. Medwin and C. S. Clay, *Fundamentals of Acoustical Oceanography*, Academic Press, 1998.
- [53] Z. Ye and L. Ding, "Acoustic dispersion and attenuation relations in bubbly mixture,," *J. Acoust. Soc. Amer.*, vol. 98, 1995.
- [54] C. Feuillade, "The attenuation and dispersion of sound in water containing multiply interacting air bubbles,," *J. Acoust. Soc. Amer.*, vol. 99, no. 6, 1996.
- [55] F. S. Henyey, "Corrections to foldy's effective medium theory for propagation in bubble clouds and other collections of very small scatters,," *J. Acoust. Soc. Amer.*, vol. 105, 1999.
- [56] S. G. Kargl, "Effective medium approach to linear acoustics in bubbly liquids,," *J. Acoust. Soc. Amer.*, vol. 111, 2002.
- [57] H. Medwin and C. S. Clay, *Acoustical Oceanography*, John Wiley and Sons, 1977.
- [58] H. Medwin, "In situ acoustic measurements of bubble populations in coastal ocean waters,," *J. Geophys. Res.*, vol. 75, no. 1, p. 599–611, 1970.
- [59] H. Czerski, "An inversion of acoustical attenuation measurements to deduce bubble populations,," *J. Atmospheric and Oceanic Tech.*, 2012.
- [60] P. S. Epstein and M. S. Plesset, "On the stability of gas bubbles in liquid-gas solutions,," *J. Chem. Physics*, vol. 18, p. 1505–1509, 1950.
- [61] K. George and P. H. Dahl, "Scattering measurements from a dissolving bubble,," *J. Acoust. Soc. Amer.*, vol. 131, pp. 4243–4251, 2012.
- [62] S. A. Thorpe, "Bubble clouds and the dynamics of the upper ocean,," *Journal of The Royal Meteorological Society*, vol. 118, no. 503, 1992.
- [63] G. P. Gerbi, "Observations of turbulence in the ocean surface boundary layer: Energetics and transport,," *Journal of Physical Oceanography*, vol. 39, 2009.
- [64] P. A. Walree, T. Jenserud, and S. Smedsrud, "A discrete-time channel simulator driven by measured scattering functions,," *IEEE Journal on Selected Area in Communications*, vol. 29, no. 26, 2008.
- [65] P. A. Walree, "Channel sounding for acoustic communications: techniques and shallow-water examples,," Norwegian Defence Research Establishment (FFI), Tech. Rep., 2011.
- [66] R. W. Lee and J. C. Harp, "Weak scattering in random media, with applications to remote probing,," *Proceedings of the IEEE*, vol. 57, no. 4, 1969.

- [67] A. Leon-Garcia, *Probability and Random Processes for Electrical Engineering, Second Edition (International Edition)*. Addison-Wesley, 1994.
- [68] T. H. Eggen, “Underwater acoustic communication over doppler spread channels,” Ph.D. dissertation, MIT, 1997.
- [69] D. M. Glover, W. J. Jenkins, and S. C. Doney, *Modeling Methods for Marine Science*. Cambridge University Press, 2011.
- [70] J. R. Potter, M. B. Porter, and J. C. Preisig, “Ucomms: A conference and workshop on underwater communications, channel modeling, and validation,” *IEEE J. Ocean. Eng.*, vol. 38, no. 4, pp. 603–613, Oct 2013.
- [71] W. Braun and U. Dersch, “A physical mobile radio channel model,” *IEEE Trans. Veh. Technol.*, vol. 40, no. 2, pp. 472–482, 1991.
- [72] A. Goldsmith, *Wireless Communication*. Cambridge University Press, 2014.
- [73] M. Chitre, “Underwater acoustic communications in warm shallow water channels,” Ph.D. dissertation, National University of Singapore, 2006.
- [74] B. Borowski, “Characterization of a very shallow water acoustic communication channel,” in *Oceans’09 MTS/IEEE*, 2009.
- [75] B. Tan, S. Quek, and N. Zou, “Characterization of multipath acoustic channels in very shallow waters for communications,” in *Oceans’06 MTS/IEEE Asia Pacific*, 2006.
- [76] W. Li and J. Preisig, “Estimation of rapidly time-varying sparse channels,” *IEEE J. Ocean. Eng.*, vol. 32, pp. 927–939, 2007.
- [77] M. Chitre, J. R. Potter, and S. H. Ong, “Optimal and near-optimal signal detection in snapping shrimp dominated ambient noise,” *IEEE J. Ocean. Eng.*, vol. 31, no. 2, 2006.
- [78] J. H. McCulloch, “Simple consistent estimators of stable distribution parameters,” *Commun. Statistical Simulation*, vol. 66, no. 336, 1986.
- [79] E. F. Fama and R. Roll, “Parameter estimates for symmetric stable distributions,” *J. Amer. Statistical Assoc.*, vol. 66, no. 334, 1971.
- [80] B. Sklar, *Digital Communications: Fundamentals and Applications*. Prentice-Hall International Inc., 2006.
- [81] A. J. Viterbi, “Phase-locked loop dynamics in the presence of noise by fokker-planck techniques,” *Proceedings of the IEEE*, vol. 51, pp. 1737–1753, 1963.
- [82] F. Fan and M. Loh, “Effect of noisy phase reference on coherent detection of band-limited offset-qpsk signals,” *IEEE Trans. on Comm.*, vol. 38, pp. 156–159, 1990.
- [83] O. Wurl, E. Wurl, L. Miller, K. Johnson, and S. Vagle, “Formation and global distribution of sea-surface microlayers,” *Biogeosciences*, vol. 8, no. 12, pp. 121–135, 2011.
- [84] M. M. Lozano, E. Talu, and M. L. Longo, “Dissolution of microbubbles generated in seawater obtained offshore: Behaviour and surface tension measurement,” *J. Geophy. Res.*, vol. 112, 2007.

BIBLIOGRAPHY

- [85] T. C. Weber, A. P. Lyons, and D. L. Bradley, "An estimate of the gas transfer rate from oceanic bubbles derived from multibeam sonar observations of a ship wake," *J. Geophys. Res.*, vol. 110, 2005.
- [86] V. Svein, D. M. Farmer, and G. B. Deane, "Bubble transport in rip currents," *J. Geophys. Res.*, vol. 106, 2001.
- [87] B. D. Johnson and P. J. Wangersky, "Microbubbles' stabilization by monolayers of adsorbed particles," *J. Geophys. Res.*, vol. 92, no. C13, 1987.
- [88] J. W. Cartmill and Y. S. Ming, "Bubble size distribution under saltwater and freshwater breaking waves," *Dynamics of Atmospheres and Oceans*, vol. 20, 1993.

List of Publications

Journals

- (J1) G. Chua, M. Chitre, and G. Deane, “Impact of Persistent Bubbles on Underwater Acoustic Communication,” *IEEE Journal of Oceanic Engineering*, (Submitted).
- (J2) G. Chua, M. Chitre, and G. Deane, “Characterization of an underwater acoustic channel with advected micro-bubbles,” *IEEE Journal of Oceanic Engineering*, (In-progress).

Conferences

- (C1) M. Chitre and G. Chua, “ Modeling realistic underwater acoustic networks using experimental data, ” *Asilomar Conference on Signals, Systems and Computers*, Pacific Grove, CA, USA, November 2014.
- (C2) G. Chua, M. Chitre, and G. Deane, “Impact of Persistent Bubbles on Underwater Acoustic Communication,” *Underwater Communications Networking*, Lerici, Italy August 2018.
- (C3) G. Chua, M. Chitre, and G. Deane, “Stabilization of micro-bubbles,” (In-progress).